(2)

ARMY RESEARCH LABORATORY

Development and Characterization of Adiabatic Shear Prone Tungsten Heavy Alloys

Animesh Bose, James Lankford, Jr., and
Herve' Couque

ARL-CR-60 July 1993

prepared by

Southwest Research Institute
6220 Culebra Road
San Antonio, TX 78228-0510

under contract

DAAL04-91-C-0065

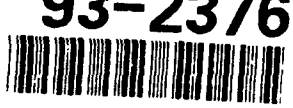

(6)

The findings in this report are not to be construed as an official Department of the Army position unless so designated by other authorized documents.

Citation of manufacturer's or trade names does not constitute an official endorsement or approval of the use thereof.

Destroy this report when it is no longer needed. Do not return it to the originator.

REPORT DOCUMENTATION PAGE

Form Approved
OMB No. 0704-0188

1. AGENCY USE ONLY *(Leave blank)*	2. REPORT DATE	3. REPORT TYPE AND DATES COVERED
	July 1993	Final Report - 10/1/91 - 1/31/93

4. TITLE AND SUBTITLE
Development and Characterization of Adiabatic Shear Prone Tungsten Heavy Alloys

5. FUNDING NUMBERS
Contract Number
DAAL04-91-C-0065

6. AUTHOR(S)
Animesh Bose, James Lankford, Jr., and Hervé Couque

7. PERFORMING ORGANIZATION NAME(S) AND ADDRESS(ES)
Southwest Research Institute
6220 Culebra Road, P.O. Drawer 28510
San Antonio, TX 78228-0510

8. PERFORMING ORGANIZATION REPORT NUMBER
SwRI 06-4601

9. SPONSORING/MONITORING AGENCY NAME(S) AND ADDRESS(ES)
U.S. Army Research Laboratory
Watertown, MA 02172-0001
ATTN: AMSRL-OP-PR-WT

10. SPONSORING/MONITORING AGENCY REPORT NUMBER
ARL-CR-60

11. SUPPLEMENTARY NOTES
Robert Dowding, COR

12a. DISTRIBUTION/AVAILABILITY STATEMENT
Approved for public release; distribution unlimited.

12b. DISTRIBUTION CODE

13. ABSTRACT *(Maximum 200 words)*

SEE PAGE 1 .

14. SUBJECT TERMS
Tungsten heavy alloy, Alloy development, Mechanical properties, Adiabatic shear

15. NUMBER OF PAGES
80

16. PRICE CODE

17. SECURITY CLASSIFICATION OF REPORT	18. SECURITY CLASSIFICATION OF THIS PAGE	19. SECURITY CLASSIFICATION OF ABSTRACT	20. LIMITATION OF ABSTRACT
Unclassified	Unclassified	Unclassified	UL

NSN 7540-01-280-5500

Standard Form 298 (Rev. 2-89)
Prescribed by ANSI Std. Z39-18
298-102

"DEVELOPMENT AND CHARACTERIZATION OF ADIABATIC SHEAR PRONE TUNGSTEN HEAVY ALLOYS"

ABSTRACT

Depleted uranium (DU) is currently the top-performing kinetic energy penetrator, followed closely (but not matched) by several tungsten heavy alloy variants. Because of the adverse environmental impact associated with DU, it is extremely desirable to determine a means of upgrading the ballistic performance of heavy alloys to a level at least comparable to that of DU.

It is thought that the reason for the improved ballistic performance of DU-0.75 Ti alloy is embedded in its ability to self sharpen during armor penetration, and it is further postulated that this self-sharpening ability is due to the susceptibility of DU to adiabatic shear during penetration events. The contrasting inability of current tungsten heavy alloys to localize shear during penetration causes mushrooming at the head of the projectile, thus decreasing the depth of penetration. Consequently, there is a great urgency to develop new tungsten alloys that will exhibit localized, unstable shear failure, and associated self sharpening during armor penetration.

It should be pointed out that using ballistic tests as the means of screening a large number of new materials is extremely expensive and impractical. Thus, there is also a need for developing a rapid and relatively inexpensive high strain rate screening method for testing various heavy alloys and determining the relative ease of shear localization in these alloys.

The primary aim of this project was to process and test a suite of tungsten heavy alloys based on the theoretical principles of adiabatic shear phenomena. To achieve those goals, it was necessary to have a screening method by which the suite of alloys could be tested and compared with the current 90W-8Ni-2Fe baseline tungsten heavy alloy. This report provides the results of the investigations that have been carried out during the first year of a three-year contract. The findings show that the heavy alloy microstructure and thermomechanical processing have a significant effect on the shear localization tendency of tungsten heavy alloys.

INTRODUCTION

A. Role of Shear Localization in Penetration

High density is one of the key attributes for successful kinetic energy penetrator materials, and the only two high density materials that are economically viable are DU and tungsten heavy alloys. Although both materials possess the combination of high density, strength, and ductility required for ballistic penetration, their metallurgical characteristics and processing methods are completely different.

At present, DU is known to be a more effective penetrator material than an equivalent density tungsten heavy alloy, a phenomenon whose basis seems to reside in the ability of DU to self-sharpen during penetration. However, mounting political pressure and increasing environmental concern have created conditions whereby DU penetrators, despite their improved penetration characteristics, are being discarded in favor of tungsten heavy alloys. This situation has led to tremendous interest in processing and testing new tungsten heavy alloys that would provide penetration properties similar to, or better than, DU.

Recent experiments by Magness and Farrand [1] have provided solid evidence that the superior performance of DU is rooted in the ability of this material to fail through the formation of adiabatic shear. This prevents the formation of a stable "mushroom head" by constant "self-sharpening" of the DU penetrator. Mushrooming has a detrimental effect on the penetration efficiency, as the resisting pressure on the projectile is over a proportionally larger area, causing greater deceleration force. Current state-of-the-art tungsten heavy alloys, unfortunately, do not appear to self-sharpen, and thereby lose penetration efficiency. Therefore, improved penetration performance may be induced in tungsten heavy alloys in which the localized adiabatic shear failure can be enhanced.

B. Characteristics of Tungsten Heavy Alloys

Tungsten heavy alloys are a class of two-phase composites characterized by high density and a microstructure consisting of tungsten grains embedded in an alloy matrix. They are processed by classic liquid-phase sintering of elemental tungsten mixed with binders like Ni-Fe, Ni-Cu, Fe- Ni-Co, or Co-Ni. The tungsten content normally varies from 90 to 98 weight percent. The final sintered microstructure consists of nearly pure bcc tungsten grains dispersed in a ductile fcc matrix. Alloys with W-Ni-Fe are among the most popular heavy alloys. These alloys have an approximate matrix composition of 53Ni-23Fe-24W [2]. The typical mean tungsten grain size varies from 20 to 40 μm depending on the volume fraction of tungsten, initial particle size, sintering temperature, and sintering time.

The unique property combination of high strength (800 to 1000 MPa), high ductility (from 10% for high tungsten alloys to 30% in 90 wt.% tungsten alloys), very high density (usually from 16 to 18 g/cc), good electrical and thermal conductivity, and excellent machinability, are making these alloys useful for numerous applications [3-5]. The army traditionally is one of the major users of tungsten heavy alloys, and uses include armor-piercing projectiles, counterbalances in helicopters and military aircraft, outer casings of hand grenades, etc. The recent efforts to use heavy alloys as a replacement for depleted uranium (DU) kinetic energy penetrators have resulted in a renewed surge of research efforts on tungsten heavy alloys.

C. Means of Promoting Shear Localization in Heavy Alloys

It is our opinion that tungsten heavy alloys do have the potential (not yet optimized) for unstable, possibly adiabatic, shear. In support of this hypothesis is the observed deformation caused by uniaxially compressing a standard 90W-7Ni-3Fe alloy to 55% strain at a strain rate of 5500 s^{-1}. As a result, the specimen is riddled with 45° shear cracks nucleated within intense deformation bands; study of a polished section through such a crack reveals the deformation attending its initiation/propagation. However, it is obvious that the presence in the laboratory of such shear localized bands in the 90W-7Ni-3Fe alloy does not carry over to the penetration process. Thus, it is clearly necessary to alter the fundamental deformation behavior of the conventional tungsten heavy alloys if adiabatic shear or shear localization is to play a useful role during penetration. Some of the possible approaches are outlined below.

1. If a new matrix that is more prone to adiabatic shear localization can be incorporated, it is possible that the overall composite will exhibit a greater tendency toward shear localization.

2. Based on a number of observations, it seems reasonable to believe that it may be possible, through appropriate thermomechanical processing, to optimize the propensity of tungsten heavy alloys to fail by shear localization.

3. Though microstructure does not play a significant role in the process of adiabatic shear of monolithic materials, it is expected that it would play a major role in the two phase composite materials such as tungsten heavy alloys. Inhomogeneous microstructures (small amounts of porosity; local matrix "pools") could provide triggers for the initiation of shear localization, while the ease of propagation of these small bands will depend on how easily they can bypass the tungsten grains.

D. Means of Screening of Materials

The major thrust of most heavy alloy research to date has been geared toward improving quasi-static properties by varying the processing parameters. In particular, the classic W-Ni-Fe alloys with 90 to 93 weight percent tungsten have quasi-static properties that are almost identical to DU-0.75Ti alloys, aside from the yield strength, which is approximately 25 to 30% higher for the tungsten alloys. However, heavy alloys are much more strain-rate sensitive compared to DU, and the toughness of heavy alloys under impact loading conditions is much lower than DU. These and a number of other ballistic properties are not predicted from the quasi-static behavior. Thus, it is important to determine the dynamic properties of new tungsten alloys developed for kinetic energy penetrator applications.

Recent work by Lankford, et al., [6], demonstrates that tungsten-based heavy alloys do have the potential for localized shear. In that study, the investigation was carried out on a classic 90W-7Ni-3Fe alloy specimen that was tested in compression using the split Hopkinson pressure bar technique at a strain rate of 5500 s^{-1}. The sectioned specimen was studied to reveal the shear localization characteristics of the material. In this case, numerous 45° cracks were observed within intense shear bands. If such unstable shear zones can be created at lower critical strains for initiation (around 30% compression say), it should be possible to produce tungsten heavy alloys that would fail by localized shear (i.e., self-sharpen) during penetration. To achieve this, it is imperative to incorporate some means by which the shear bands and the associated cracks can either by-pass or fracture most of the tungsten particles they encounter.

Given a suite of varying W-alloy microstructures, it appears to us that the best screening method for shear propensity is to use the SHPB technique, and compression test the desired suite of alloys at high strain rates. This must be followed up by microscopic characterization to determine the relative abilities of the materials to localize shear since the presence or absence of unstable shear generally does not manifest itself in the stress-strain curve.. In totally new alloys, of course, it is useful to first carry out routine compression tests at slow strain rates to determine if any of the materials are intrinsically brittle, in which cases it would not be justifiable to carry out the high strain rate testing on those material systems.

E. Microstructural Analysis

The W-Ni-Fe heavy alloys exhibit a classical liquid phase sintered microstructure. Often the usefulness of these materials is very much dependent on their microstructures, as the physical and mechanical properties of these alloys are dependent on their microstructural

features. In case of heavy alloys, the microstructure typically consists of a large volume fraction of pure tungsten embedded in a matrix, which forms the liquid at the sintering temperature. Due to differences in processing and material variables, uncertainties remain with respect to the microstructure of the heavy alloys. Thus, quantitative metallographic analysis of the heavy alloys used for the present investigation should constitute an important part.

The various microstructural characteristics that influence the properties of tungsten heavy alloys are volume fraction of tungsten, grain size of the tungsten phase, the contiguity, connectivity, and the dihedral angle. Generally volume fraction of tungsten increases with increasing tungsten content in the system. The grain size of the tungsten particles for the same composition can be increased by increasing the sintering temperature or the sintering time. To obtain a good measure of the grain size, it is necessary to measure the size of a large number of grains. The dihedral angle provides a measure of wetting of the tungsten grains by the liquid matrix. Small changes in the composition and processing conditions can affect the dihedral angle. Dihedral angle measurements are usually made by measuring the angle between two tangent lines drawn at the solid-solid-matrix intersection. An average of a large number of such measurements provides the best estimate of the true dihedral angle.

A classic problem in analyzing the microstructure of tungsten heavy alloys is the conversion that is necessary from a two-dimensional metallographic cross-section to a representation of the actual three-dimensional structure. The connected solid tungsten grains are expected to influence the final properties of these alloys. There are two ways of providing a qualitative measure of the connectivity of these materials. They are known as contiguity and connectivity. Contiguity is a measure of the average fraction of a tungsten grain that is actually in contact with other solid tungsten grains, while the connectivity is a measure of the number of contacts that each particular tungsten grain makes with its neighboring solid grains. From the two dimensional microstructure, the contiguity is determined by counting the number of tungsten-tungsten interfaces, N(ww), and the number of single grid line. A large number of parallel grid lines can be used to cover the total microstructure. The contiguity, C, is then calculated using the formula:

$$C = 2N(ww)/[2N(ww) + N(wm)]$$

The connectivity is measured by actually counting the number of contacts that each grain makes with its neighbors. The connectivity is determined by dividing the total number of contacts by the total number of grains within the field of the microstructure.

Apart from these measurements, it is also necessary to assess qualitatively the microstructure of the alloys in terms of porosity, inhomogeneous segregation of the matrix material, or presence of inclusions. All these microstructural features play an important role in determining the final properties of tungsten heavy alloys.

EXPERIMENTS AND RESULTS

The alloys studied during the course of the first year (Table 1) can be separated into two broad categories, the first involving microstructural variation (Alloys 1 through 7), the second a range of thermomechanical treatments (Alloys 8 through 14, and Alloy 3); Alloy 3 is common to both studies. All alloys have been assigned a particular number, and that number will be referred to throughout this report. The subsequent sections describe the various tests that were carried out on some or all of the above samples.

A. Microstructural Characterization

Round cylindrical samples of these alloys were obtained from commercial vendors, although in some cases the materials were specially fabricated. Small pieces cut from the end of the rods were mounted, polished, and observed in the SEM. The microstructure of Alloys 1 through 14 are shown in Figures 1a through 1n, respectively.

Since the microstructural characteristics were considered to have an effect on the shear localization behavior of tungsten heavy alloys, it was decided that several samples would be investigated in detail. The chosen samples were characterized in terms of their mean grain intercept length, tungsten volume fraction, contiguity, connectivity, and dihedral angle. To measure the mean grain intercept length and the volume fraction of tungsten, four different areas of each sample were selected at random for each set of specimens. The SEM photomicrographs were taken at magnifications that would provide 30 to 50 tungsten grains within the frame, and were stored in the image analyzer. The contacting tungsten grains were manually dissected before carrying out the grain size analysis. This was done to separate the contiguous grain boundaries and ensure their not erroneously being included by the machine within a single grain. The volume fraction of solid and the mean intercept lengths were measured by the automated image analyzer. The mean value of the four measurements has been reported for each specimen.

For the measurement of the contiguity, connectivity, and the dihedral angle of the selected specimens, all of the SEM photomicrographs were enlarged to 8 x 10 inches. On these enlarged photomicrographs, the tungsten-tungsten grain contacts were carefully marked with a colored pen. The 24 enlarged photomicrographs were than evaluated.

The measurement of contiguity and connectivity involves a procedure of counting a large number of points, essentially using a transparent grid. The counting includes the number of tungsten-matrix contacts and the number of tungsten-tungsten contacts for determining the contiguity, and the number of tungsten-tungsten contacts per tungsten grain in the two-dimensional photomicrographs for determining the connectivity. The mean value of the four SEM photomicrographs was defined as the value of the contiguity and connectivity of each sample. The dihedral angle was determined by drawing two tangential lines at the tungsten-tungsten-matrix intersections. A large number of angles (between 150 to 200) were measured, and the mean values of the resultant distribution were taken as the best estimate of the true dihedral angle for each type of specimen.

As some of the microstructural characterization was extremely tedious and expensive, the alloys to be characterized were carefully chosen to cover the baseline composition (Alloy 1), the effect of grain size (Alloys 3, 4, and 5), and the effect of tungsten volume fraction (Alloys 3, 6, and 7). The results of the microstructural analysis are given in Table 2.

B. Screening Tests

Compression test samples were machined from the as-sintered or thermomechanically treated rods into cylindrical specimens 6.35 mm in diameter and 12.7 mm in length. Dynamic compression tests were performed at a strain rate in the range of 4000 to 5000 s^{-1}, using the split Hopkinson pressure bar (SHPB) technique [7] (Figure 2). A compression specimen placed between two long, high-strength steel bars is loaded by propagating a compressive pulse generated in one of the elastic bars by impacting it with a gas-fired projectile striker. The SHPB pulse length, proportional to the length of the striker, was usually sufficient to produce plastic strains in the specimen on the order of 0.35 to 0.50. The true stress-true strain curves that were generated from these tests are shown in Figures 3a through 3n.

The outer surfaces of the tested samples were first examined for any signs of shear localization. The specimens were then sectioned, mounted, polished, and observed under the SEM. When present, shear bands generally were observed along the lines that form the diagonals of the cross-sectioned specimens. Representative montages were made of the shear bands, and in some cases, interesting portions of bands were studied at higher magnification.

It should be noted that the samples in which the shear bands were observed could be divided into three categories. The first type of samples were one which showed clear evidence of one or more shear crack on the outer surface of the compression tested sample, and when the sample was sectioned, they also exhibited clear evidence of shear localization. The second type of samples also exhibited shear cracks on the outside surface of the

compression tested specimen but the sectioned material did not show any clear evidence of shear localization. The third category of specimens did not show any external shear cracks or any shear localization in the sectioned part. Examples of the shear cracks on the outer surface are shown in Figures 4a through 4e. The montages of the shear bands for all the alloys are shown in Figures 5 though 21. As mentioned earlier, there were several samples that did not exhibit shear localization on the sectioned area, but did show clear shear induced cracks on the outer surface. For these samples, the montages represents the area near the external shear crack. For these samples, the SEM photomicrographs of the polished flats are also shown in the same figure that shows the SEM photomicrographs of the montages.

C. Mode II Tests

We are still in the process of developing the Mode II fracture test, with the proposed setup as shown in Figure 22. The design consists of a compact specimen with two parallel machined notches; loading is conducted by impacting the specimen between the two notches with a miniaturized striker, 6.35 mm in diameter. Striker velocity is measured 10 mm in front of the striker-specimen interface, and the specimen loading history is monitored by means of a strain gage located between the notches and 5 mm from the striker-specimen interface.

Based on a series of experiments, the loading conditions required to reach a given striker velocity and to ensure a planar impact at the striker specimen interface have been identified. Planar impact was obtained by guiding the miniaturized striker to the striker specimen interface within a cylindrical Teflon Sabot. However, localized shear deformation was not observed at either of the two (symmetric) crack tip locations. This appears to be caused by the absence of hydrostatic pressure in the K_{II} specimen, as compared to the uniaxial compression specimen. These results agree with recently published data generated using torsional specimens in which the hydrostatic pressure is known to be less than in the compression specimen [8]. In these specimens, only coarse shear bands were observed prior to fracture. The shear band was found to involve deformed tungsten particles of maximum aspect ratio 5, which is 5 to 10 times less than the deformed tungsten particles within local unstable shear bands in the compression specimen. Consequently, it is planned to conduct the next series of experiment involving K_{II} specimens with superimposed static confining pressure.

Thus, a series of experiments will be carried out in the second year whereby:

1) Static confined pressure will be applied normal to the anticipated crack direction.

2) A damping mechanism will be implemented to reduce the intensity of reflected tensile stress waves.

3) The size of the notch radius, the striker length, and the striker velocity will be varied to enable specification of the loading conditions promoting shear band formation in the Mode II fracture specimen.

D. Quantification of Shear Bands

Considerable progress has been achieved in establishing a means of quantifying the shear localization tendency of the heavy alloys. This is a complex process, one that requires careful visual inspection of what can be considered the core of the band. First, an imaginary straight line is drawn through the core of the band, and that straight line is considered to be the center of the shear localized area. In several cases, it was found that one straight line could not account for the core of the band over an extended length of the shear localized zone. In those cases, bands apparently have initiated at various locations in the structure, but have not been joined together to form a straight line. An example of such a case is shown in Figure 23, an as-sintered (i.e., unswaged) 91W-6Ni-3Co alloy tested in compression at a high strain of 5070 s^{-1}. When the same alloy is 25% swaged and aged, the shear band formed is narrow and almost straight. In this particular case it was not necessary to draw a line through the core of the band as the material exhibited shear-induced cracking. The crack is essentially considered to be the core of the band, as can be seen in Figure 24.

To find suitable criteria for quantifying the shear localization tendency, the aspect ratio of the individual grains within the shear band is taken into consideration. The aspect ratio is simply measured by dividing the length measured on an elongated tungsten grain (denoted as "a" in Figures 23 and 24) by the width of the same tungsten grain (denoted as "b" in Figures 23 and 24). The measurements are relatively simple when they are made on grains that are far removed from the core of the shear band and in cases where the shear is not very well localized. However, when the shear is well localized, as in the case of the example shown in Figure 24, parts of individual grains that are very close to the shear band are extensively elongated. The question is how to measure the aspect ratio of these grains that are almost adjacent to the core of the shear band. In such cases, the individual grains looked like teardrops, where one section of the drop has been elongated extensively. In these cases, an imaginary line is drawn to cut away the thick section of the teardrop-shaped grain. The aspect ratio is measured only on the heavily elongated section. This situation is illustrated in Figure 25.

To carry out the actual measurements, several lines are drawn perpendicular to the line denoting the core of the band, extending across both sides of the shear band core. Only the tungsten grains that are intersected by these perpendicular lines are considered for measurement. The distance (y) of each grain (being measured) from the core of the shear band is measured, as shown in Figures 23 and 24. The variation of the height with the aspect size ratio for all the measured grains is plotted for each alloy. Materials that exhibit localized shear show a very high aspect ratio of grains only when very close to the vertical axis of the figure. In fact, the aspect ratios are so large that they become difficult to measure. In comparison, materials that do not exhibit intense shear localization do not have high aspect ratios concentrated close to the vertical axis of the figure.

This situation is well illustrated in Figure 26, which shows the variation of "y" (the distance from the core of the shear band) with the tungsten grain aspect ratio, for 91W-6Ni-3Co alloys in the as-sintered (Alloy 8; marked in the figure as 0), 7% swaged and aged (Alloy 9; marked in the figure as 7), and 25% swaged and aged (Alloy 10, marked in the figure as 25). It can be observed that the as-sintered alloy exhibits a maximum aspect ratio of 23; the 7% swaged and aged alloy has a maximum aspect ratio of 25; the 25% swaged and aged alloy has an aspect ratio that far exceeds 30. It can also be observed from Figure 26 that the very high aspect size ratio of the 25% swaged and aged alloy is actually concentrated over a very narrow distance from the core of the shear band (approximately 5 μm).

Further work on the quantification of other samples is expected to continue in the second year.

E. Processing of New Alloys

The efforts on processing of new tungsten alloys were taken up toward the later stages of the first year. Because the microstructure did play an important role in affecting the shear localization tendency of the tungsten heavy alloys, the first new heavy alloy that was processed was a 85W-5Re-7Ni-3Fe alloy. This alloy is expected to be stronger and have a smaller grain size (which is expected to enhanced shear localization) compared to the conventional 90W-7Ni-3Fe alloy. Two round, cylindrical samples with a composition of 85W-5Re-7Ni-3Fe (wt.%) were cold isostatically pressed at 12 kpsi. This pressure was too low for good compaction of the powders, and the resultant compact was broken into a number of pieces. Unfortunately, 12 kpsi was the maximum pressure that could be achieved in the cold isostatic press at Rensselaer Polytechnic Institute during that time. However, two reasonably large fragments could be sintered, and accordingly were sintered at 1500°C, using the three-stage sintering atmosphere developed by Bose and German [9]. The following sintering schedule was used to sinter this alloy.

1. Room temperature to 800℃ at 10℃/min (dry hydrogen)

2. Hold at 800℃ for 1 hour (dry hydrogen)

3. From 800℃ to 1300℃ at 10℃/min (dry hydrogen and switch to wet hydrogen at the end)

4. From 1300 to 1500℃ at 5℃/min (wet hydrogen)

5. Hold at 1500℃ for 45 minutes (convert to dry argon during the last 5 minutes of the hold)

6. From 1500℃ to 1300℃ at 3℃/min (dry argon)

7. Furnace cool from 1300℃ to room temperature (dry argon)

The dew point of the dry hydrogen was -39℃, and the wet hydrogen was +13℃. The sintered material was subsequently heat treated by quenching in water from 990℃ after holding at that temperature for 1 hour in argon atmosphere. Characterization and testing of this alloy will be taken up during the second year of the project. Another new alloy that was processed at the MTL, Watertown, MA, was a conventional 90W-7Ni-3Fe alloy, which was doped with alumina powder. We have sectioned the alumina-doped heavy alloy samples, and documented several microstructural deficiencies. First, there is a definite microstructural gradient from the top to the bottom surface of the material. In addition, there is also a gradient in the distribution of alumina in the microstructure, which is apparently induced during liquid phase formation. Finally, the particle size of the alumina is also too large. Figures 27a through 27c show the sample microstructures at three different locations, the top, the transition zone where the rounded tungsten grains change to jagged tungsten grains (implying a low sintering temperature), and the bottom of the sample, respectively. Because of anticipated poor mechanical properties it was decided that these samples would not be tested. Possible changes that could alleviate some of these problems are: using finer alumina powder; processing a thicker specimen; and sintering at higher temperature.

Processing of new alloys is expected to continue during the second year, with at least three new alloys probably being added to the present list of materials.

DISCUSSIONS

For the sake of clarity and ease of understanding, the results and discussion section will be divided into two broad sections, one dealing with the effects of microstructure and the other with the effects of thermomechanical processing.

Effect of Microstructure

The following suite of alloys was selected to carry out investigations regarding microstructural influence in the shear stability of the alloys:

Alloy 1. 90W-8Ni-2Fe alloy, pore free and homogeneous microstructure, normal sintering time of approximately 45 minutes.

Alloy 2. 90W-7Ni-3Fe alloy porous and inhomogeneous microstructure.

Alloy 3. 90W-7Ni-3Fe alloy, pore free and homogeneous microstructure, normal sintering time of approximately 45 minutes.

Alloy 4. 90W-7Ni-3Fe alloy pore free and homogeneous microstructure, sintering time of 240 minutes.

Alloy 5. 90W-7Ni-3Fe alloy pore free and homogeneous microstructure, sintering time of 800 minutes.

Alloy 6. 95W-3.5Ni-1.5Fe pore free and homogeneous microstructure, normal sintering time of approximately 45 minutes.

Alloy 7. 86W-9.8Ni-4.2Fe pore free and homogeneous microstructure, normal sintering time of approximately 45 minutes.

The results of the detailed microstructural characterization of all the selected alloys, except Alloy 2, is shown in Table 2. For Alloy 2, only the mean grain intercept length (which is a measure of the grain size) and the volume fraction of the solid phase were measured. For all other alloys, the characterization included the mean intercept length (which is a measure of the grain size), the volume fraction of solid, contiguity, connectivity, and dihedral angle.

A. Conventional Tungsten Alloys

One of the first samples studied was a 90W-8Ni-2Fe alloy (Alloy 1), selected as the baseline composition. The microstructure was quite uniform, as can be seen in Figure 1a; there is practically no porosity and the tungsten grains are well dispersed within the matrix alloy. This is the current standard W-alloy for use in penetrators.

The montage of the shear band that is formed when the alloy is tested at a strain rate of 5231 s^{-1} can be seen in Figure 5. Broad, highly deformed shear bands were present in the 90W-8Ni-2Fe alloy, but there was no evidence of any unstable shear localization. The presence of elongated tungsten grains was observed over a large thickness and the band was quite diffuse. There was no evidence of any cracking or extensive localization of the deformation within a narrow band. Thus, the baseline alloy is not one that exhibits the shear localization.

The next alloy that was investigated was a 90W-7Ni-3Fe alloy (Alloy 2) that had an inhomogeneous microstructure. The microstructure, shown in Figure 1b, was characterized by dispersed porosity and areas that can be qualitatively referred to as "lakes" of matrix alloy. The alloy showed extensive shear localization and cracking when tested in compression at a strain rate of 5559 s^{-1}; in fact, this test resulted in the failure of the specimen. One-half of the failed specimen was sectioned, mounted, polished, and observed in the SEM. There was clear evidence of shear band localization, as seen in the montage shown in Figure 6. The inhomogeneous nature of the microstructure can also be clearly observed from Figure 6. Figure 6 also shows that the tungsten grains are extensively elongated and the band width lies within a very narrow range. Thus, this material of inhomogeneous microstructure is definitely capable of shear localization. The next logical transition was to evaluate the properties of a 90W-7Ni-3Fe alloy with a clean and uniform microstructure. The microstructure of such an alloy (Alloy 3) is shown in Figure 1c. This material, tested at a strain rate of 5668 s^{-1}, showed evidence of shear cracking even on the outer surface of the specimen (Figure 4a). The sectioned sample showed evidence of shear localization that was qualitatively much more localized than the (clean) 90W-8Ni-2Fe alloy, but was definitely more diffuse than the 90W-7Ni-3Fe alloy with the inhomogeneous microstructure. The montage of a portion of the shear band is shown in Figure 7, where there is evidence of a small crack lying within the band. However, since this sample showed a shear-induced crack on the outer surface of the compression tested material (Figure 4a), the material was remounted and polished with the cracked side facing the edge being polished. The montage of the shear band near the area close to the cracked edge (not near the sectioned center) is shown in

Figure 8. A macro-photograph of the polished section is also shown in the same picture. It is clear from this montage that near the cracked surface the material underwent extensive shear localization and shear-induced cracking.

A comparison of the three shear bands shown in Figures 5, 6, and 7 brings out the important effect of the microstructure. From the montage showing the shear band in the 90W-7Ni-3Fe alloy with the porous and inhomogeneous microstructure, it is clear that this particular alloy exhibited the thinnest shear band, with extensive unimpeded elongation of the tungsten grains. This may be at least partly due to the inhomogeneous nature of the microstructure, characterized by large pools of W-free matrix where shear bands might nucleate and grow unimpeded. In addition, it is also possible that the porosity present in the same microstructure could serve as the trigger mechanism that localizes the shear in the material. It would seem, therefore, that there might be some merit, in terms of shear localization, in having an inhomogeneous microstructure with small volume fraction of porosity dispersed in it. However, materials with such a nonuniform microstructure could well exhibit poor general mechanical properties. Over and above that, consistently processing such inhomogeneous materials would be extremely difficult.

An obvious and important question concerns the nature of the difference between a homogeneous pore-free 90W-7Ni-3Fe (Alloy 3) and a 90W-8Ni-2Fe (Alloy 1) alloys, the former exhibiting unstable shear, the latter not. In order to asses the extent of difference in matrix chemistry between the two alloys, an EDS analysis of the matrices was carried out, with the following results:

Alloy 1: 37W, 50Ni, and 13Fe (weight percent)
Alloy 3: 34W, 47Ni, and 19Fe (weight percent)

It might be argued that the slightly lower tungsten content in the 90W-7Ni-3Fe alloy matrix could make it more prone toward shear localization, as tungsten by itself is not amenable to adiabatic shearing. However, the tungsten is in this case alloyed with the other constituents and not segregated into pure W-enclaves, so that the small difference in the chemistry per se of the two alloys seemingly provides only a weak argument for the difference in the shear localization tendency between the two. Therefore, some influence of chemistry was sought by considering certain implications deriving from the results of the microstructural analysis. First, it was noted that the average intercept length for the 90W-7Ni-3Fe alloy with the pore free and homogeneous microstructure is around 17.8 μm, while for the 90W-8Ni-2Fe alloy, the average intercept length is 23.5 μm. Thus, the 90W-7Ni-3Fe alloy does have a slightly smaller grain size than the 90W-7Ni-3Fe alloy. Theoretically, a smaller grain size should promote the tendency for shear localization by

providing more direct routes for shear band propagation; this is supported by our prior work on a relatively fine-grained W-Ni-Mn based alloy [10]. Thus, the slightly smaller grain size of Alloy 3 (90W-7Ni-3Fe) could also influence the shear localization tendency of this material. Moreover, the 90W-7Ni-3Fe alloy has a contiguity of 0.293, which is larger than that (0.195) of the 90W-8Ni-2Fe alloy (Table 2). A larger contiguity means a larger amount of tungsten-tungsten contacts within the microstructure. The tungsten-tungsten contact, which is the weakest link in the microstructure, is probably the first segment that fails. For almost the same volume fraction of tungsten, it is likely that a larger number of W-W microcracks are created within the microstructure in the high contiguity alloy. These local flaws may then serve as local triggers for shear instability in the microstructure.

It is difficult to determine at this point which of the above mechanisms are responsible for the greater propensity of the 90W-7Ni-3Fe alloy to localize shear compared to the 90W-8Ni- 2Fe counterpart. It is probably due to a combination of matrix chemistry, grain size difference, and difference in the contiguity of the two alloys. The previous discussion would seem to suggest that a smaller grain size and a smaller volume fraction of tungsten promote the shear localization process. However, the grain size variation available with the normal sintering process is not wide enough to quantify the relative importance of this variable. Similarly, it is difficult to implement significant variation in the volume fraction of tungsten when the initial tungsten content is kept the same. Thus, further experiments were designed to study the aspect of grain size and the tungsten volume fraction.

B. Effect of Tungsten Grain Size

To obtain a true gauge of the effect of tungsten grain size on the propensity of the alloy to localize shear, it is first necessary to maintain uniform alloy chemistry. Thus, the same composition, 90W-7Ni-3Fe, was chosen for these experiments.

The grain size of tungsten heavy alloys can be changed principally by two methods:

1. Increasing the sintering temperature
2. Increasing the sintering time

Increasing the sintering temperature results in greater solubility of the tungsten in the matrix. This changes the matrix chemistry of the material, and therefore, makes it difficult to separate the effect of grain size and the matrix chemistry. Thus, it was decided that grain size variations would be induced by increasing the sintering time.

Two sets of samples were sintered for 240 minutes (Alloy 4) and 800 minutes (Alloy 5). These alloys could be directly compared to Alloy 3, sintered for the normal length of time (approximately 45 minutes).

The first task was to ensure the relative uniformity of the matrix chemistry of the three alloys. EDS analysis on the matrix of the three alloys revealed the following compositions (weight percent):

Alloy 3 (45 minutes): 34W, 47Ni, and 19Fe
Alloy 4 (240 minutes): 36W, 46Ni, and 18Fe
Alloy 5 (800 minutes): 34W, 47Ni, and 19Fe

Thus, the matrix chemistry of the three alloys was not significantly different.

Microstructural characteristics, especially the mean grain intercept length, which provides a measure of the grain size, were then scrutinized. As expected, it was found that the mean grain intercept length of the three alloys had increased with sintering time. The alloys sintered for 45, 240, and 800 minutes had mean grain intercept lengths of 17.8, 38.7, and 59.8 μm, respectively; their microstructures are shown in Figures 1c, 1d, and 1f, respectively. The volume fraction of tungsten grains varied between 0.76 to 0.81.

As noted earlier, Alloy 3 (45 minute sinter) showed both surface and internal shear localization, and associated surface shear band fracture (Figure 4a). However, while the alloy sintered for 240 minutes (Alloy 4) also showed a shear-induced crack on its outer surface (Figure 4d; Alloy 4), when the specimen was sectioned at the center, there was little evidence of internal shear localization. The montage of the surface shear band, shown in Figure 9, showed extensive cracking and shear localization. Thus, this alloy does have some of the ability to experience shear localization and cracking similar to the 90W-7Ni-3Fe alloy sintered for 45 minutes. However, the internal shear localization observed for the 45 minutes sinter (Figure 7) was not duplicated in the alloy sintered for 240 minutes.

The results for the 800 minute sinter continued this trend. The mean intercept length of the tungsten grains for this long-time sintered material was around 59.8 μm, (approximately three times that achieved in the 45 minutes sinter, and 50% larger than that obtained within 240 minutes sinter). This alloy showed no shear-induced cracks, although when the specimen was sectioned at the center, some evidence of shear localization was seen; this was intense only near the impacted edge of the sample. From the montage of the shear band in this alloy, which is shown in Figure 10, it appears that the band which did form close to the edge was unable to propagate to any large distance. Thus, in this case, it would appear that though

shear was able to localize, the propagating shear band was impeded by the large tungsten grains and could not propagate macroscopically. This finding, coupled with the relative ease of shear band propagation in the fine grained W-Ni-Mn alloys [10], strongly suggests that shear localization would be favored by fine grain size.

Since tungsten by itself will not shear adiabatically, while the matrix itself can easily deform and localize shear, one assumes that adiabatic shearing is almost exclusively concentrated within the matrix material. However, in order to propagate the band, the tungsten grains must be deformed to a critical state such that an adequate mean free path is created between a number of adjacent tungsten particles. Thus, it is reasonable that it should be relatively difficult for the general, fairly diffuse shear field within a specimen to deform relatively large tungsten grain sufficient to establish the mean free path required for locally intense shear enclaves to propose.

C. Effect of Tungsten Volume Fraction

Based on the preceding experience, it seems clear that improvements in shear localization tendency can be brought about by reducing the impedance posed by tungsten grains. One of the simplest ways of testing this theory is to change the volume fraction of tungsten while maintaining a similar chemistry of the matrix alloy. Thus, a suite of alloys characterized by 86, 90, and 95 weight percent tungsten were processed (the microstructures of the 95W and 86W alloys are shown in Figures 1f and 1g, respectively). The matrix chemistries of the alloys are given below.

Alloy 3: 34W, 47Ni, and 19Fe
Alloy 6: 32W, 49Ni, and 19Fe
Alloy 7: 34W, 47Ni, and 19Fe

It is clear that the matrix chemistries of the alloys are almost similar. This is to be expected because nickel-to-iron ratios of the three alloys were kept the same. Tungsten volume fractions of the alloys are 0.76, 0.80, and 0.69, respectively (see Table 2), proportional to the weight percent of tungsten in each heavy alloy.

The montage of the shear band of Alloy 6 (95W), shown in Figure 11, indicates very little shear localization, i.e., the shear band was extremely diffuse and very broad. There was no evidence of any shear-induced cracking on the outside surface of the compression tested specimen. Thus, this alloy, which has a high volume fraction of tungsten, clearly is not prone to shear localization. Interestingly, this alloy also has a very high contiguity, which means that the tungsten-tungsten contact in this alloy is more frequent. According to earlier

discussion, it was postulated that increased contiguity could enhance shear cracking. However, that consideration would apply to alloys with comparable volume fractions of solid. In this case, the very high tungsten volume fraction simply prevents the propagation of the shear bands which must precede crack nucleation.

When Alloy 7 (86W) was tested in compression, shear-induced cracking was clearly visible on the outside surface of the compression tested specimen (Figure 4e), while sectioning at the center showed that there was a weak tendency for internal shear localization (Figure 12). Figure 13 shows a montage of the shear band close to the cracked surface band, with evidence of extensive cracking in association with the localized shear band; the major crack that has formed exhibits almost a straight line configuration. Thus, the lower tungsten volume fraction heavy alloy clearly exhibits good shear localization capability, in accord with the hypothesis that an alloy with a lower volume fraction of the solid tungsten phase should be more prone to shear localization.

Effects of Thermomechanical Treatment

Cold work-induced dislocation structures tend to be somewhat unstable at high temperatures, and rapid deformation may produce local thermal spikes at sites of particularly intense shear that literally anneal out the strengthening dislocation network. These regions might then constitute the nuclei for adiabatic shear bands. Thermomechanical processes of swaging, swaging and aging, rolling, extrusion, etc., provide the means for attaining the desirable characteristics, where shear localization could be promoted to a great extent. Thus, this aspect had to investigated in further details. The following suite of alloys was selected for this purpose:

Alloy 3. 90W-7Ni-3Fe alloy, pore free and homogeneous microstructure; normal sintering time of approximately 45 minutes.

Alloy 8. 91W-6Ni-3Co alloy; pore free and homogeneous microstructure; as sintered.

Alloy 9. 91W-6Ni-3Co alloy; pore free and homogeneous microstructure; 7% swaged and aged.

Alloy 10. 91W-6Ni-3Co alloy; pore free and homogeneous microstructure; 25% swaged and aged.

Alloy 11. 91W-4.4Ni-1.9Fe-2.7Co alloy; pore free and homogeneous microstructure; as sintered.

Alloy 12. 91W-4.4Ni-1.9Fe-2.7Co alloy; pore free and homogeneous microstructure; 20% swaged.

Alloy 13. 90W-7Ni-3Fe alloy; pore free and homogeneous microstructure; normal sintering time of 45 minutes, 10% swaged.

Alloy 14. 90W-7Ni-3Fe alloy; pore free and homogeneous microstructure; normal sintering time of 45 minutes, 24% swaged.

The effect of swaging on the possible tendency to localize shear was first investigated on a 91W-6Ni-3Co alloy. High strain rate compression tests were carried out on an as-sintered alloy (Alloy 8), a 7% swaged and aged material (Alloy 9), and a 25% swaged and aged alloy (Alloy 10). The microstructures of the alloys are shown in Figures 1h, 1i, and 1j, respectively, and the associated compressive stress-strain curves obtained during high strain rate deformation in Figure 28. The qualitative similarities between the curves, all of which exhibit initial hardening followed by subsequent softening, tend to suggest that the deformation mechanisms are somewhat similar. However, when the specimens were sectioned after they had been strained to approximately 0.45, and the shear bands subsequently observed in the SEM, they conveyed a totally different picture.

The montages of the internal shear bands for the as-sintered alloy, 7% swaged and aged alloy, and the 25% swaged and aged alloy are shown in Figures 14, 15, and 16, respectively. It can be observed that the as-sintered material (Alloy 8) shows practically no evidence of any shear localization, and its grains are deformed over a broad region forming a diffused band. The classic signs of shear localization, where the grains within the shear band are deformed at some angle to the grains outside the shear band, are generally absent. Thus, this material showed no shear localization tendency under the test conditions.

When we observe the shear band of the same alloy that has been 7% swaged and aged (Figure 15), we notice a tendency of some of the tungsten grains to deform at an angle when compared to other tungsten grains that are slightly away from that zone. These small localized zones do not occur in a straight-line fashion, but instead are somewhat stepped in nature. It was as though shear was trying to localize along the diagonal axis of the cross section in small zones. However, the tungsten grains were forced to align themselves further

to allow these steps to be incorporated as one intense shear band. This had not occurred as yet in the 7% swaged and aged alloy. In a sense, we were fortunate to witness this condition, which apparently just precedes the stage at which the intense shear localization does occur.

The situation is completely different when the same alloy has been 25% swaged and aged. This alloy exhibited intense adiabatic shear band formation and also localized cracking, as seen in Figure 16; in this case, the cracked shear band was oriented in a straight-line configuration. Figure 17 is high magnification SEM photomicrograph showing the details of the cracked region. Interestingly, the crack that was associated with the shear band showed evidence of a crust-like material that was present inside the crack. There was also evidence of spheroidal particles (with somewhat jagged edges) within the intense shear band crack. The crust-like material within the crack was essentially an alloy of tungsten, nickel, and cobalt, while the jagged sphere was pure tungsten. It certainly would seem improbable that the temperature rise in the shear zone was so great that it could melt tungsten. It is possible that after the crack was formed a small tungsten grain was entrapped in the crack and was milled between the two opposing walls of the crack itself. However, the presence of the crust-like material, which also exhibited small miniscules in certain areas, would tend to indicate that the temperature rise was at least sufficient to melt an alloy of tungsten, nickel, and cobalt. Whether the melting (if any) was due to the localized heating during the band formation or if it occurred due to the frictional heat that was generated after the crack had already formed is not very clear.

We can therefore conclude that the thermomechanical process of swaging and aging has a great influence on the tendency of the alloy to localize shear. To provide a quantitative description of the different shear band mechanisms involved in the three alloys discussed above, the aspect ratio of the tungsten grains was plotted as a function of the distance of the grain from the core of the shear band. This is shown in Figure 26. The details of the experimental process were discussed earlier.

The 25% swaged and aged alloy shows a single shear band lying in a straight-line configuration. The core of the shear band, which was dispersed over a very narrow width (10 μm), includes both cracks and heavily deformed tungsten grains with aspect ratios that exceed 30. Rapid deformation of the 7% swaged and aged alloy produced several shear bands that were not totally aligned into a straight-line configuration. The shear bands had a thickness of approximately 40 μm, and the aspect ratio of the grains was less than 25. The undeformed alloy also showed similar characteristics compared to the 7% swaged and aged alloy, except for the fact that the aspect ratio of the deformed tungsten grains was in the range of 20 μm, and the overall band was very diffuse.

The presence of very narrow and unstable shear bands is clearly reflected in Figure 26. It is postulated that the localization of the shear band over a narrow strip is facilitated by the presence of pre-deformed tungsten particles. Study of the macroscopic shear band sector which bounds the "core" (highly deformed) band suggests that there is a critical aspect ratio of the pre-deformed tungsten grains that lies between 1 and 1.3, the precise value of which may determine if the material will exhibit a single shear band or several shear bands during dynamic compression.

This set of experiments shows that thermomechanical processing such as swaging and aging can definitely enhance a material's propensity to shear localization. The question remains: is this behavior alloy specific or generic? In other words, would swaging affect a different alloy in a similar manner and promote its shear localization tendency? To test this, we carried out high strain rate compression tests on an alloy system that had a composition of 91W-4.4Ni-1.9Fe-2.7Co. Interestingly, the microstructures of these alloys were quite different from those that had a composition of 91W-6Ni-3Co. The alloys with the W-Ni-Co had large tungsten grains (around 20 μm) dispersed in a matrix of W-Ni-Co. However, also clearly seen within the matrix were fine (submicron sized) precipitates of tungsten. The W-Ni-Fe-Co based alloy had a microstructure in which only the large tungsten grains were dispersed in the matrix alloy (Figure 1k). Thus, this new alloy system not only provided a different composition, but also a different microstructure compared to the W-Ni-Co- based alloys. One of the alloys tested was in the as- sintered condition, and the other was a 20% swaged alloy. Both materials were tested in high strain rate compression. The tested materials were sectioned, mounted, and polished in the manner described earlier.

The shear band montages for the tests carried out on the as-sintered and the swaged materials are shown in Figures 18 and 19, respectively. It is again clear from the figures that the as-sintered alloy does not exhibit a strong shear localization tendency, while the swaged version showed shear band formation and attendant localized cracking.

Thus, it could be concluded that swaging of the material does generally enhance shear localization. Further experiments were carried out on a 90W-7Ni-3Fe alloy, which is the only alloy that has so far shown a tendency to localize shear in the as-sintered condition. Two 90W-7Ni-3Fe alloys swaged 10% (Alloy 13) and 24% (Alloy 14) were tested in high strain rate compression. Both alloys showed shear-induced cracking on the outside surface of the compression tested specimen. Figures 20 and 21 show the montages of the shear bands of the 10% and 24% swaged alloys such that the polished surface lies in a plane which includes the external crack. It is clear that both materials were capable of shear localization and cracking. However, since the unswaged alloy of this material also showed signs of shear localization, it is difficult to say whether shear localization actually was enhance because of the swaging

process. By contrasting Figures 8, 20, and 21, it can only be stated qualitatively that the 24% swaged alloy shows a straight, clear crack over the entire region of the montage. The unswaged alloy does show large cracks at the two ends of the montage, but in the section between the large cracks the shear band is localized but not associated with a straight and narrow crack.

CONCLUSIONS

Research performed in the first year has demonstrated that appropriate microstructural modifications can influence the shear localization tendencies of tungsten heavy alloys. It was determined that the shear localization propensity was increased by:

1. A porous and inhomogeneous microstructure.
2. Smaller grain size.
3. Lower volume fraction of tungsten.
4. Increased amount of swaging (or swaging/aging).

PRESENTATIONS AND PUBLICATIONS

During the course of the first year, one paper went to press, and two others have been accepted for presentation and subsequent publication:

1. "Shear Localization in Tungsten Heavy Alloys," by A. Bose, H. R. Couque, and J. Lankford, Jr., Advances in Powder Metallurgy & Particulate Materials - 1992: Non-Ferrous Materials, Vol. 6, 1992. (in press)

2. "Influence of Microstructure on Shear Localization in Tungsten Heavy Alloys," by A. Bose, H. R. Couque, and J. Lankford, Jr, Accepted for Presentation and Publication at the International Conference in Tungsten and Tungsten Alloys, Nov. 15-18, 1992, Arlington, VA.

3. "Role of Swaging on Dynamic Deformation of Tungsten," by H. R. Couque, A. Bose, and J. Lankford, Jr., Accepted for Presentation and Publication at the International Conference in Tungsten and Tungsten Alloys, Nov. 15-18, 1992, Arlington, VA.

FUTURE

Efforts in the second year will concentrate on refining the Mode II shear technique and on the processing of several adiabatic shear prone matrices. Dislocation and precipitate structures in some of the promising alloys will be characterized, as appropriate, by TEM. Feedback from the screening tests and damage characterization will be used to carry out further alloy and/or process modifications.

REFERENCES

1. L. S. Magness and T. G. Farrand, "Deformation Behavior and its Relationship to the Penetration Performance of High Density KE Penetrator Materials," Proc. 1990 Army Science Conf., Durham, N. C., May 1990, pp. 149-164.

2. N. M. Parikh, "Development and Application of a Theory of Plastic Deformation of Cemented Alloys," Armor Research Foundation Technical Report, Watertown Arsenal, Watertown, MA, Report ARF 2182-12, WAL 372/32, March 23, 1961.

3. E. I. Larsen and P. C. Murphy, "Characteristics and Applications of High-Density Tungsten-Based Composites," Canadian Mining Metall. Bull., 58, (1965), 413-420.

4. F. V. Lenel, Powder Metallurgy Principles and Applications, (Princeton, NJ: Metal Powder Industries Federation, 1980). 5. E. Ariel, J. Barta, and D. Brandon, "Preparation and Properties of Heavy Metals," Powder Metall. Int., 5, (1973), 126-129.

6. J. Lankford, H. Couque, A. Bose, and R. M. German, "Dynamic Deformation and Failure of Tungsten Heavy Alloys," Tungsten and Tungsten Alloys - Recent Advances, Eds. A. Crowson and E. S. Chen, TMS, Warrandale, PA, pp. 151-159, 1991.

7. U.S. Lindholm, "Some Experiments with the Split Hopkinson Pressure Bar," J. Mech. Phys. Solids, Vol. 12, p. 317, 1964.

8. T. Weerasooriya, P. A. Beaulieu, and R. Swanson, "Deformation and Failure of 93W-5Ni-2Fe at High Strain Rate Shear Loading," U. S. Army MTL-TR-92-19, April 1992.

9. A. Bose and R. M. German, "Sintering Atmosphere Effects on the Tensile Properties of Tungsten Heavy Alloys," Metall. Trans., Vol. 19A, pp. 2467-2476.

10. A. Bose, H. Couque, and J. Lankford, Jr., "Development and Properties of New Tungsten Based Composites for Penetrators," Inter. J. Powder Metall. (in press)

Table 1. Alloy Designation and Characteristics.

Alloy Designation	Alloy Composition in weight percent	Comments on Processing and/or Microstructure
Alloy 1	90W-8Ni-2Fe	pore free and homogeneous microstructure; normal sintering time of 45 minutes
Alloy 2	90W-7Ni-3Fe	porous and inhomogeneous microstructure
Alloy 3	90W-7Ni-3Fe	pore free and homogeneous microstructure; normal sintering time of 45 minutes
Alloy 4	90W-7Ni-3Fe	pore free and homogeneous microstructure; normal sintering time of 240 minutes
Alloy 5	90W-7Ni-3Fe	pore free and homogeneous microstructure; sintering time of 800 minutes
Alloy 6	95W-3.5Ni-1.5Fe	pore free and homogeneous microstructure; normal sintering time of 45 minutes
Alloy 7	86W-9.8Ni-4.2Fe	pore free and homogeneous microstructure; normal sintering time of 45 minutes
Alloy 8	91W-6Ni-3Co	pore free and homogeneous microstructure; as sintered
Alloy 9	91W-6Ni-3Co	pore free and homogeneous microstructure; 7% swaged and aged
Alloy 10	91W-6Ni-3Co	pore free and homogeneous microstructure; 25% swaged and aged
Alloy 11	91W-4.4Ni-1.9Fe-2.7Co	pore free and homogeneous microstructure; as sintered
Alloy 12	91W-4.4Ni-1.9Fe-2.7Co	pore free and homogeneous microstructure; 20% swaged
Alloy 13	90W-7Ni-3Fe	pore free and homogeneous microstructure; normal sintering time of 45 minutes, 10% swaged
Alloy 14	90W-7Ni-3Fe	pore free and homogeneous microstructure; normal sintering time of 45 minutes, 24% swaged

Table 2. Microstructural Characteristics of Several Alloys.

Alloy	Mean Intercept Length, μm	Volume of solid phase, %	Contiguity	Connectivity	Dihedral Angle
1	23.5 ± 9.3	74.2	0.195 ± 0.03	0.845 ± 0.01	36.0° ± 14.3°
3	17.8 ± 8.2	75.9	0.293 ± 0.01	0.938 ± 0.03	40.5° ± 21.8°
4	38.7 ± 16.8	76.3	0.215 ± 0.03	0.665 ± 0.05	39.3° ± 22.3°
5	59.8 ± 31.1	81.1	0.178 ± 0.06	0.613 ± 0.11	32.8° ± 19.1°
6	26.0 ± 15.2	80.1	0.393 ± 0.06	1.328 ± 0.13	40.8° ± 25.4°
7	19.9 ± 6.3	69.4	0.243 ± 0.04	0.845 ± 0.08	51.0° ± 25.6°

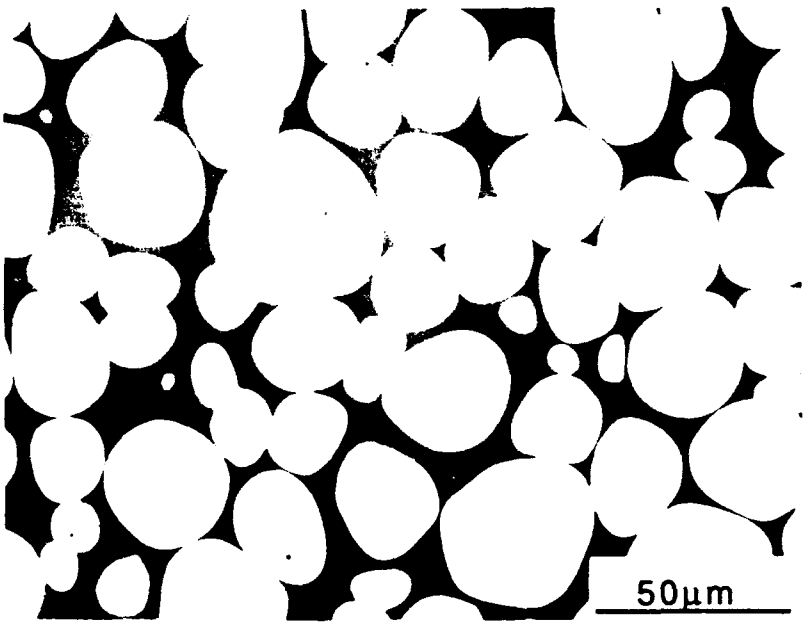

Figure 1a. **Alloy 1 (90W-8Ni-2Fe); pore free and homogeneous microstructure; normal sintering time of 45 minutes.**

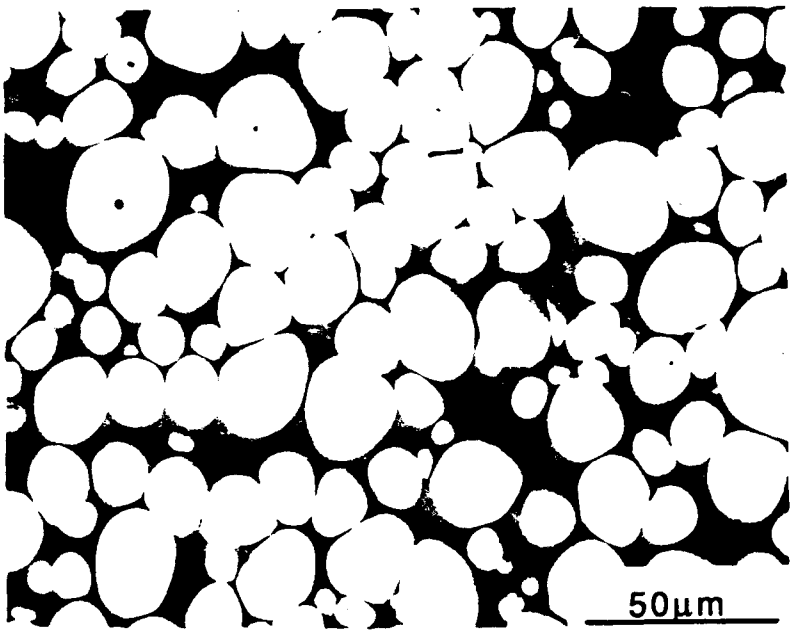

Figure 1b. **Alloy 2 (90W-7Ni-3Fe); porous and inhomogeneous microstructure.**

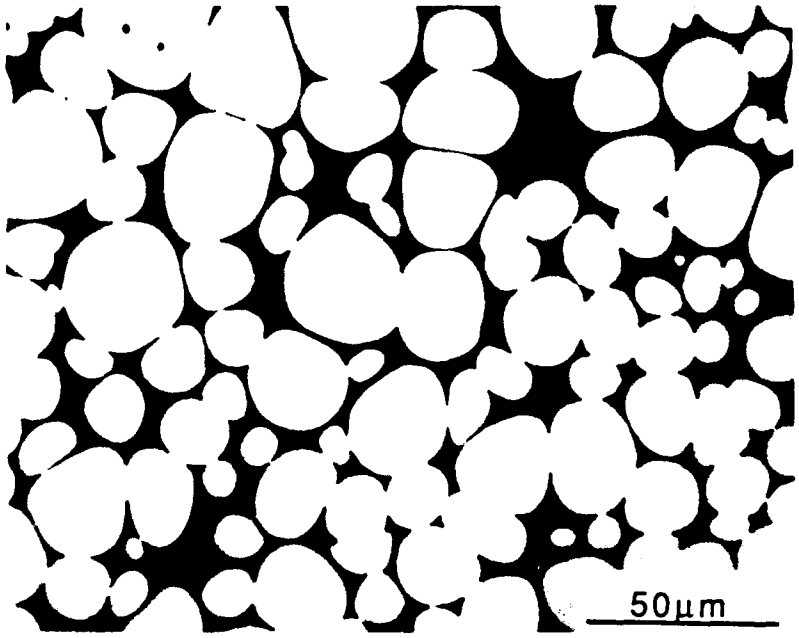

Figure 1c. Alloy 3 (90-7Ni-3Fe); pore free and homogeneous microstructure; normal sintering time of 45 minutes.

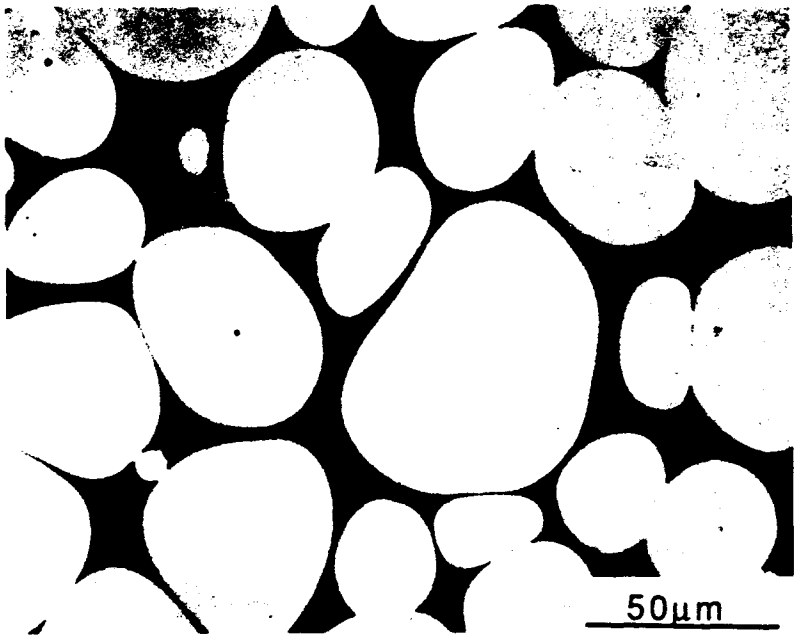

Figure 1d. Alloy 4 (90-7Ni-3Fe); pore free and homogeneous microstructure; normal sintering time of 240 minutes.

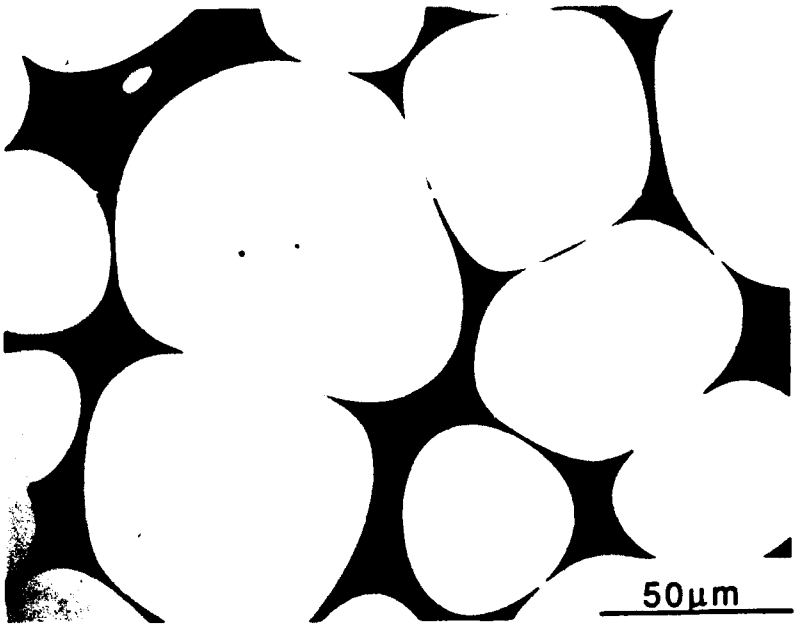

Figure 1e. Alloy 5 (90-7Ni-3Fe); pore free and homogeneous microstructure; sintering time of 800 minutes.

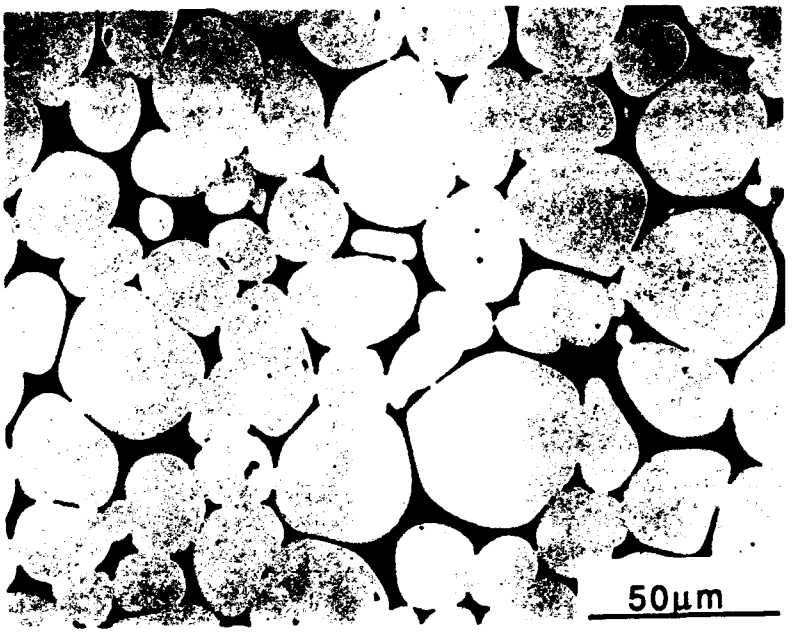

Figure 1f. Alloy 6 (95W-3.5Ni-1.5Fe); pore free and homogeneous microstructure; normal sintering time of 45 minutes.

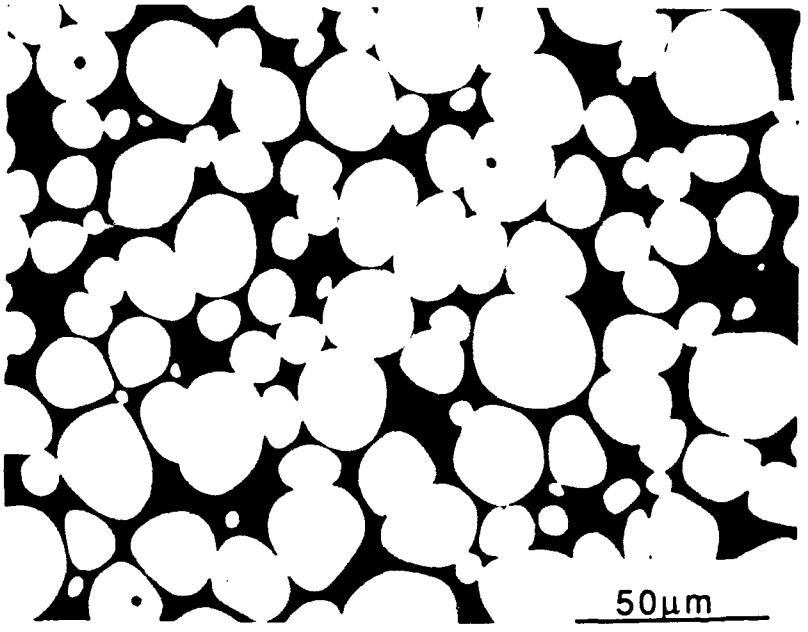

Figure 1g. **Alloy 7 (86W-9.8Ni-4.2Fe); pore free and homogeneous microstructure; normal sintering time of 45 minutes.**

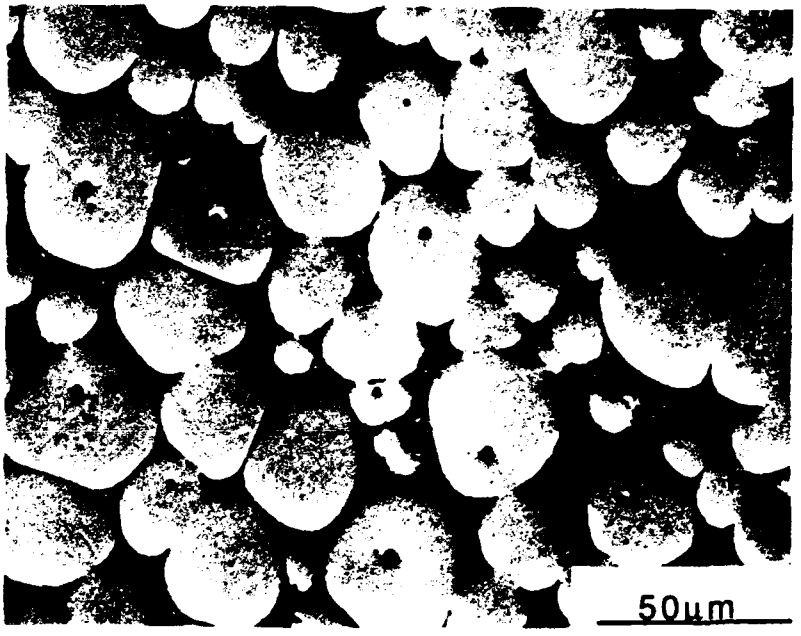

Figure 1h. **Alloy 8 (91W-6Ni-3Co); pore free and homogeneous microstructure; as sintered.**

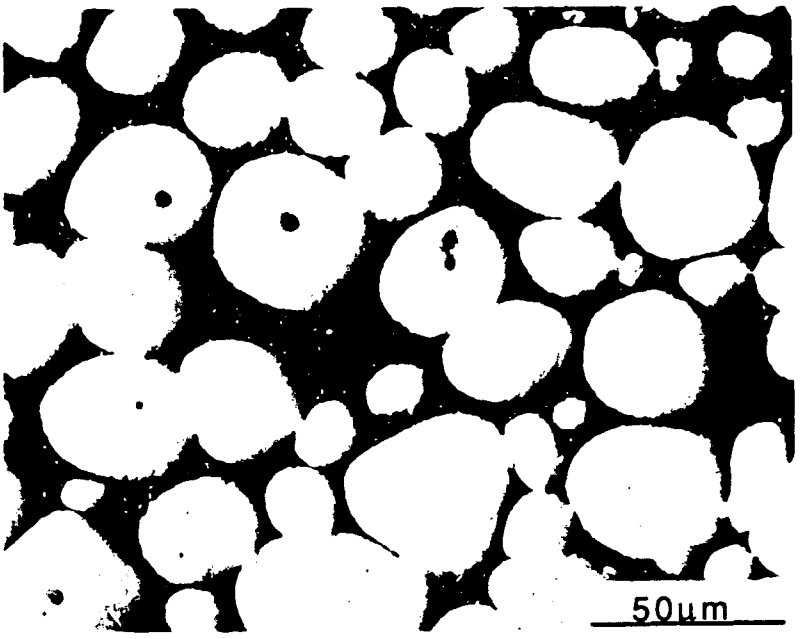

Figure 1i. Alloy 9 (91W-6Ni-3Co); pore free and homogeneous microstructure; 7% swaged and aged.

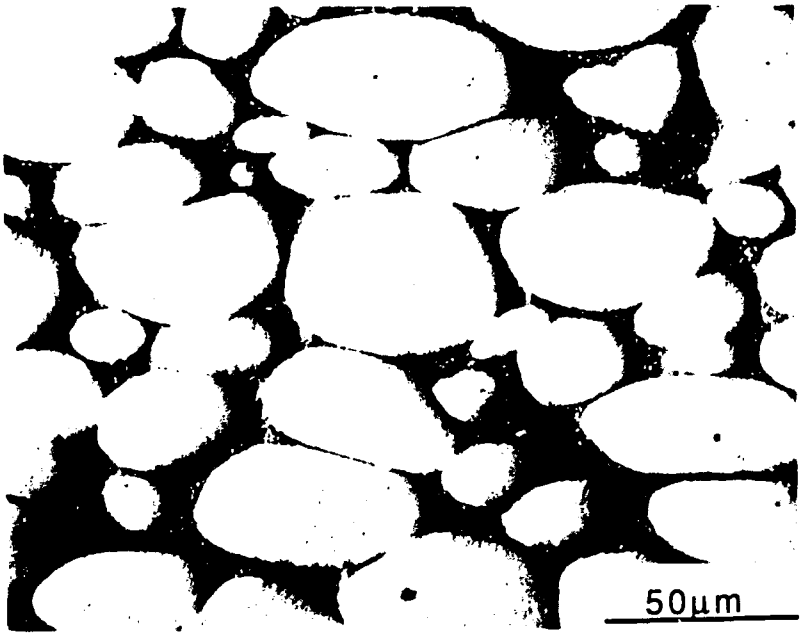

Figure 1j. Alloy 10 (91W-6Ni-3Co); pore free and homogeneous microstructure; 25% swaged and aged.

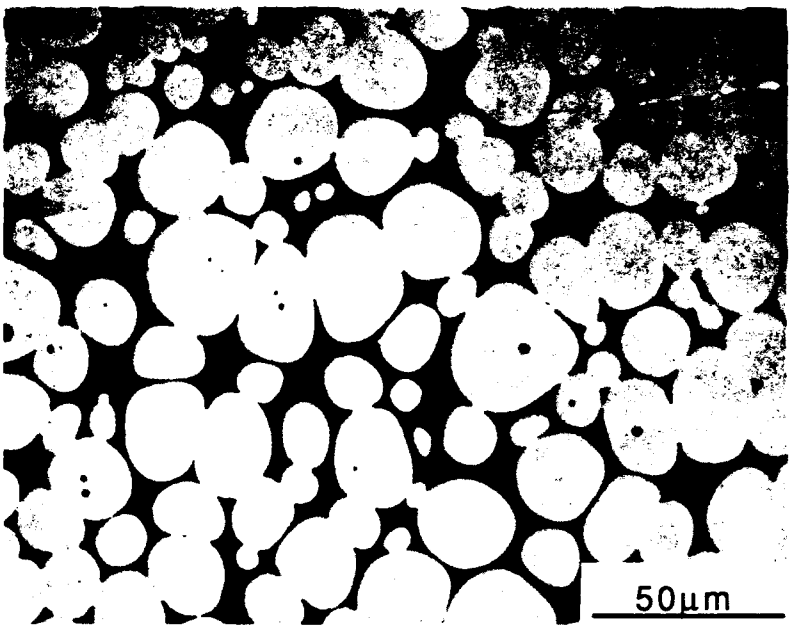

Figure 1k. **Alloy 11 (91W-4.4Ni-1.9Fe-2.7Co); pore free and homogeneous microstructure; as sintered.**

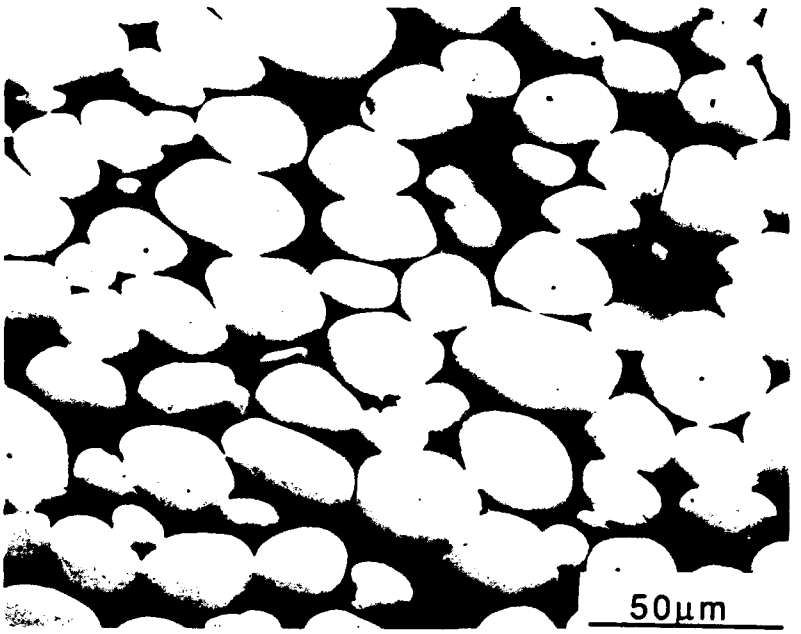

Figure 1l. **Alloy 12 (91W-4.4Ni-1.9Fe-2.7Co); pore free and homogeneous microstructure; 20% swaged.**

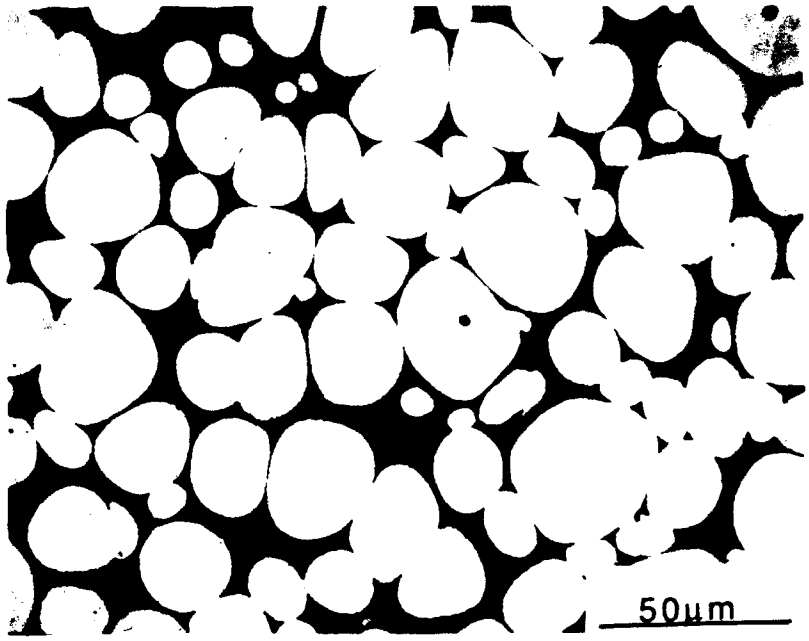

Figure 1m. Alloy 13 (90W-7Ni-3Fe); pore free and homogeneous microstructure; normal sintering time of 45 minutes, 10% swaged.

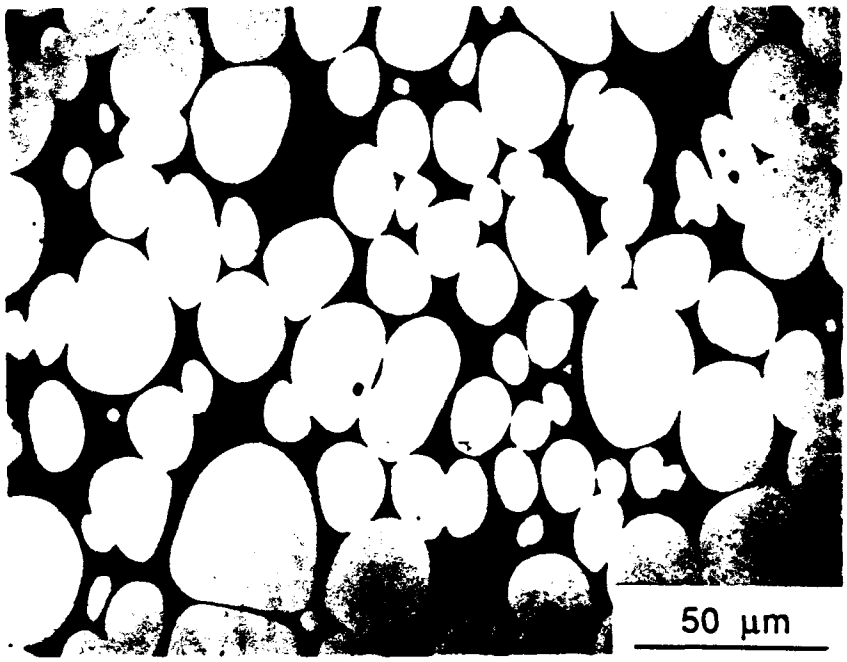

Figure 1n. Alloy 14 (90W-7Ni-3Fe); pore free and homogeneous microstructure; normal sintering time of 45 minutes, 24% swaged.

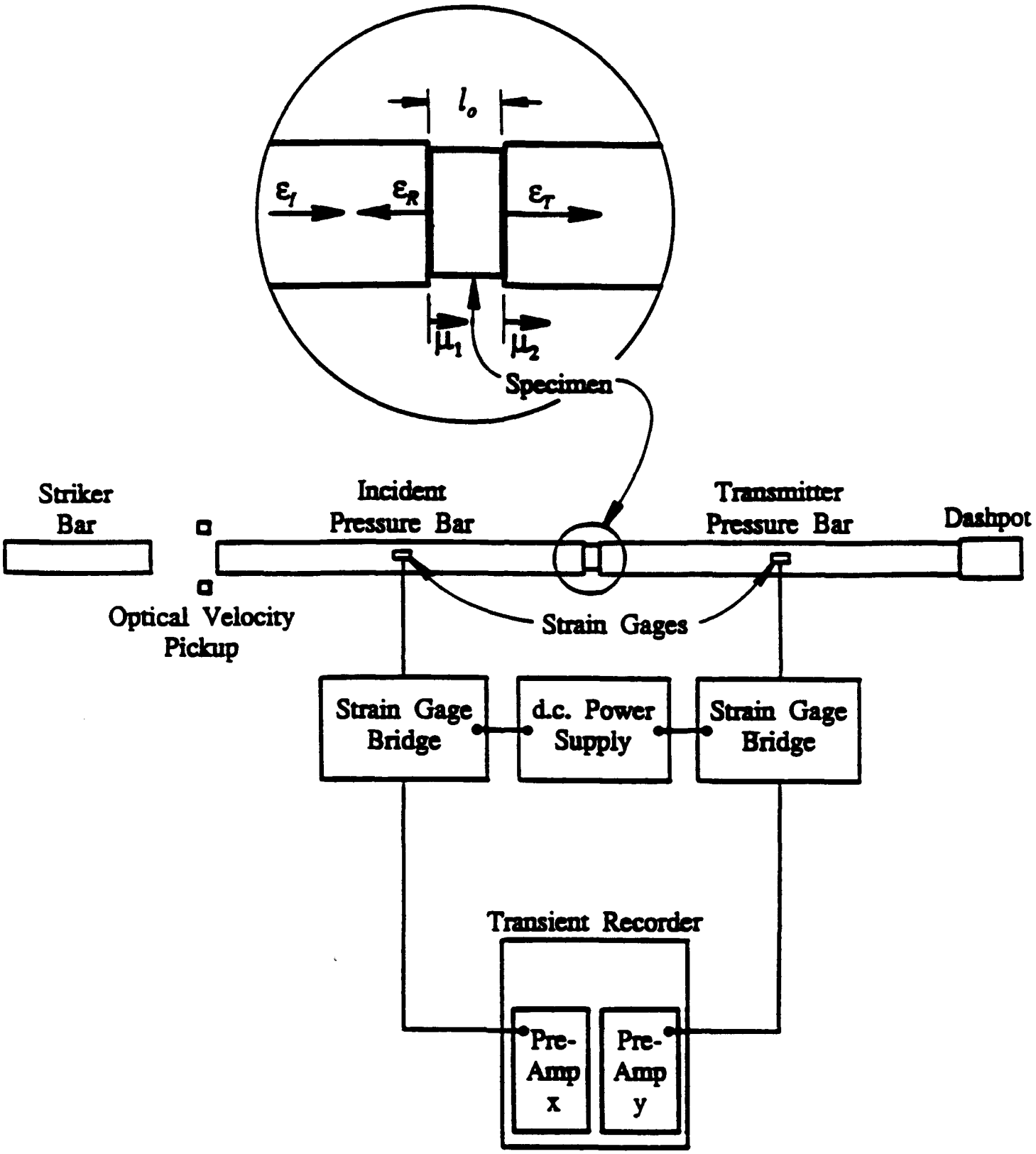

Figure 2. Compression split Hopkinson Pressure bar setup.

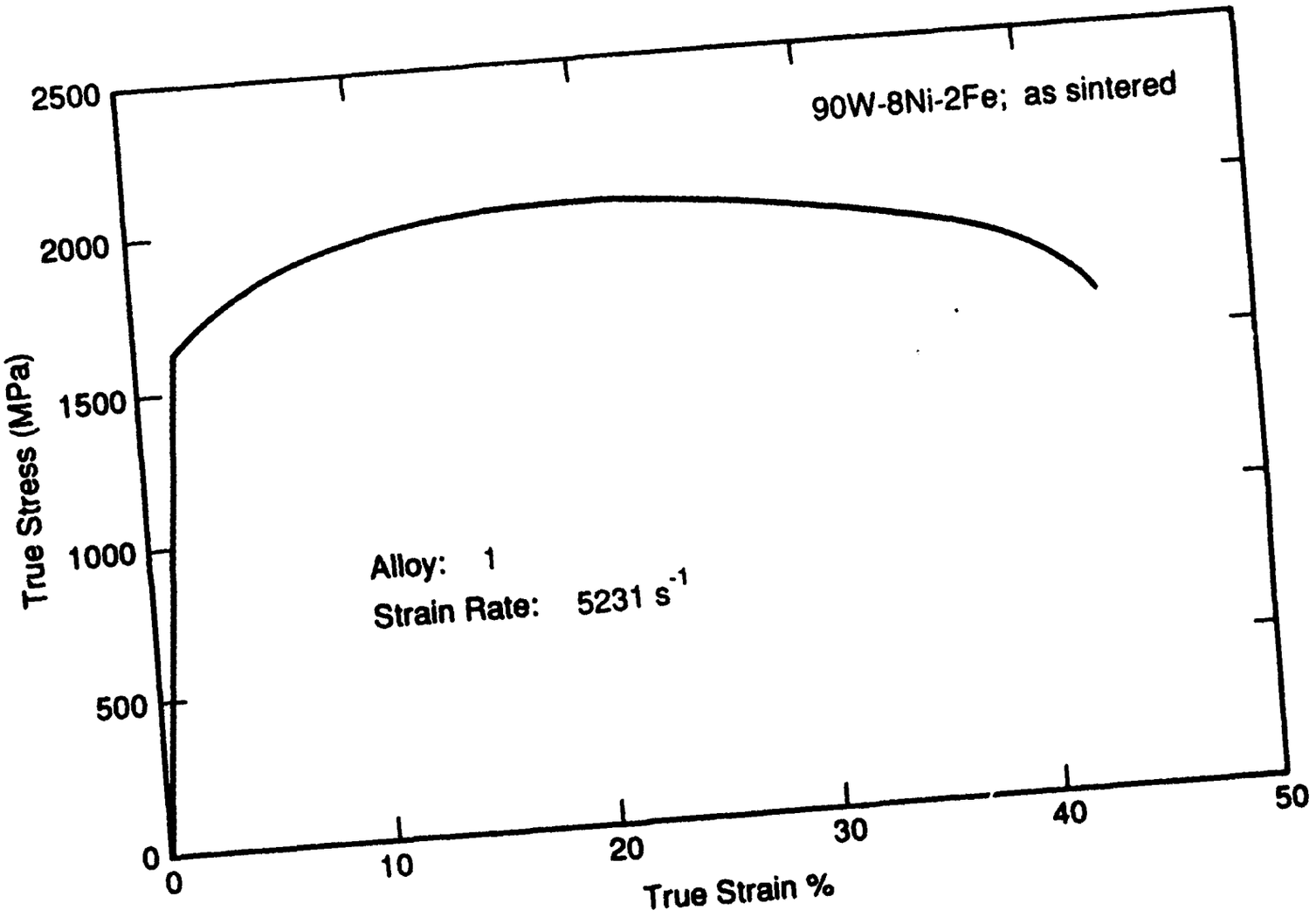

Figure 3a. Compressive stress-strain curve for Alloy 1.

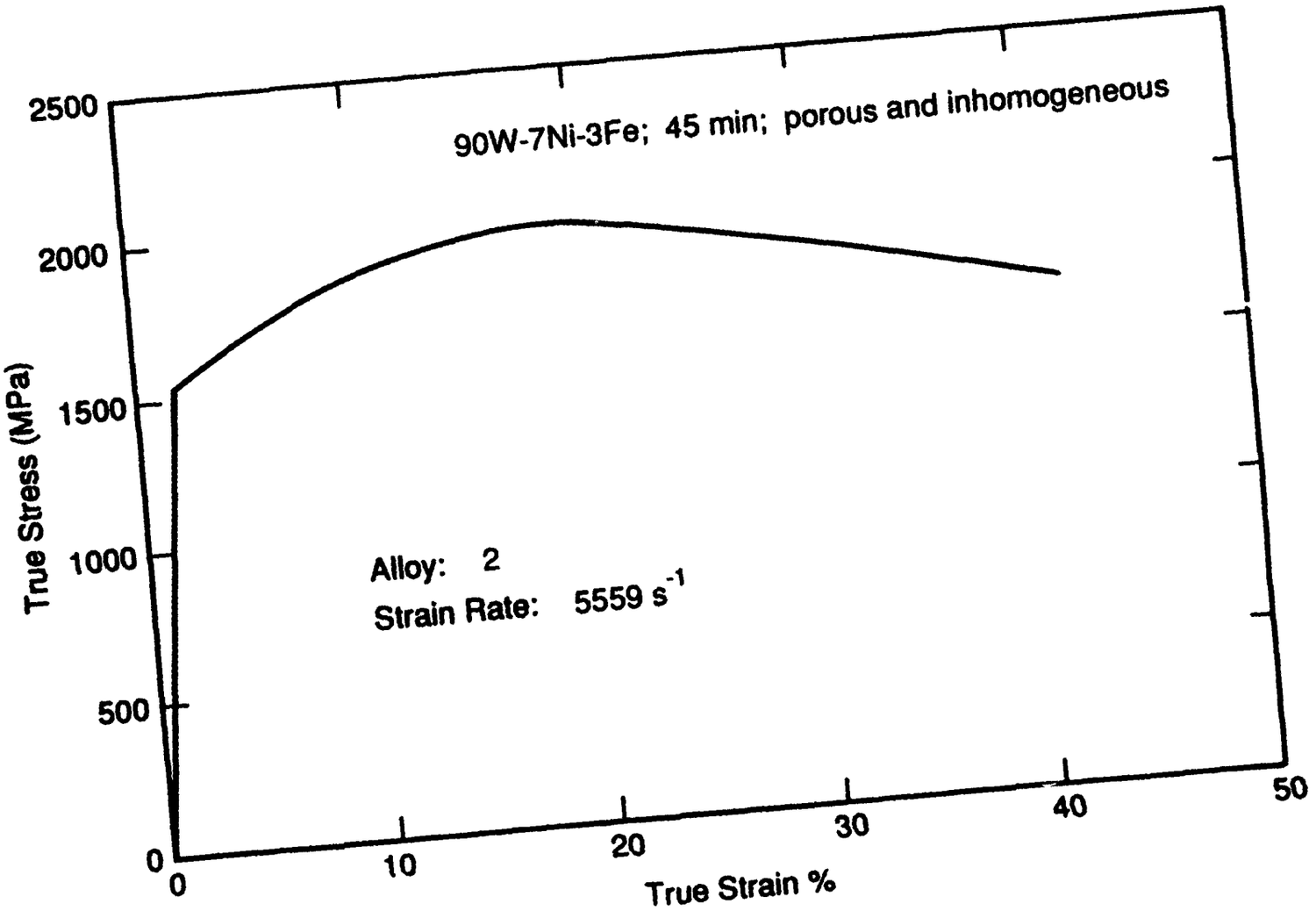

Figure 3b. Compressive stress-strain curve for Alloy 2.

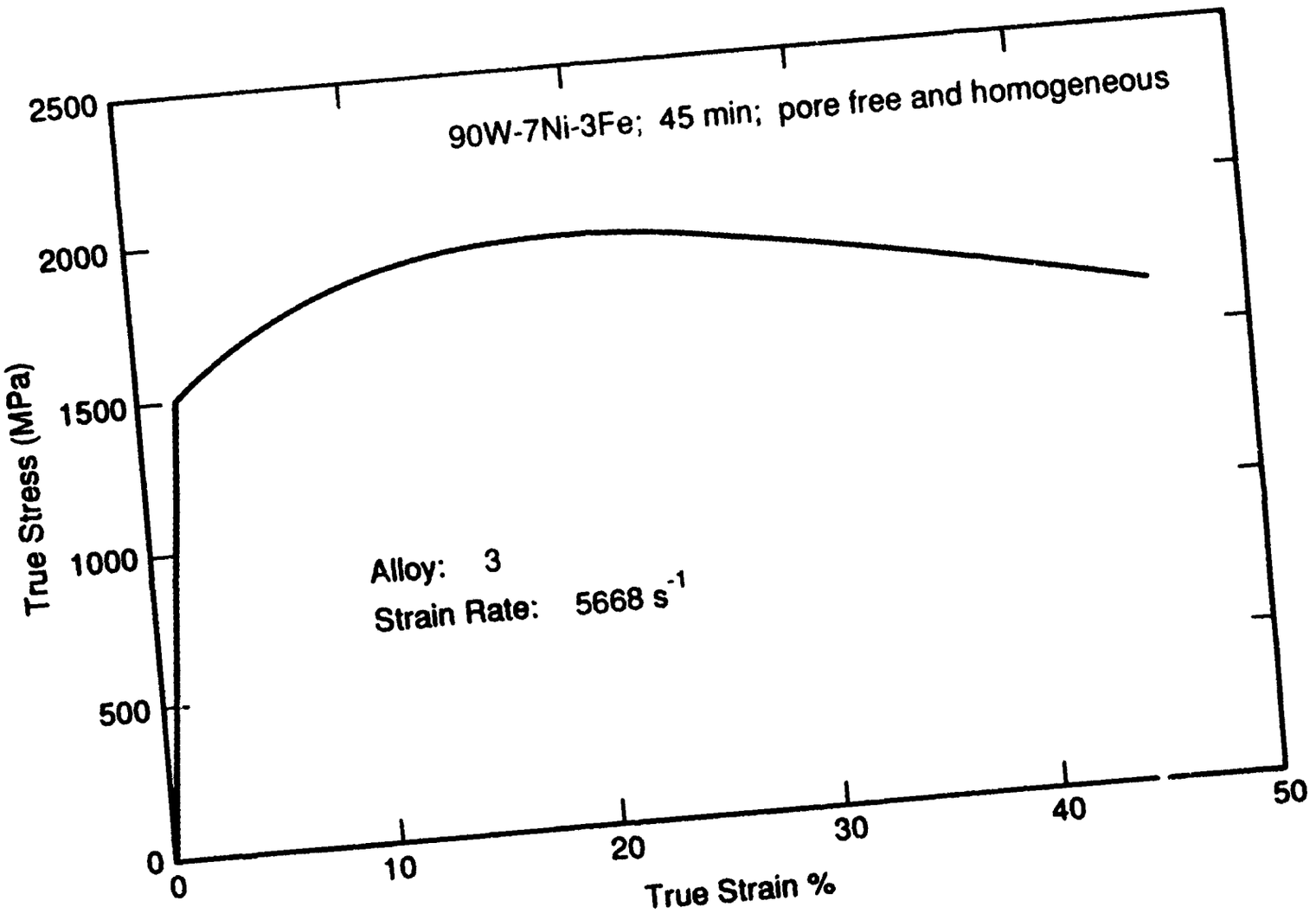

Figure 3c. Compressive stress-strain curve for Alloy 3.

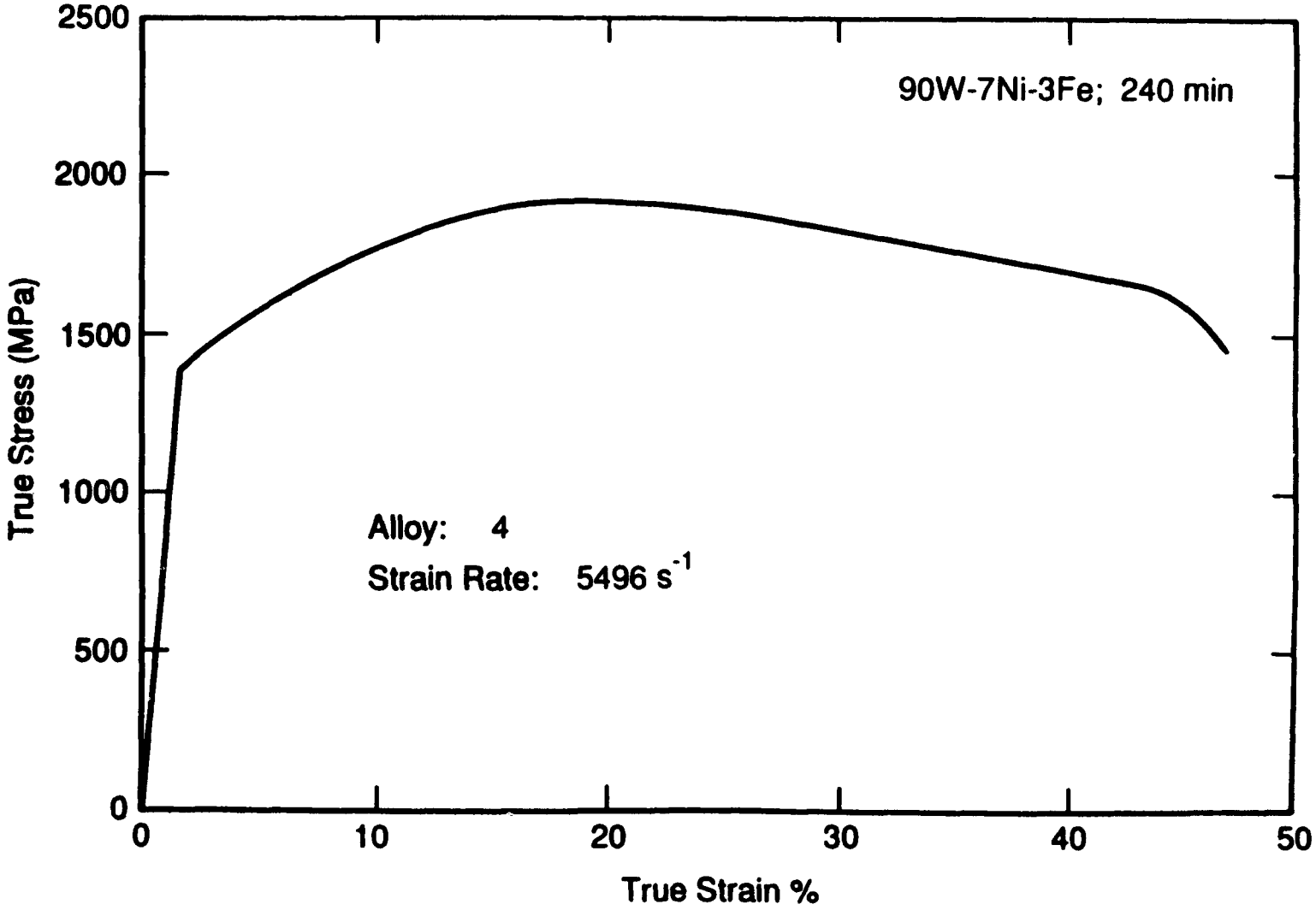

Figure 3d. Compressive stress-strain curve for Alloy 4.

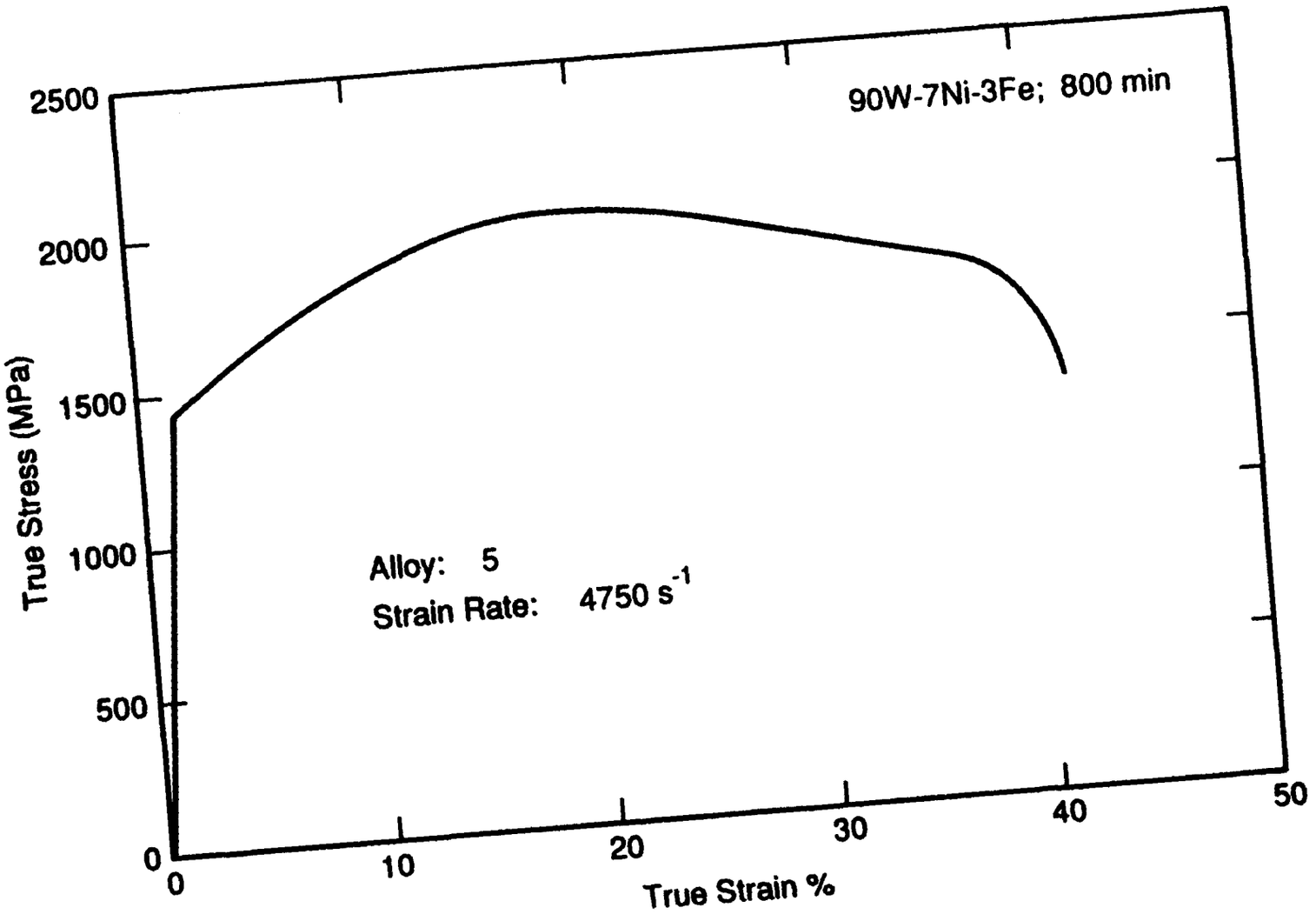

Figure 3e. Compressive stress-strain curve for Alloy 5.

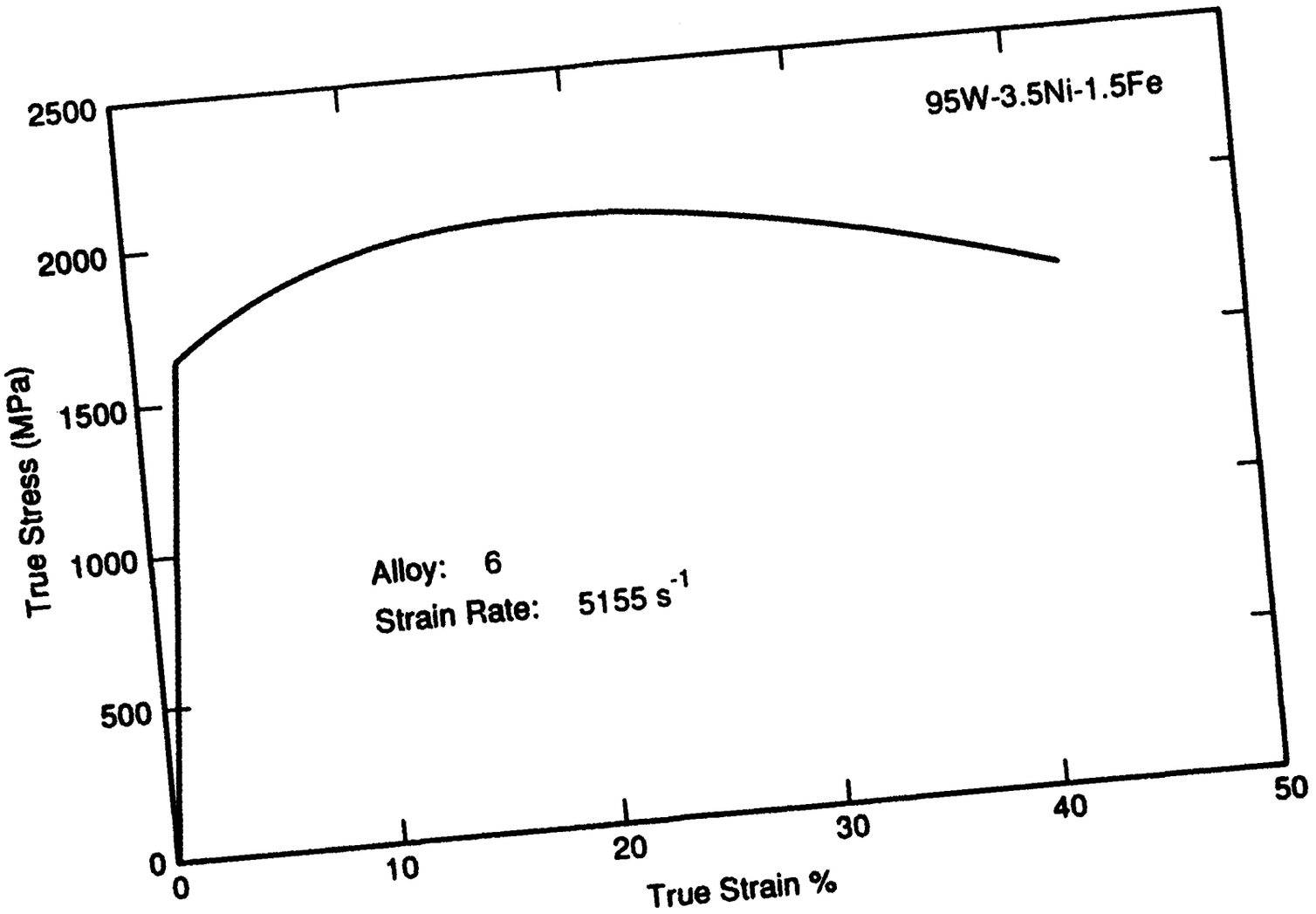

Figure 3f. Compressive stress-strain curve for Alloy 6.

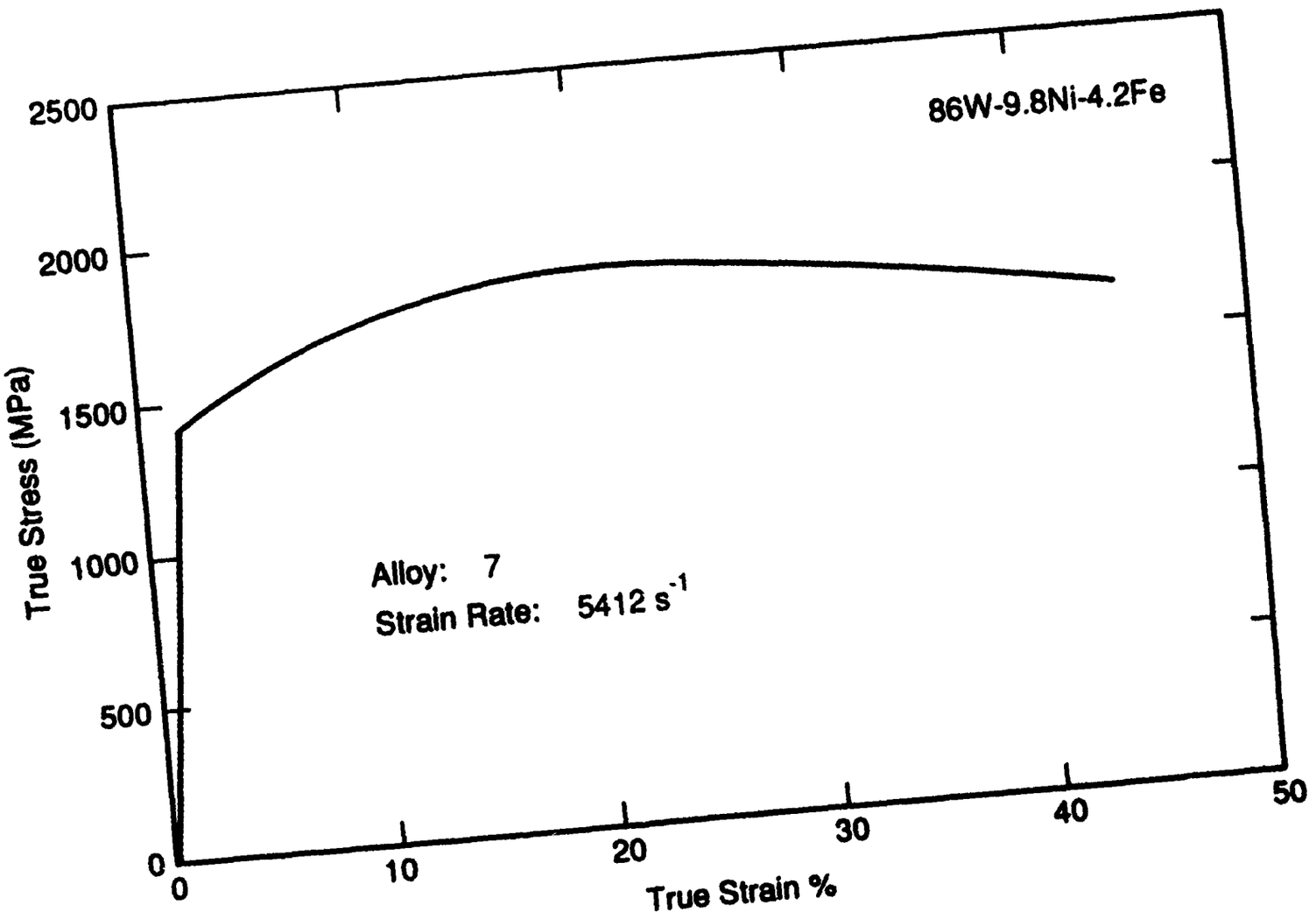

Figure 3g. Compressive stress-strain curve for Alloy 7.

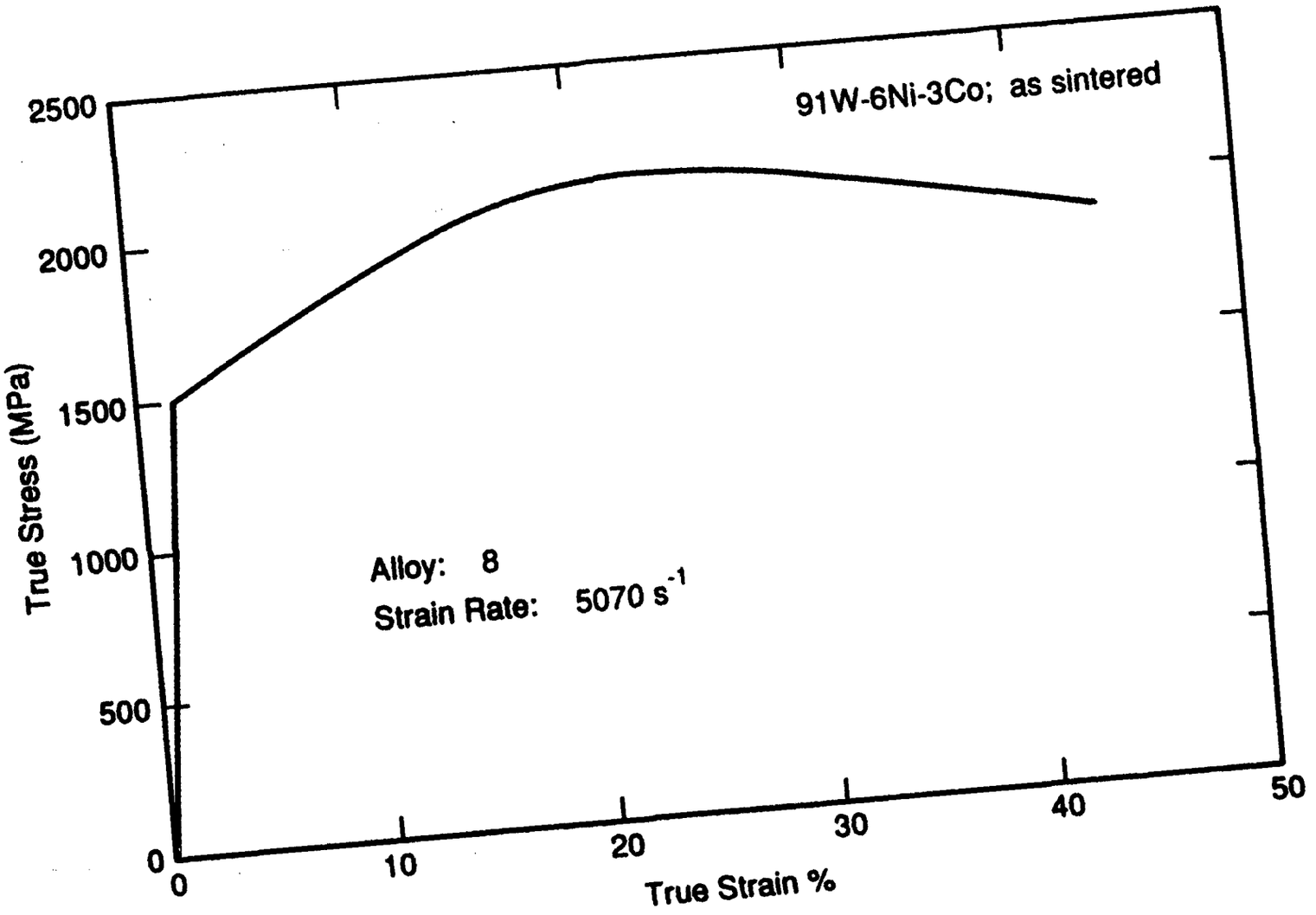

Figure 3h. Compressive stress-strain curve for Alloy 8.

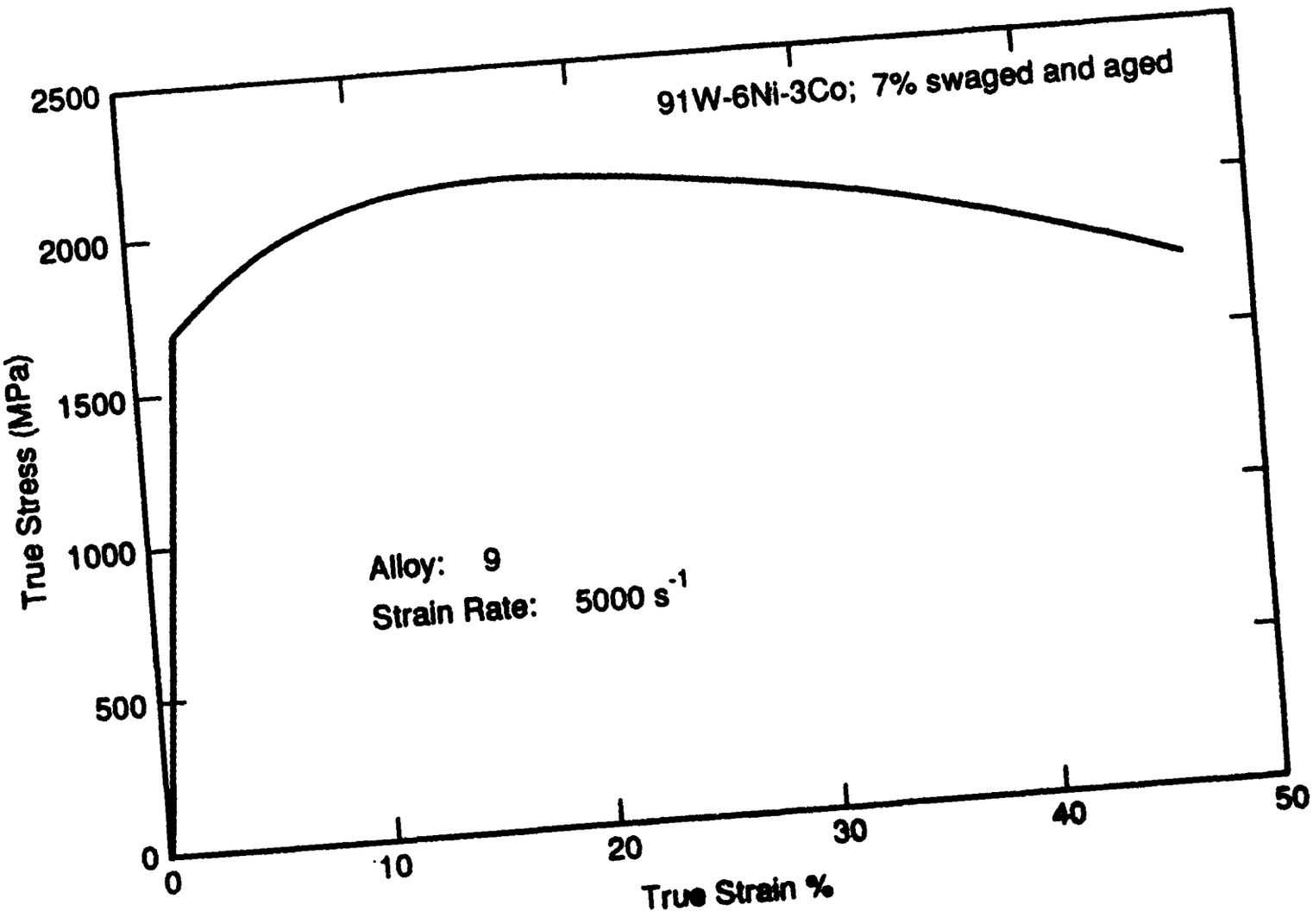

Figure 3i. Compressive stress-strain curve for Alloy 9.

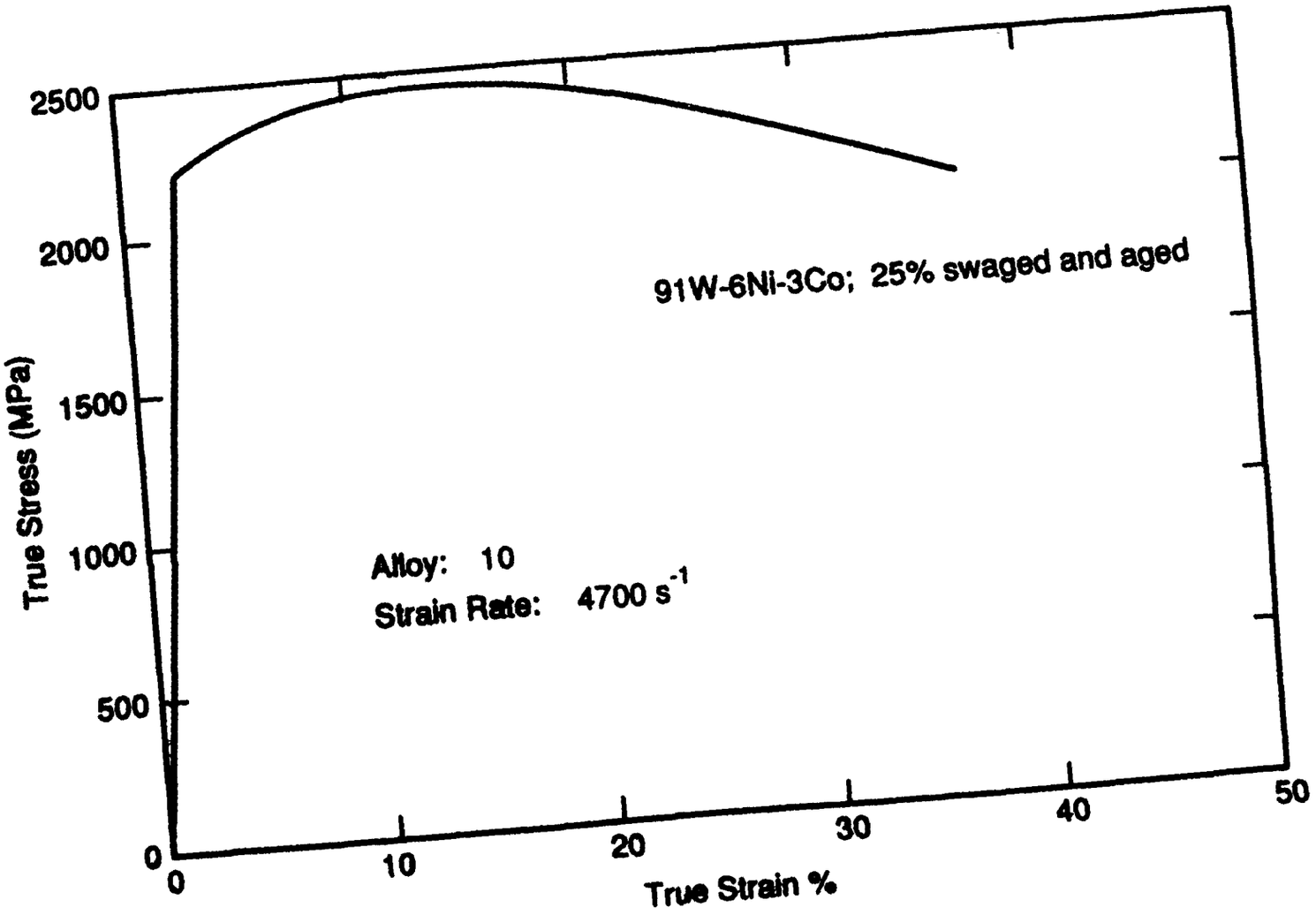

Figure 3j. Compressive stress-strain curve for Alloy 10.

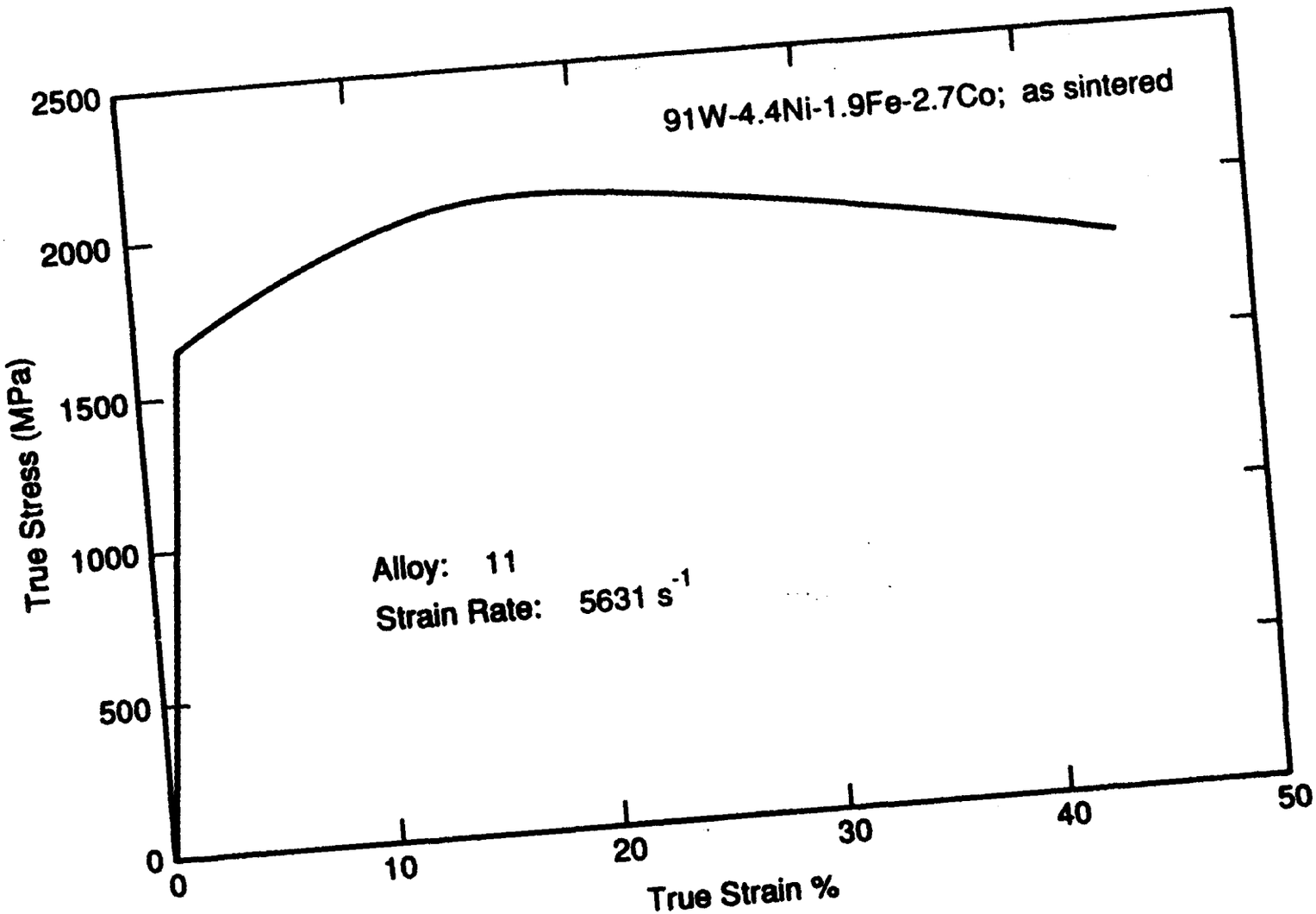

Figure 3k. Compressive stress-strain curve for Alloy 11.

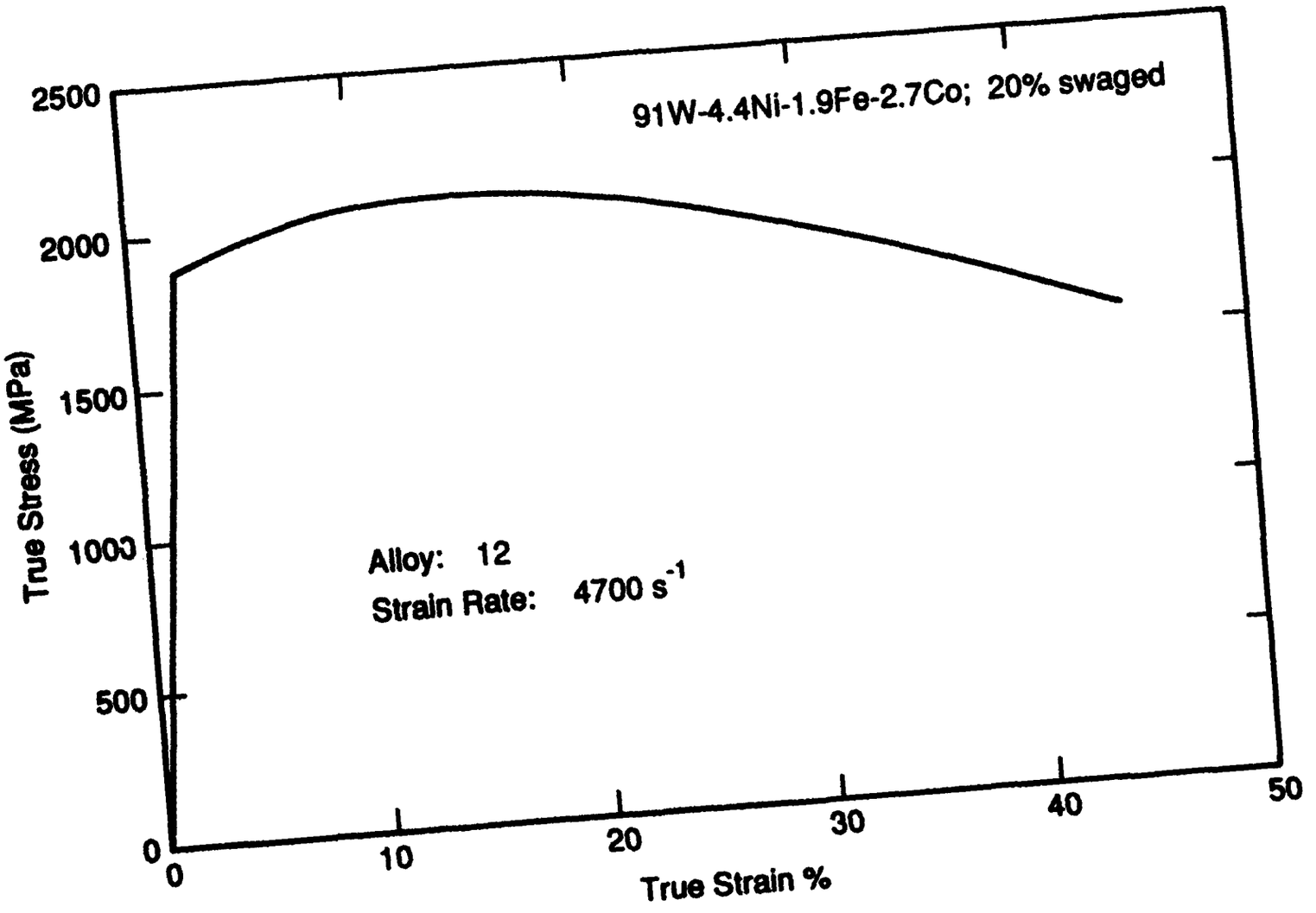

Figure 31. Compressive stress-strain curve for Alloy 12.

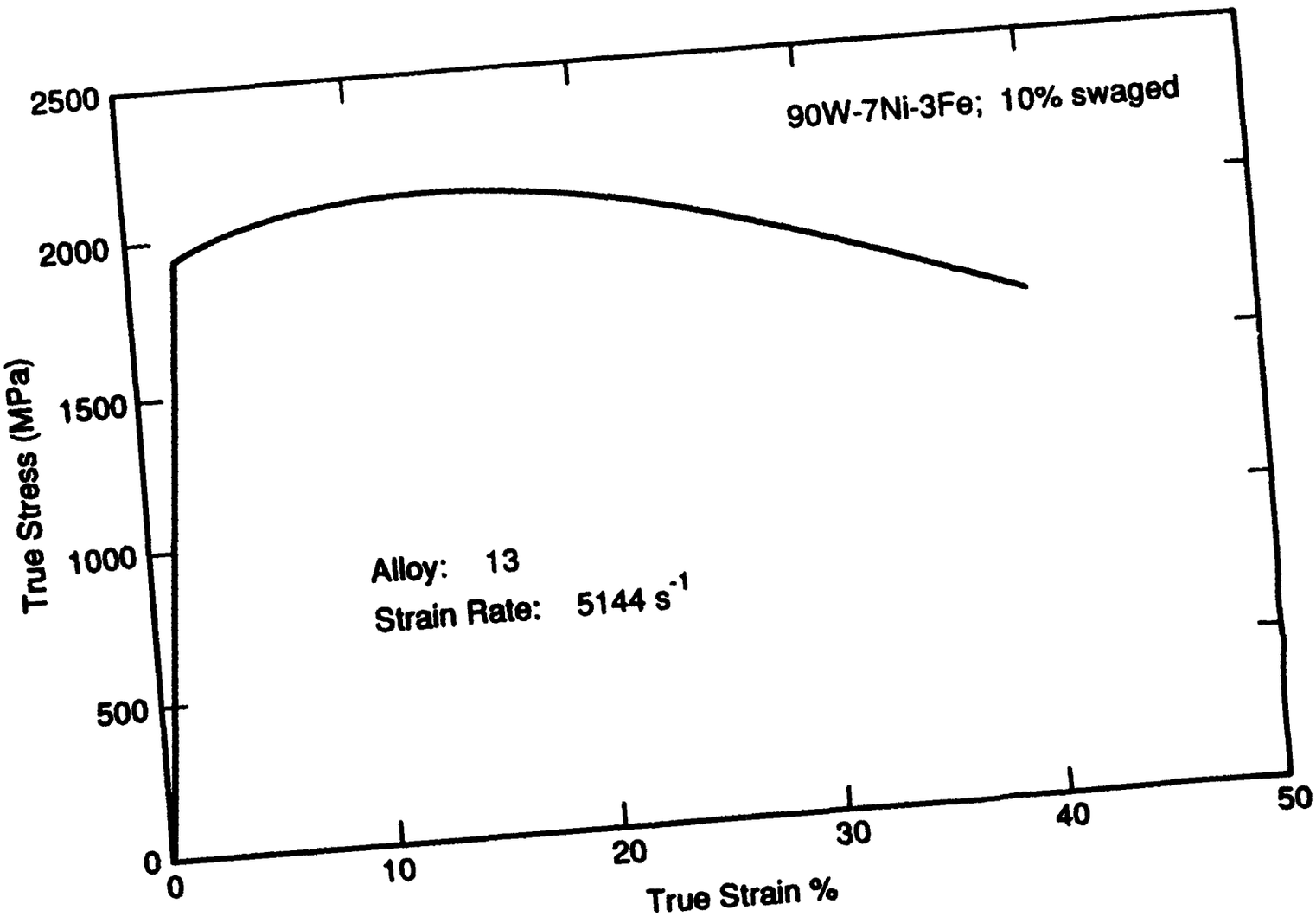

Figure 3m. Compressive stress-strain curve for Alloy 13.

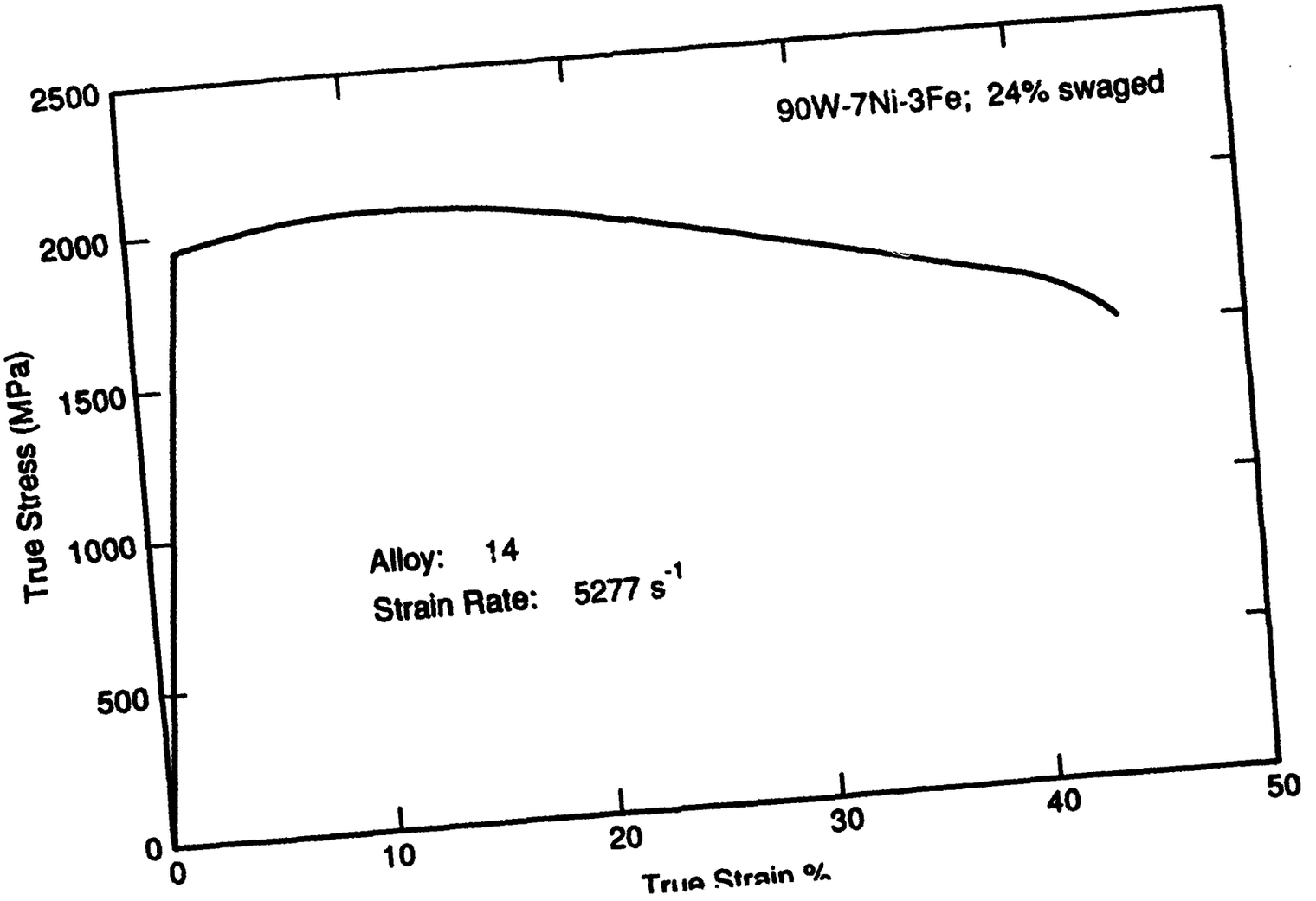

Figure 3n. Compressive stress-strain curve for Alloy 14.

Figure 4a. External shear crack, Alloy 3.

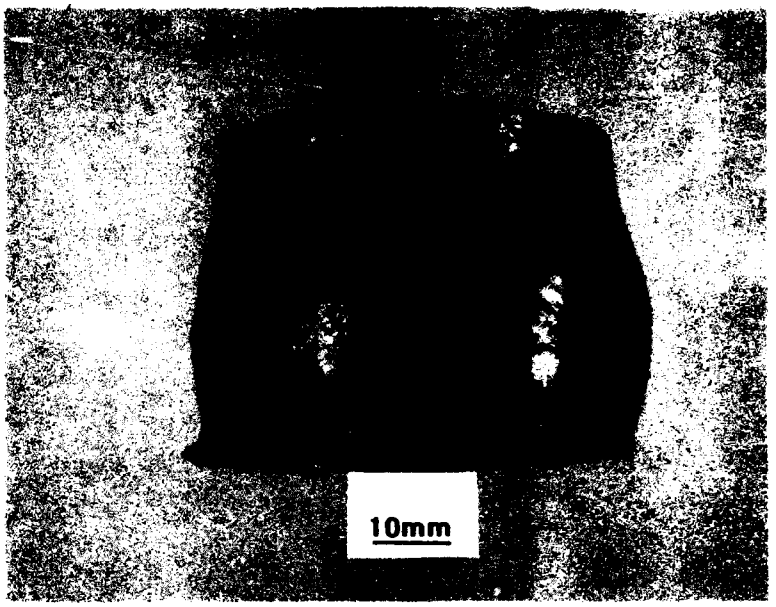

Figure 4b. External shear crack, Alloy 13.

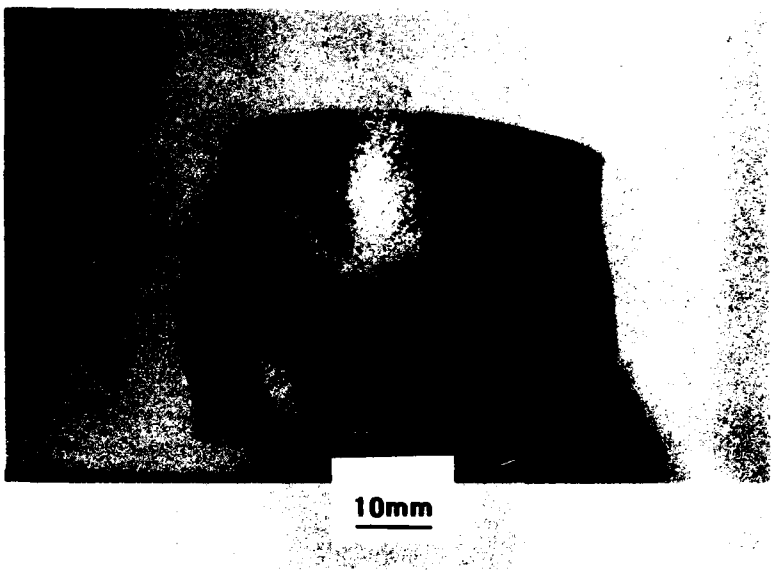

Figure 4c. External shear crack, Alloy 14.

Figure 4d. External shear crack, Alloy 4.

Figure 4e. External shear crack, Alloy 7.

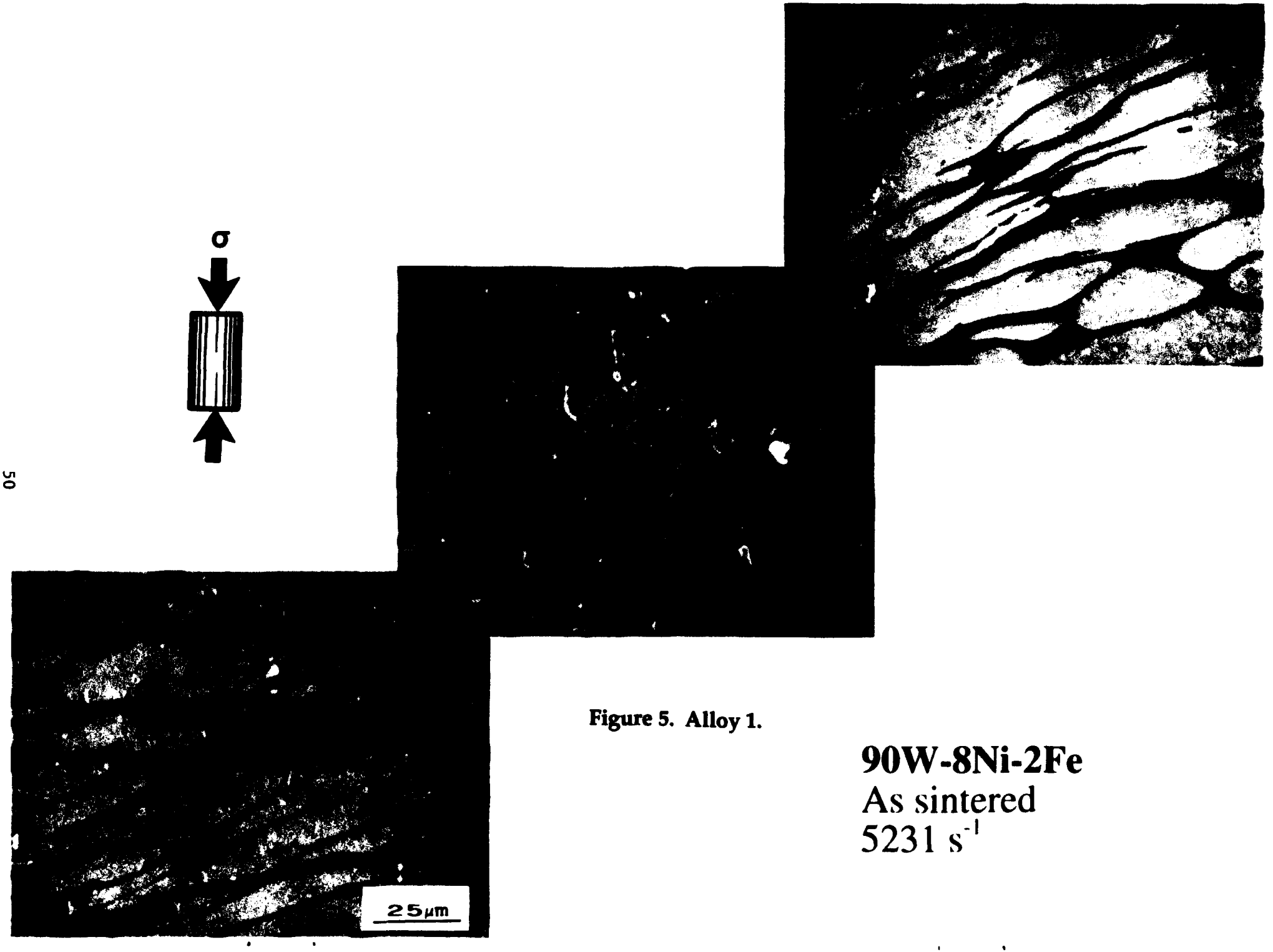

Figure 5. Alloy 1.

90W-8Ni-2Fe
As sintered
5231 s^{-1}

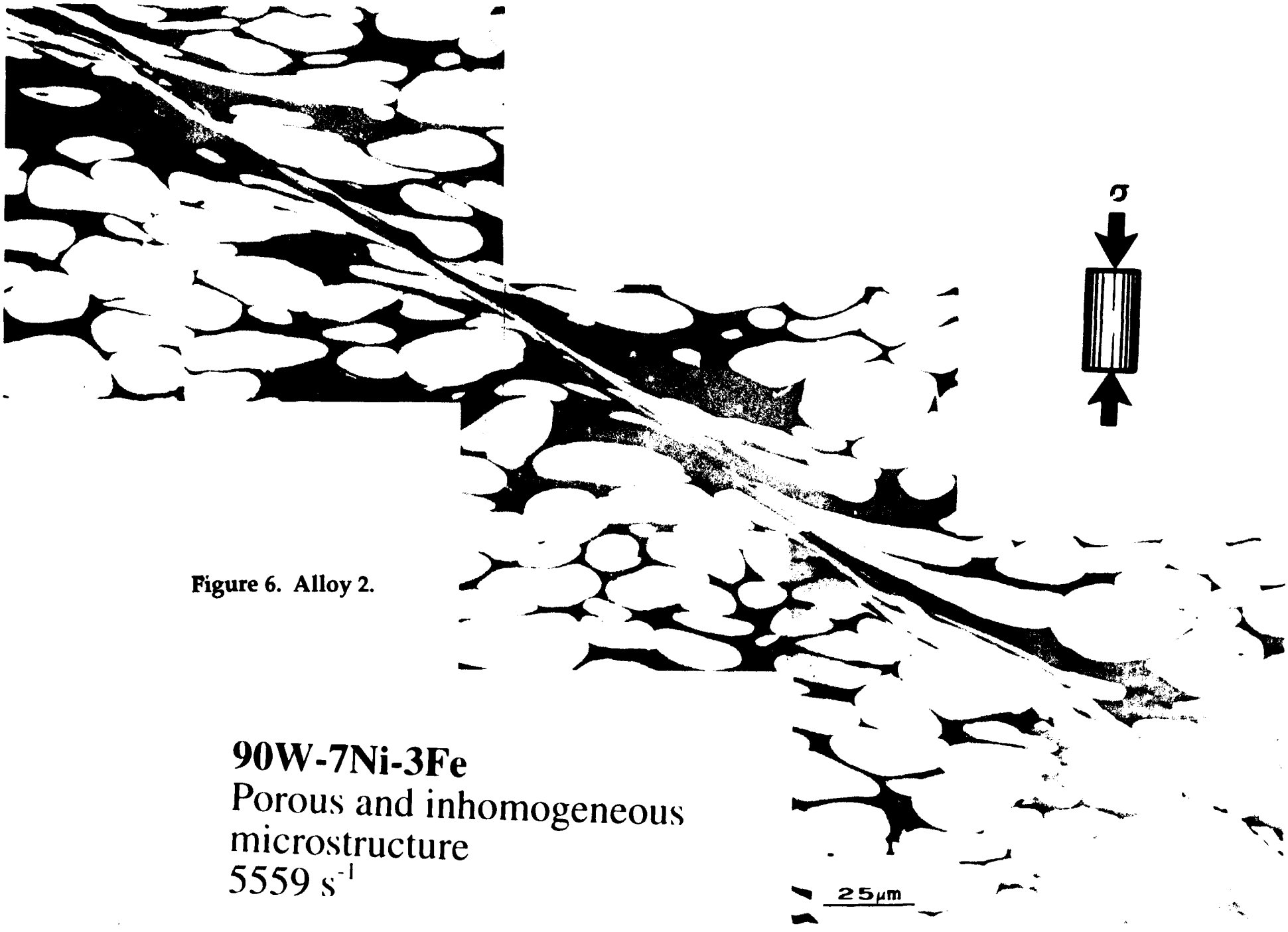

Figure 6. Alloy 2.

90W-7Ni-3Fe
Porous and inhomogeneous microstructure
5559 s^{-1}

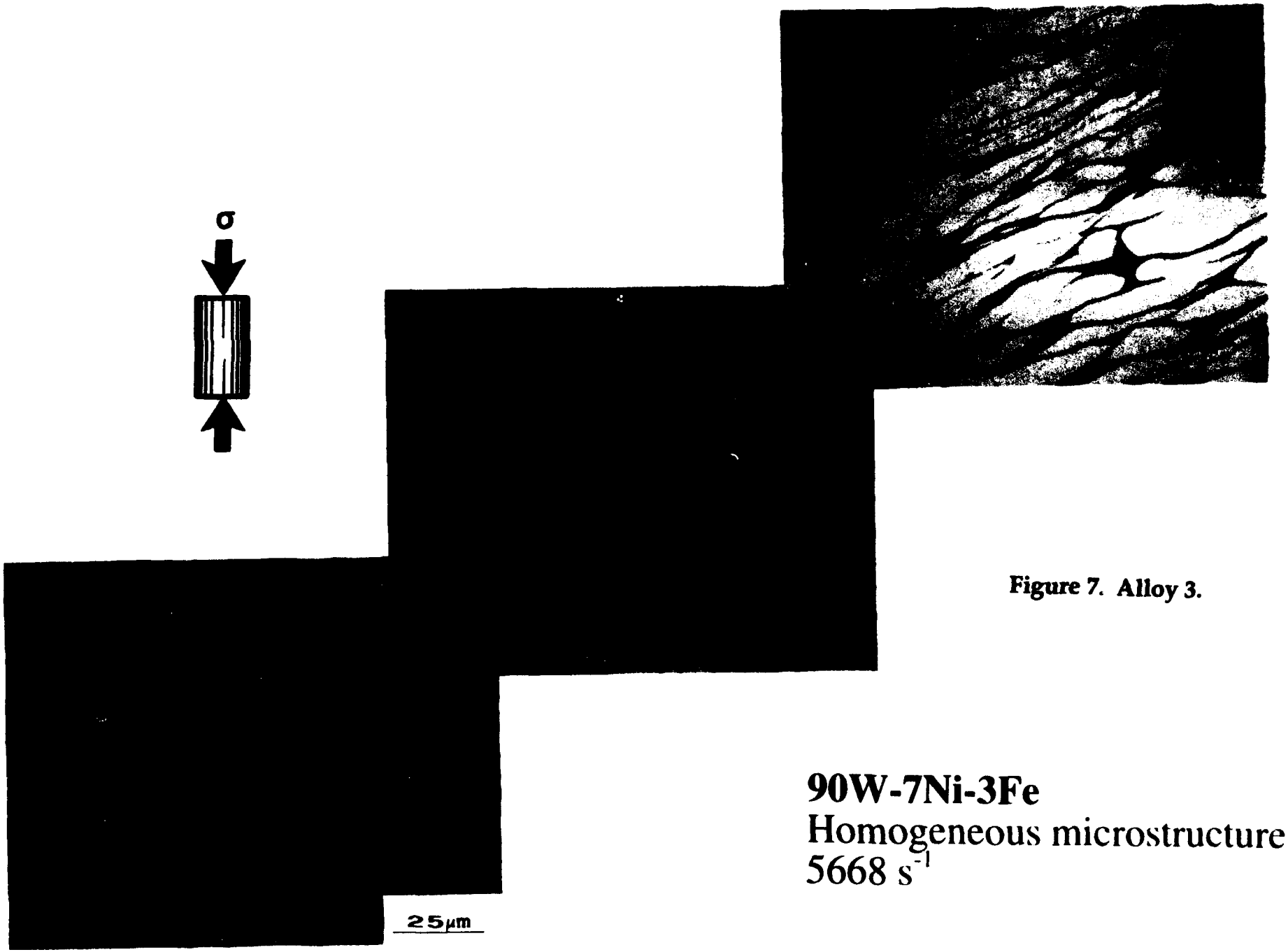

Figure 7. Alloy 3.

90W-7Ni-3Fe
Homogeneous microstructure
5668 s^{-1}

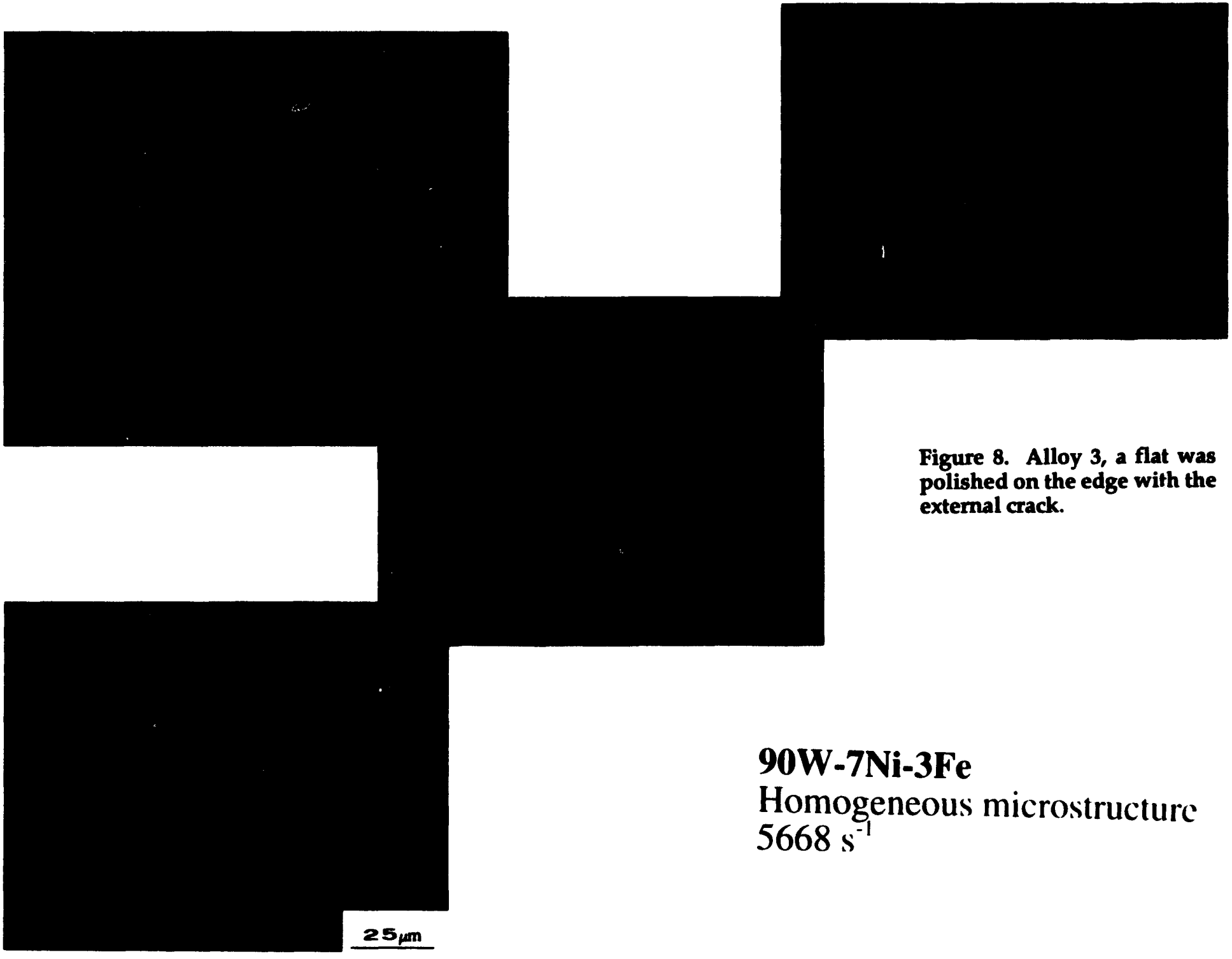

Figure 8. Alloy 3, a flat was polished on the edge with the external crack.

90W-7Ni-3Fe
Homogeneous microstructure
5668 s^{-1}

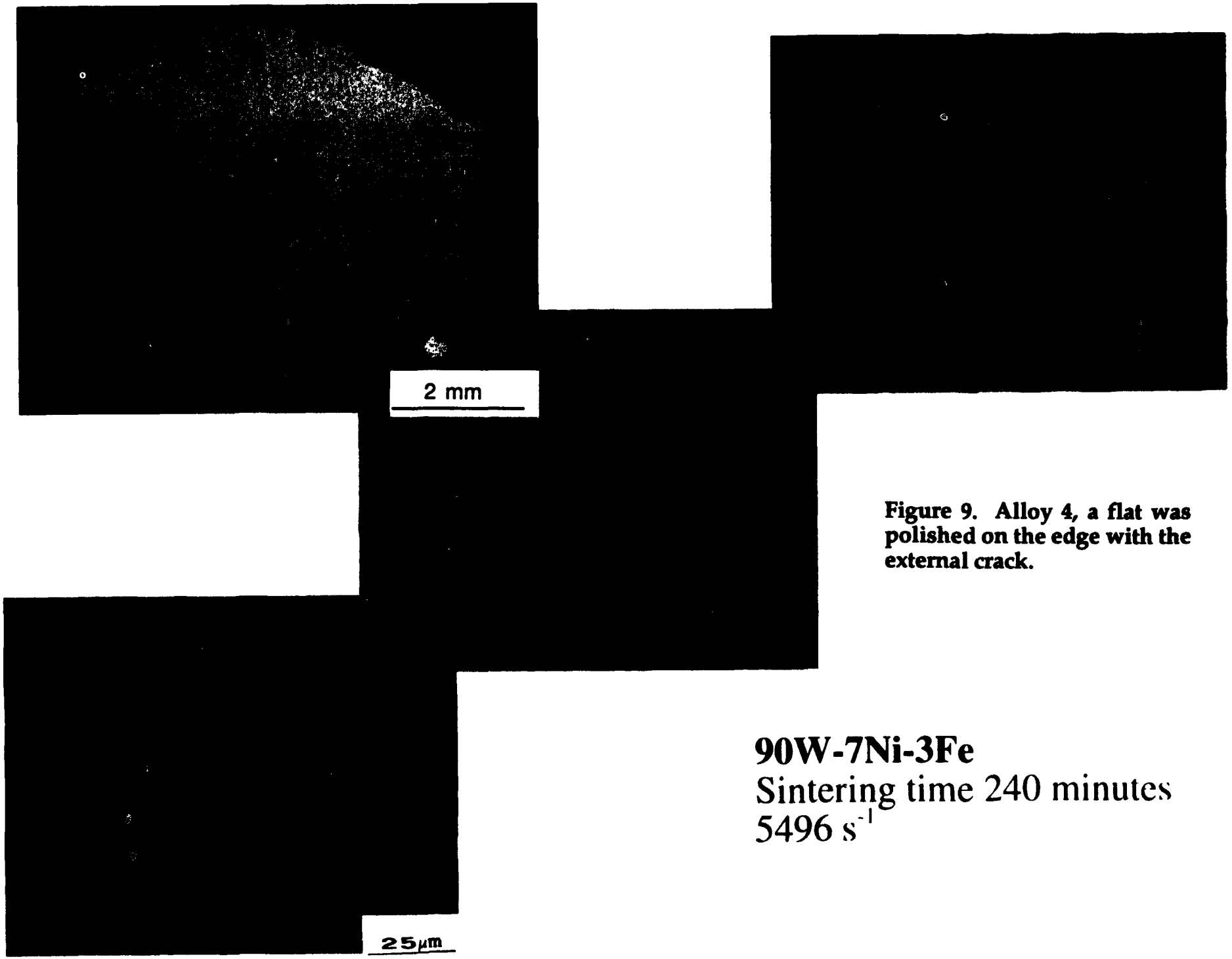

Figure 9. Alloy 4, a flat was polished on the edge with the external crack.

90W-7Ni-3Fe
Sintering time 240 minutes
5496 s^{-1}

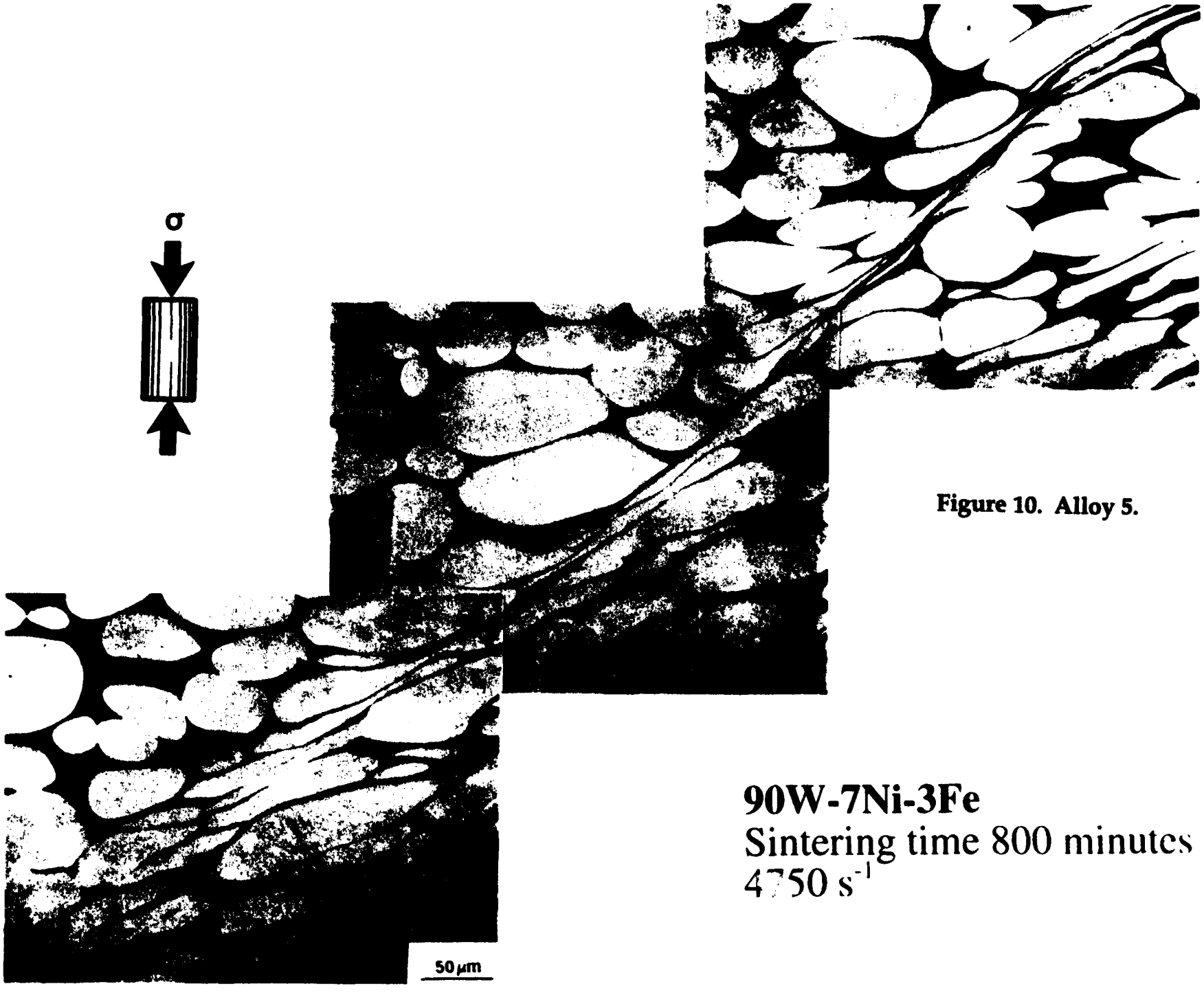

Figure 10. Alloy 5.

90W-7Ni-3Fe
Sintering time 800 minutes
4750 s^{-1}

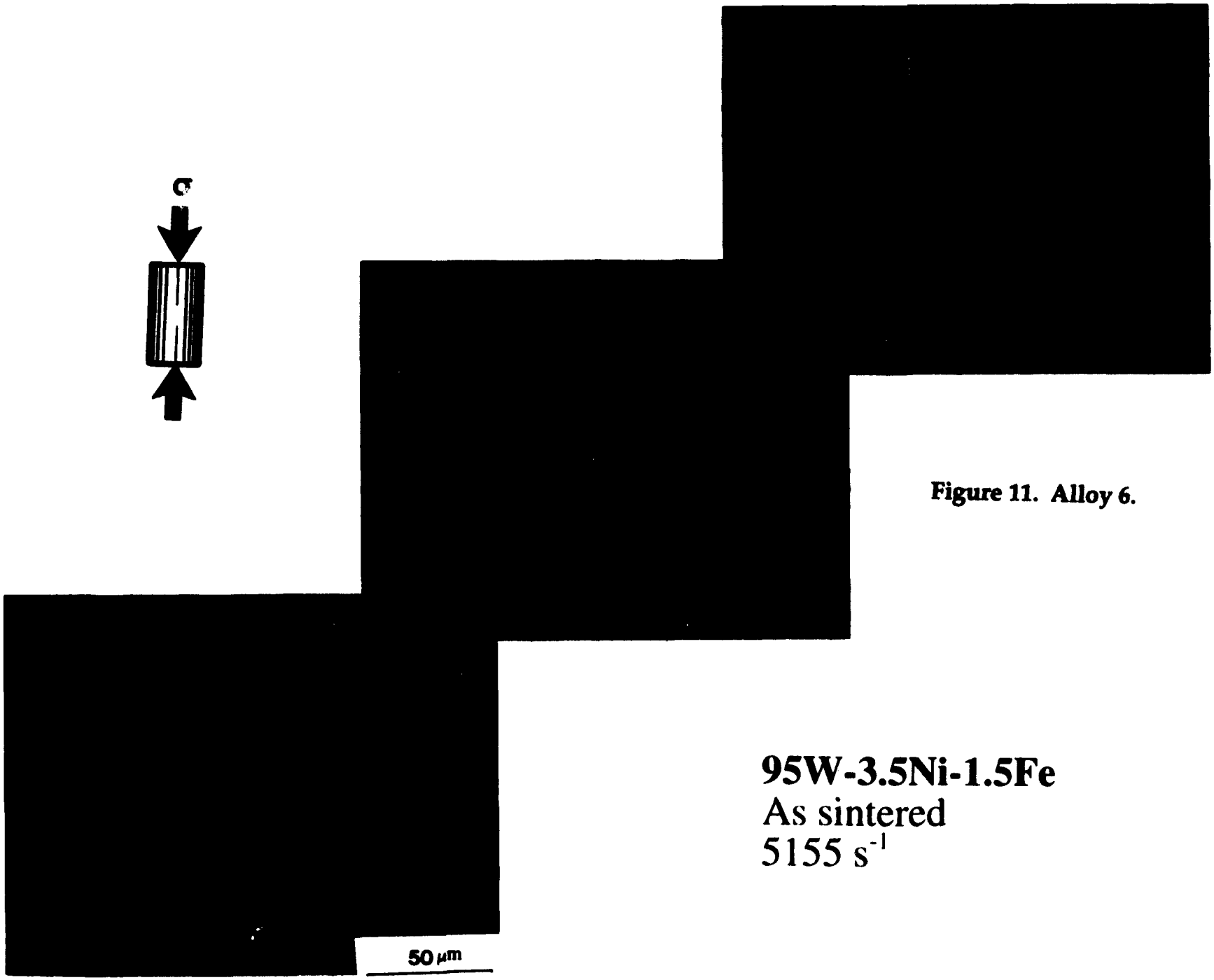

Figure 11. Alloy 6.

95W-3.5Ni-1.5Fe
As sintered
5155 s^{-1}

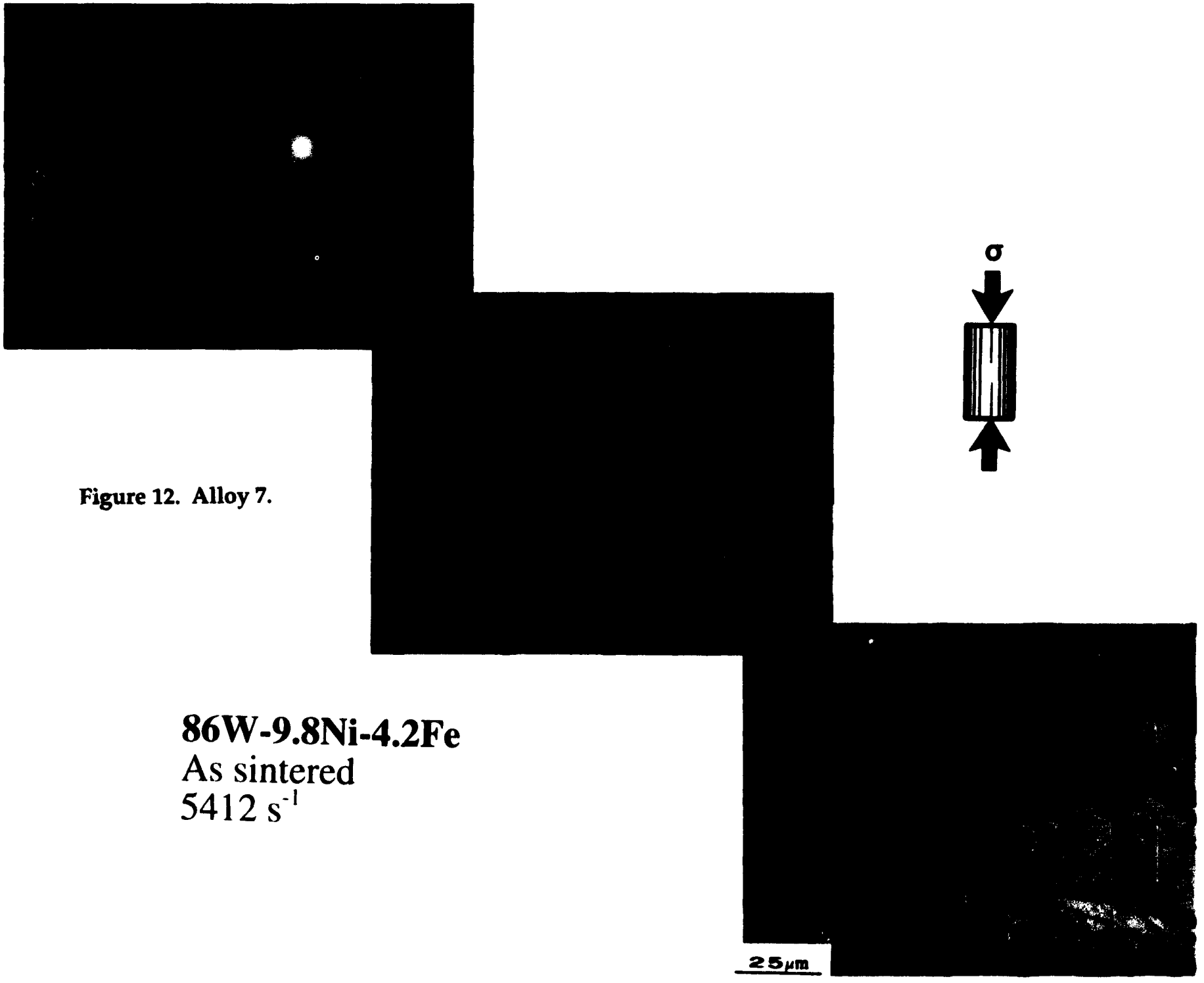

Figure 12. Alloy 7.

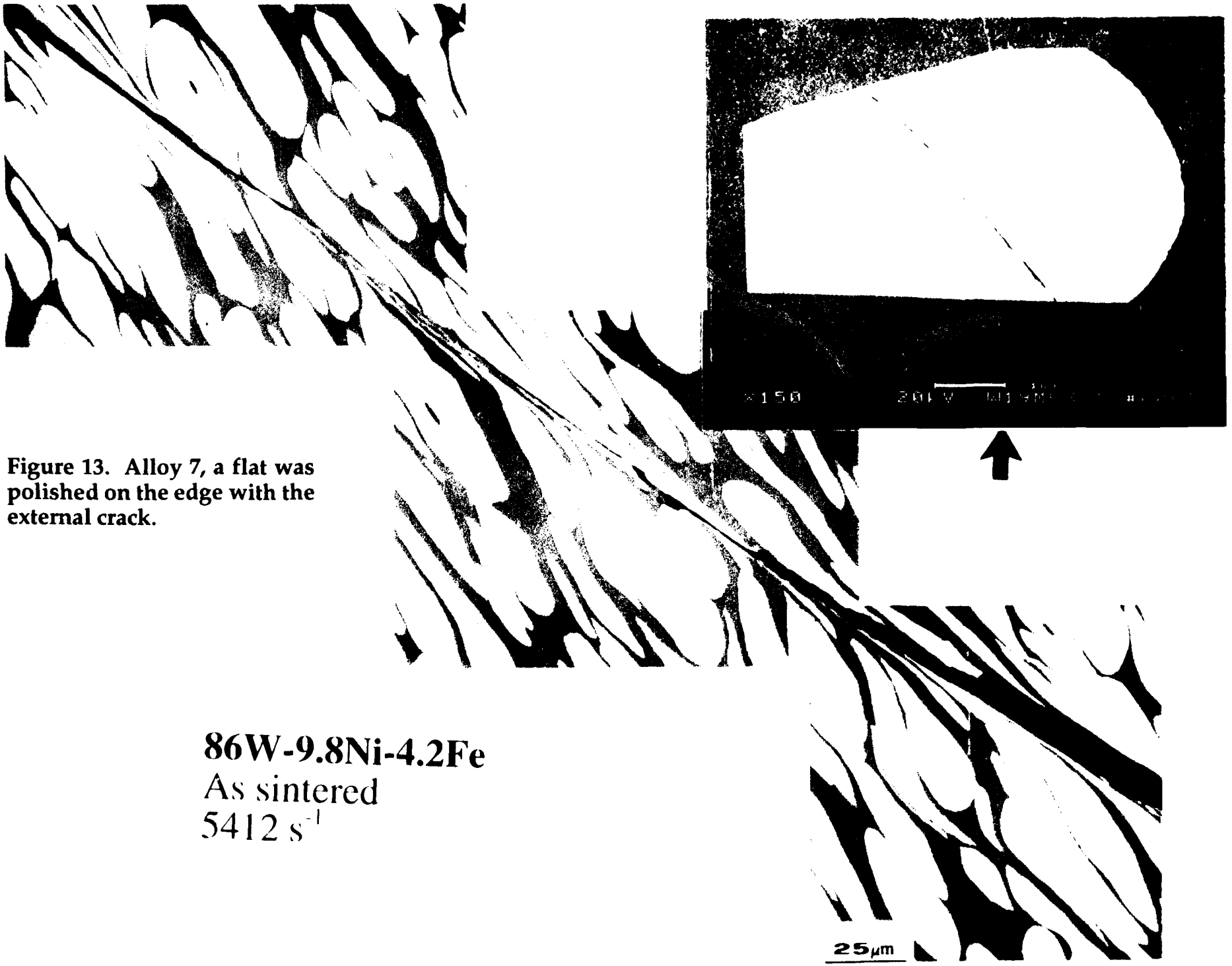

Figure 13. Alloy 7, a flat was polished on the edge with the external crack.

86W-9.8Ni-4.2Fe
As sintered
5412 s^{-1}

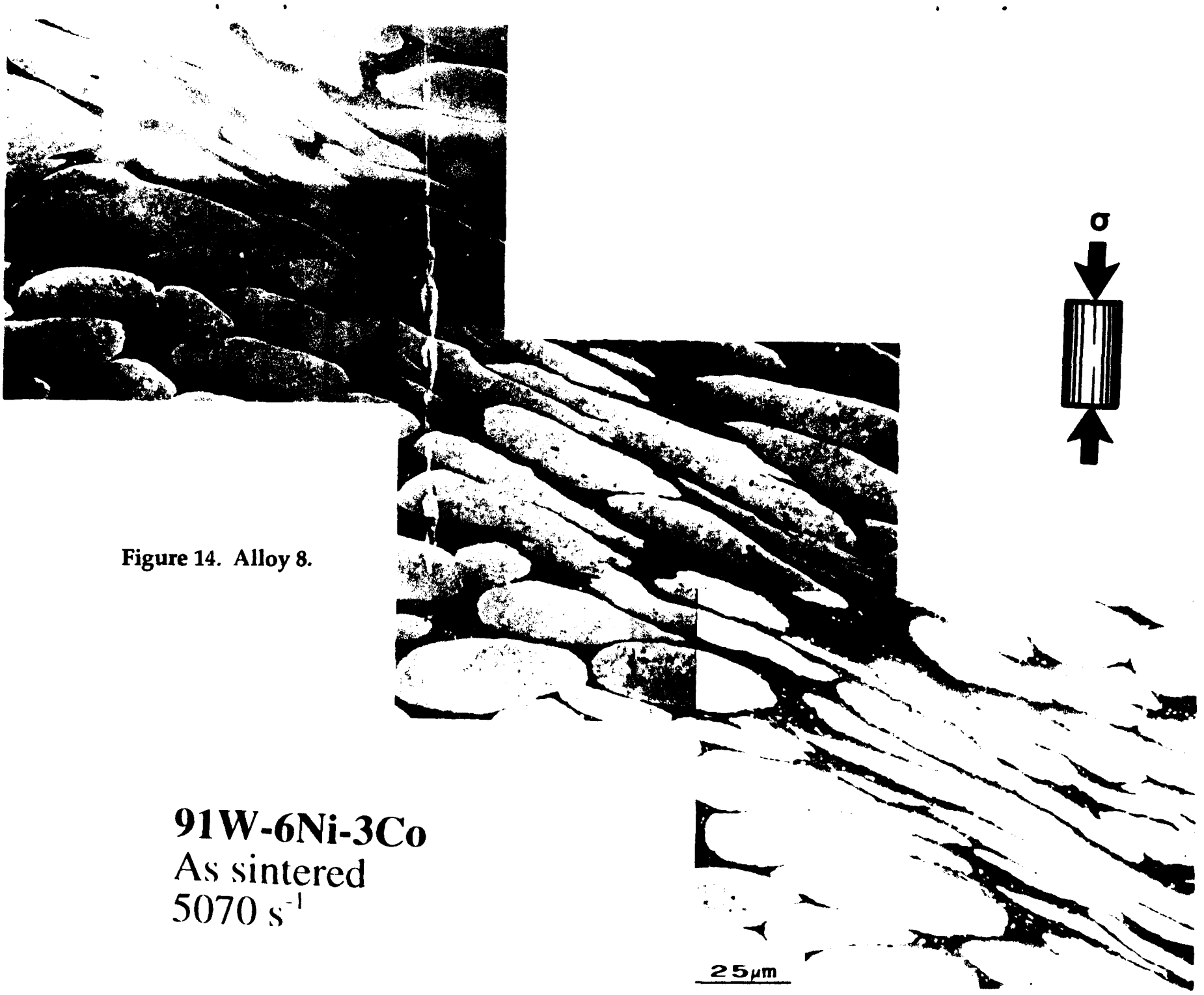

Figure 14. Alloy 8.

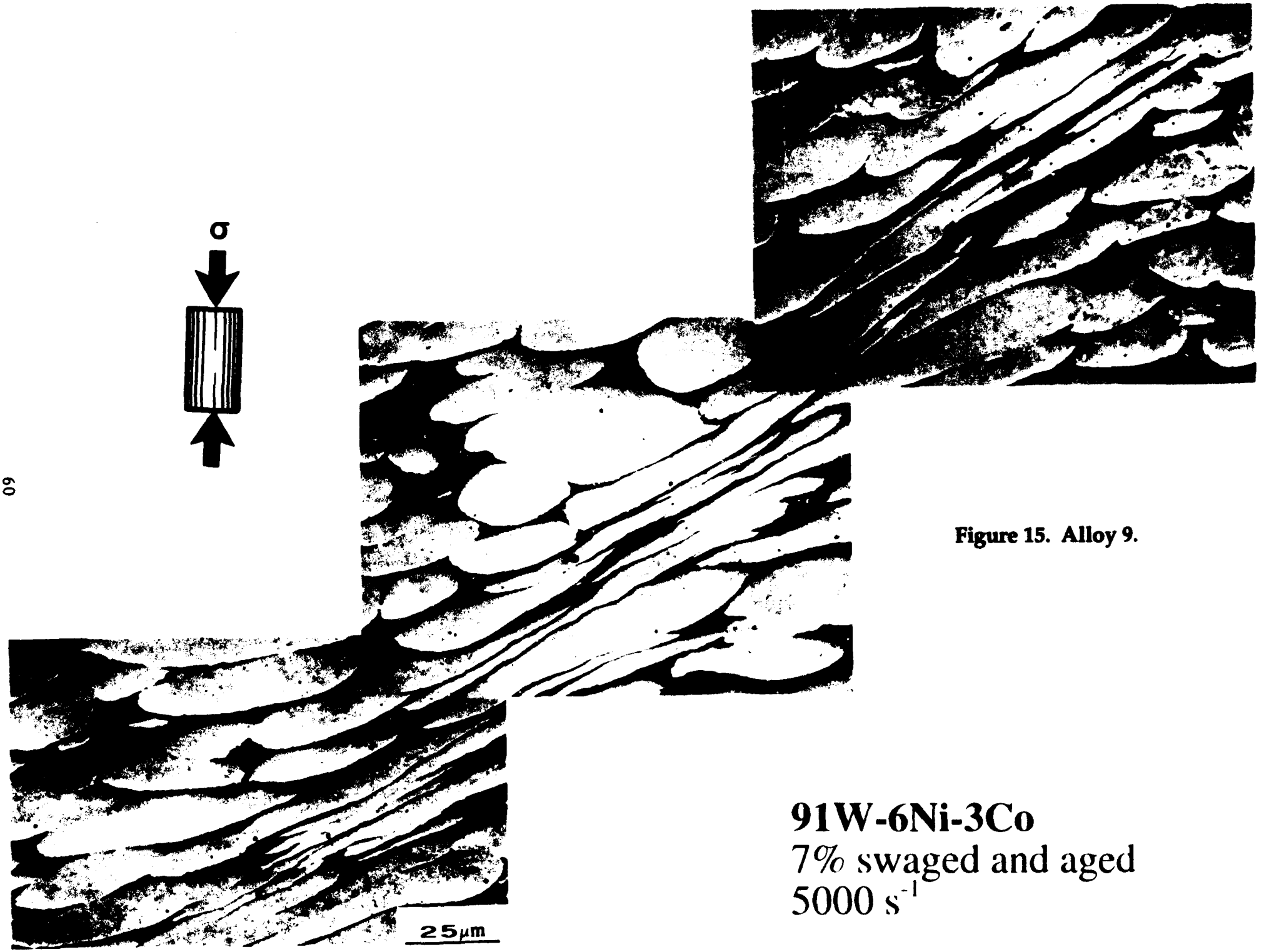

Figure 15. Alloy 9.

91W-6Ni-3Co
7% swaged and aged
5000 s^{-1}

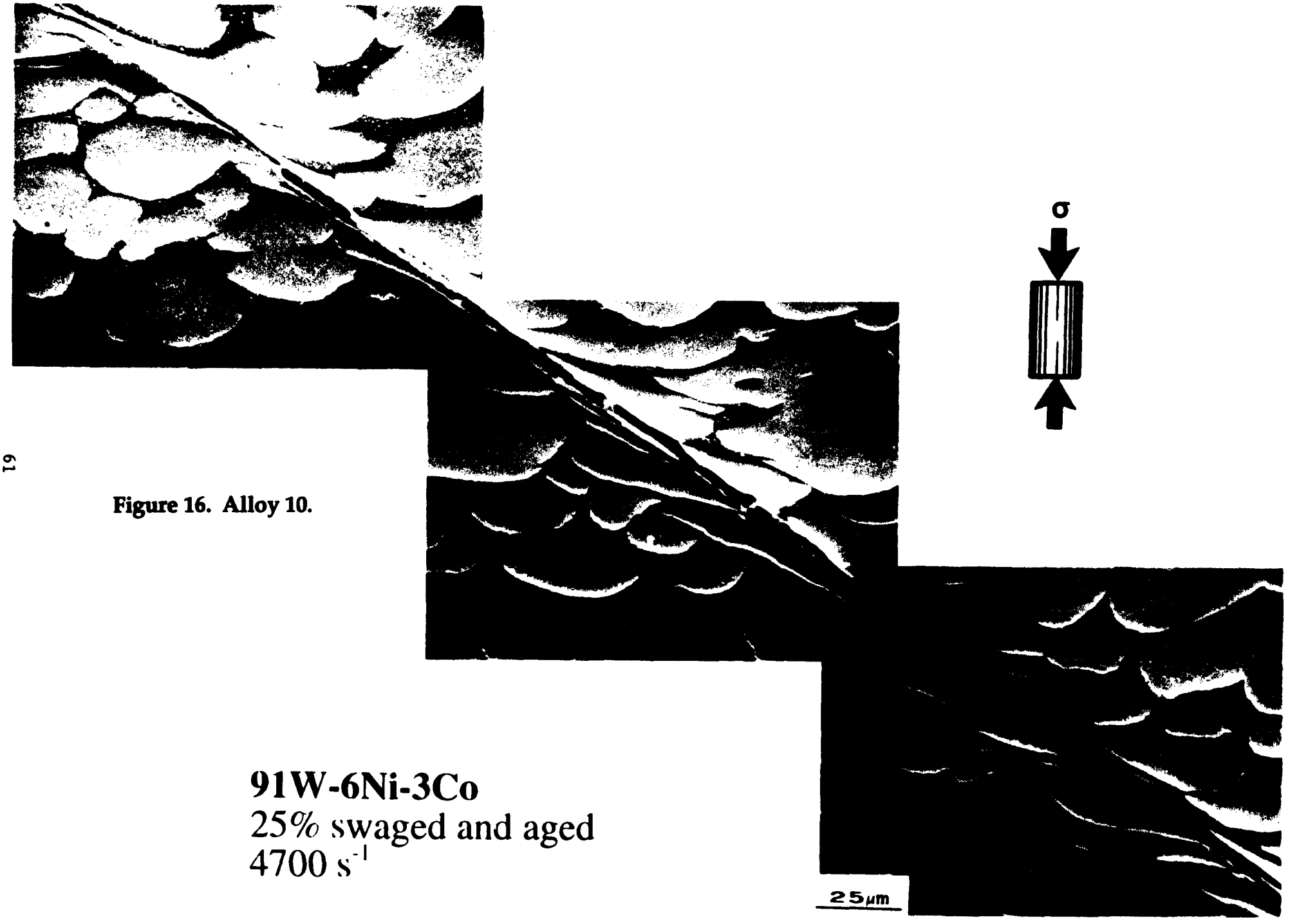

Figure 16. Alloy 10.

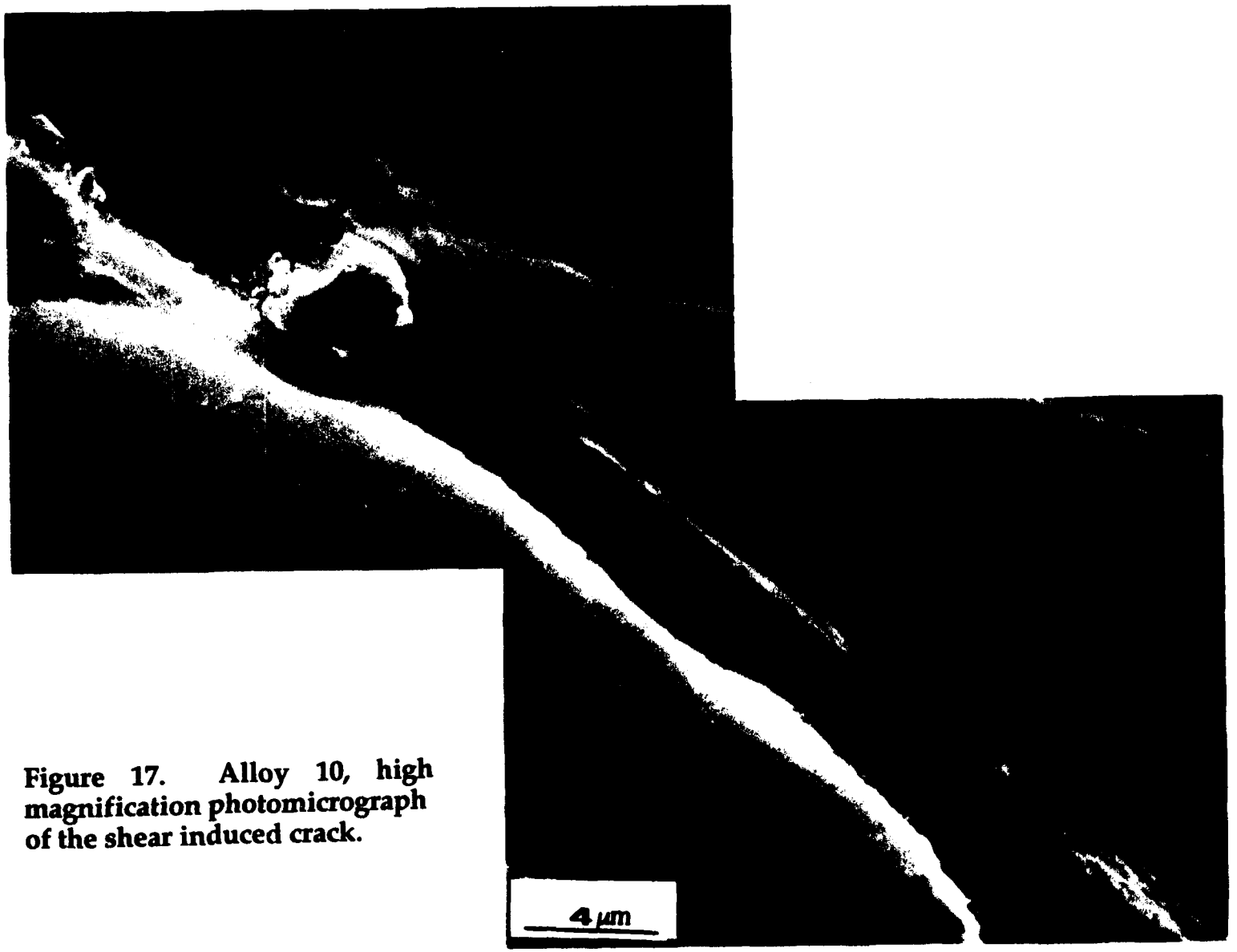

Figure 17. Alloy 10, high magnification photomicrograph of the shear induced crack.

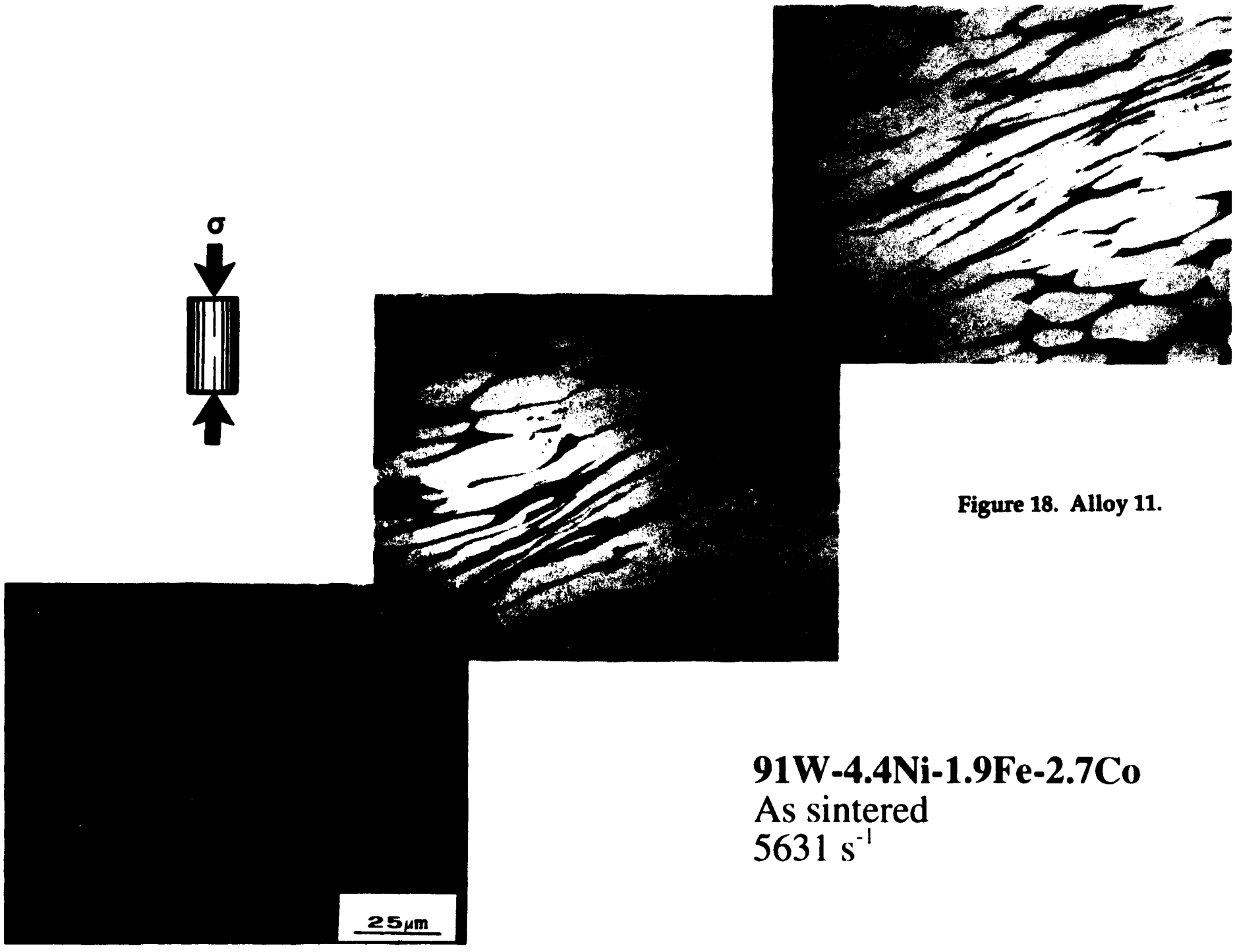

Figure 18. Alloy 11.

91W-4.4Ni-1.9Fe-2.7Co
As sintered
5631 s^{-1}

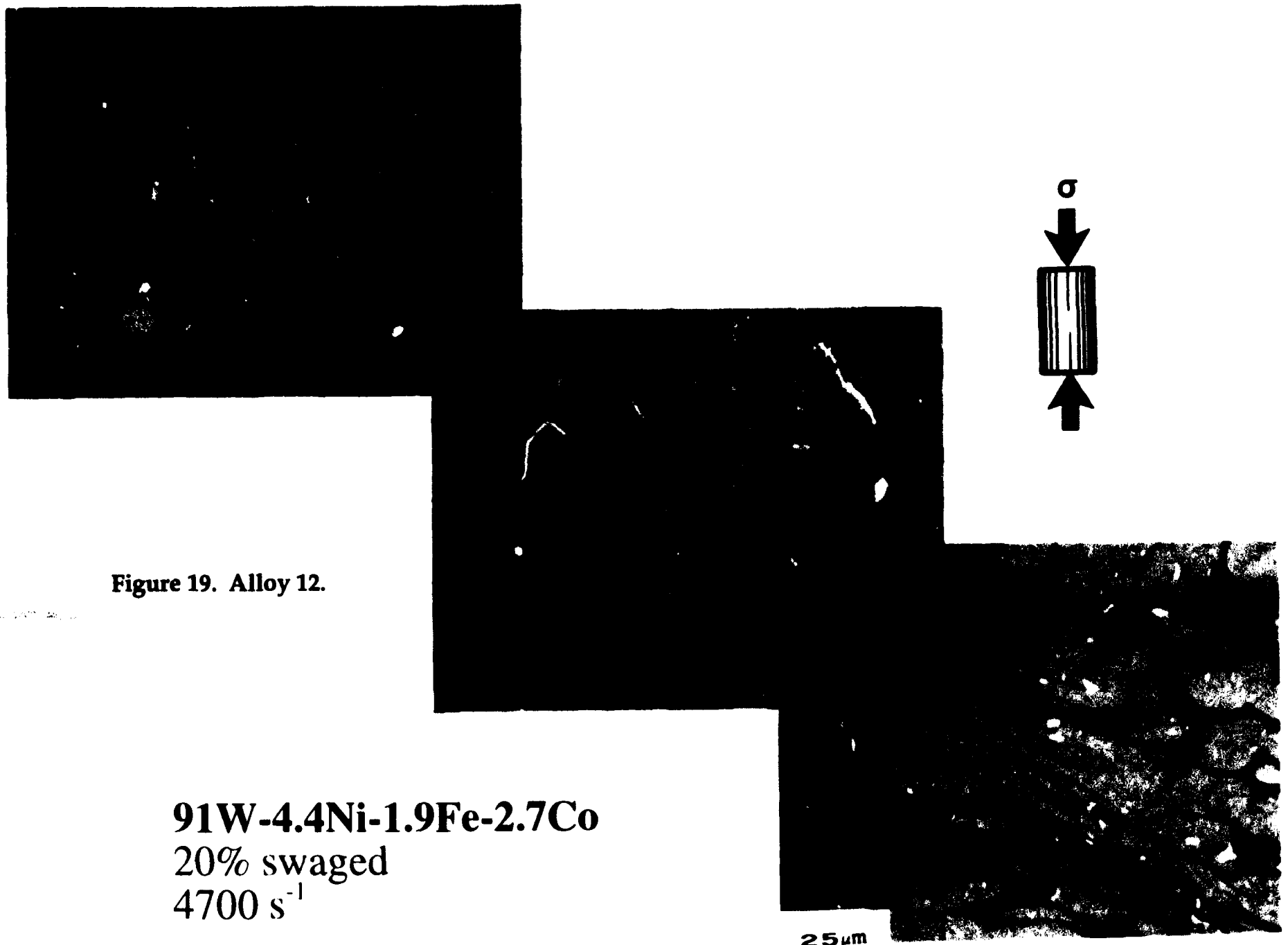

Figure 19. Alloy 12.

91W-4.4Ni-1.9Fe-2.7Co
20% swaged
4700 s^{-1}

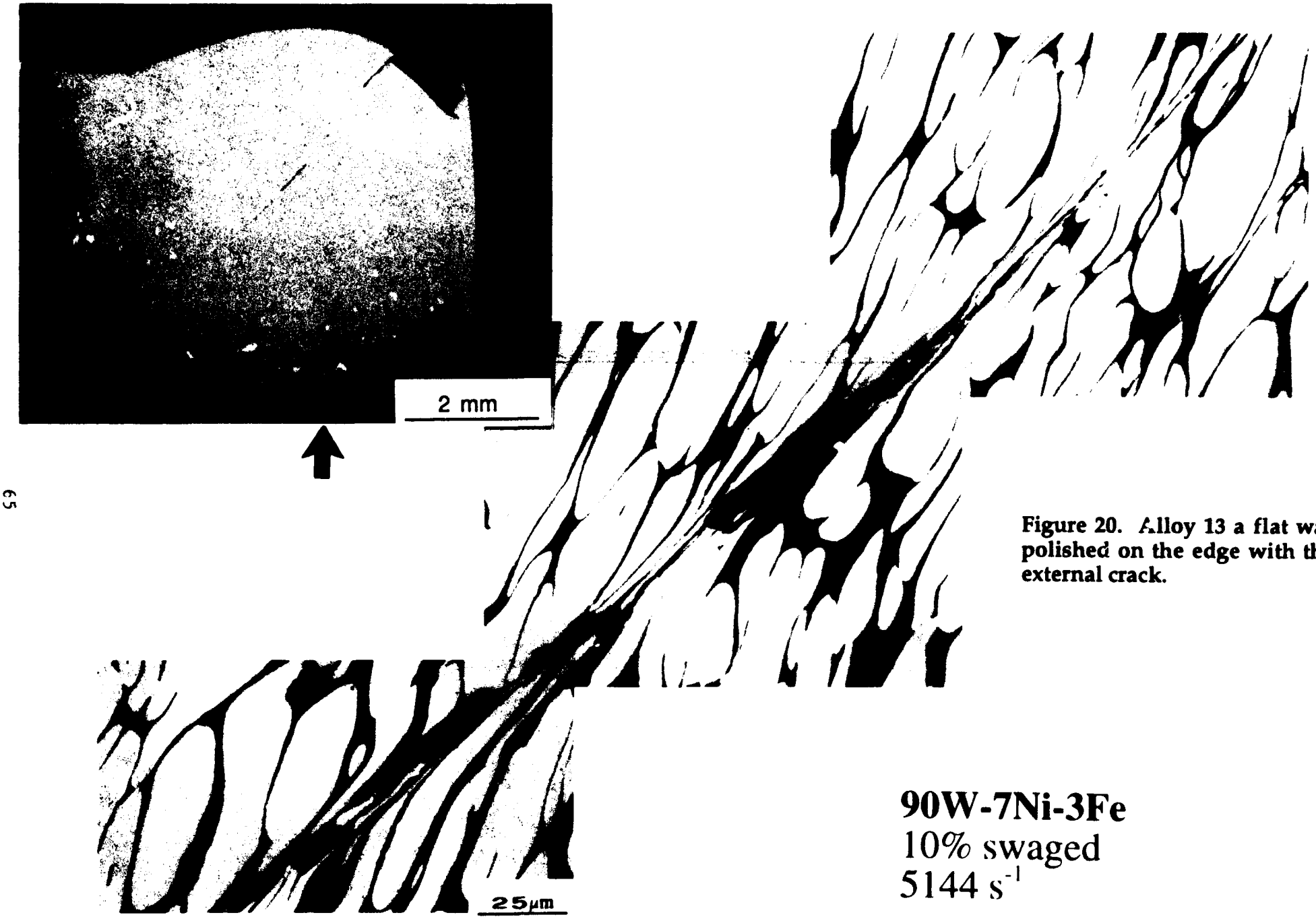

Figure 20. Alloy 13 a flat was polished on the edge with the external crack.

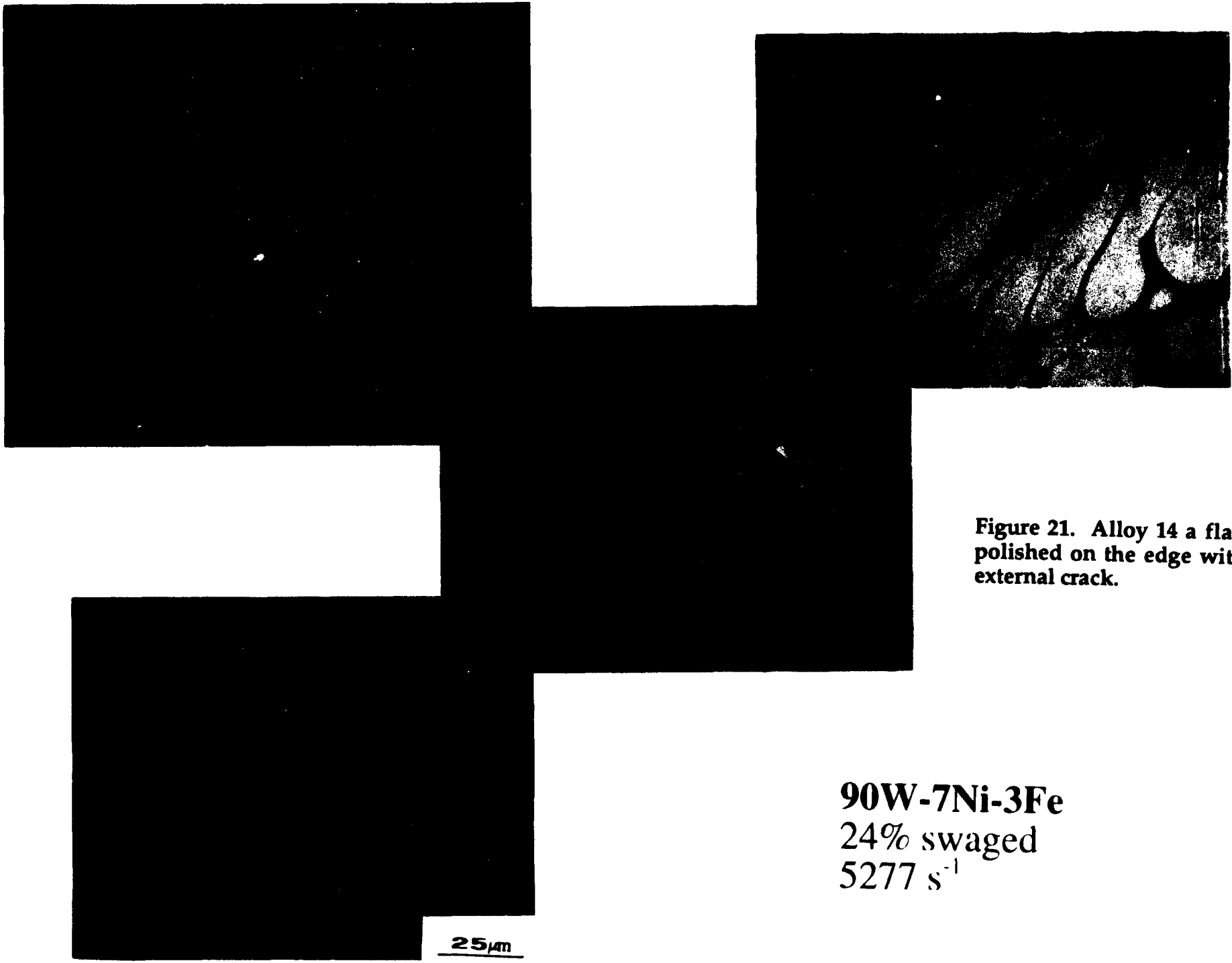

Figure 21. Alloy 14 a flat was polished on the edge with the external crack.

90W-7Ni-3Fe
24% swaged
5277 s^{-1}

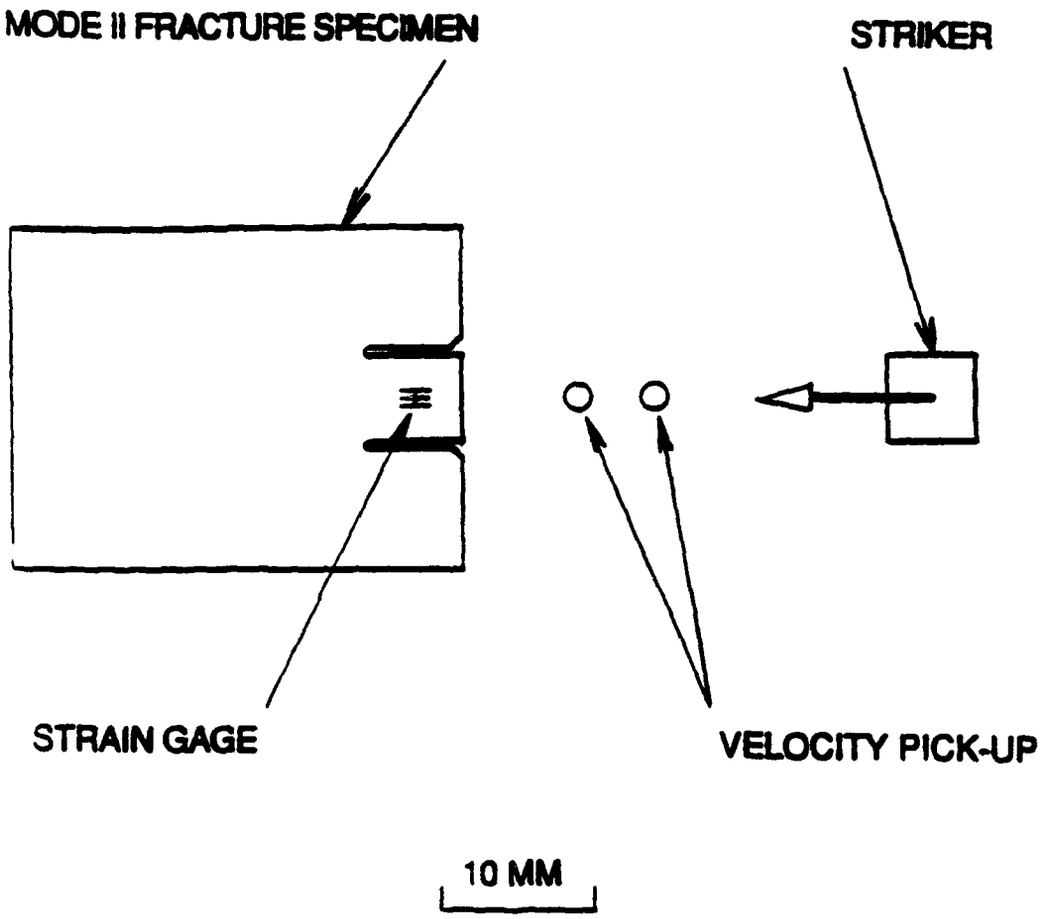

Figure 22. A schematic of the proposed Mode II test.

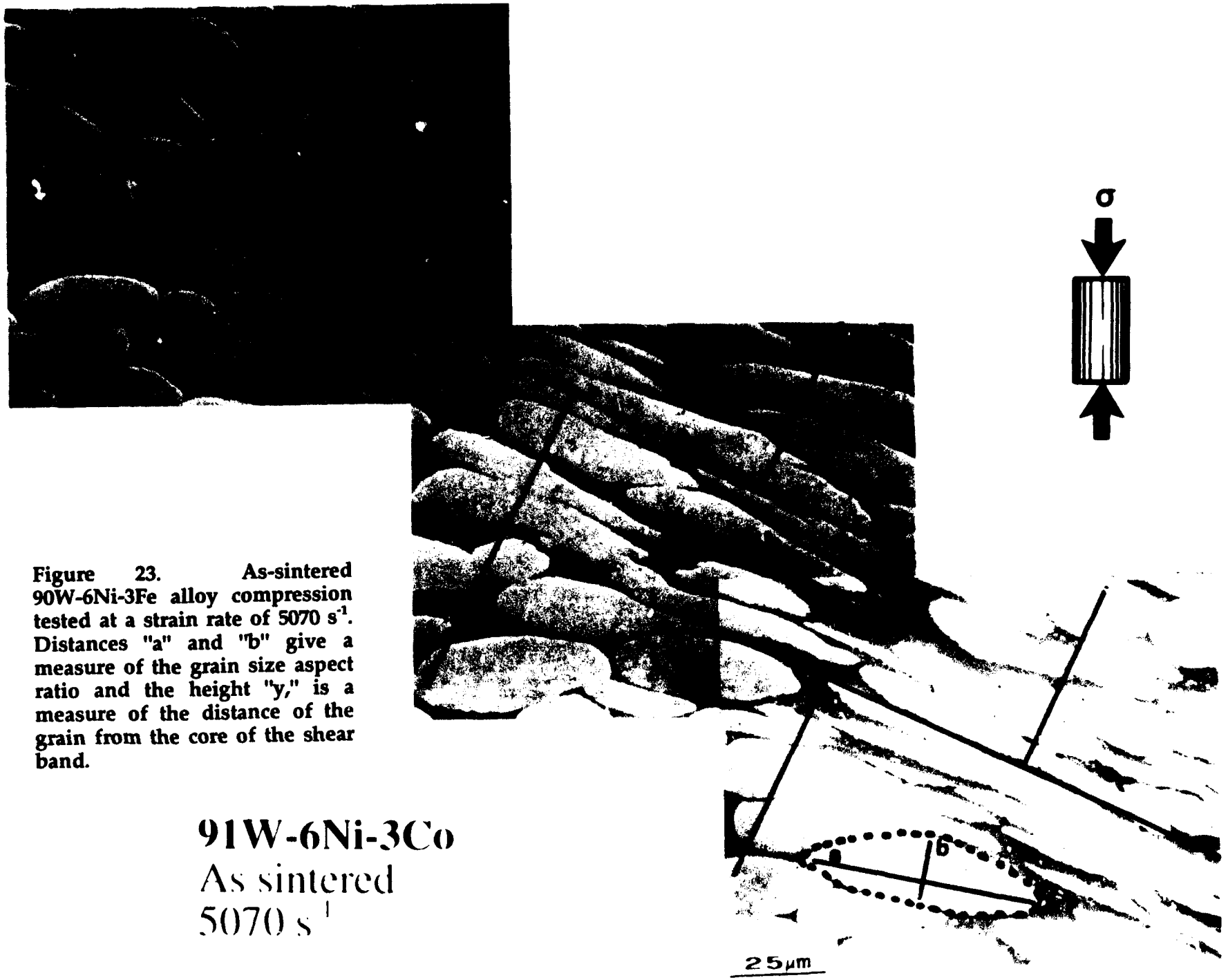

Figure 23. As-sintered 90W-6Ni-3Fe alloy compression tested at a strain rate of 5070 s^{-1}. Distances "a" and "b" give a measure of the grain size aspect ratio and the height "y," is a measure of the distance of the grain from the core of the shear band.

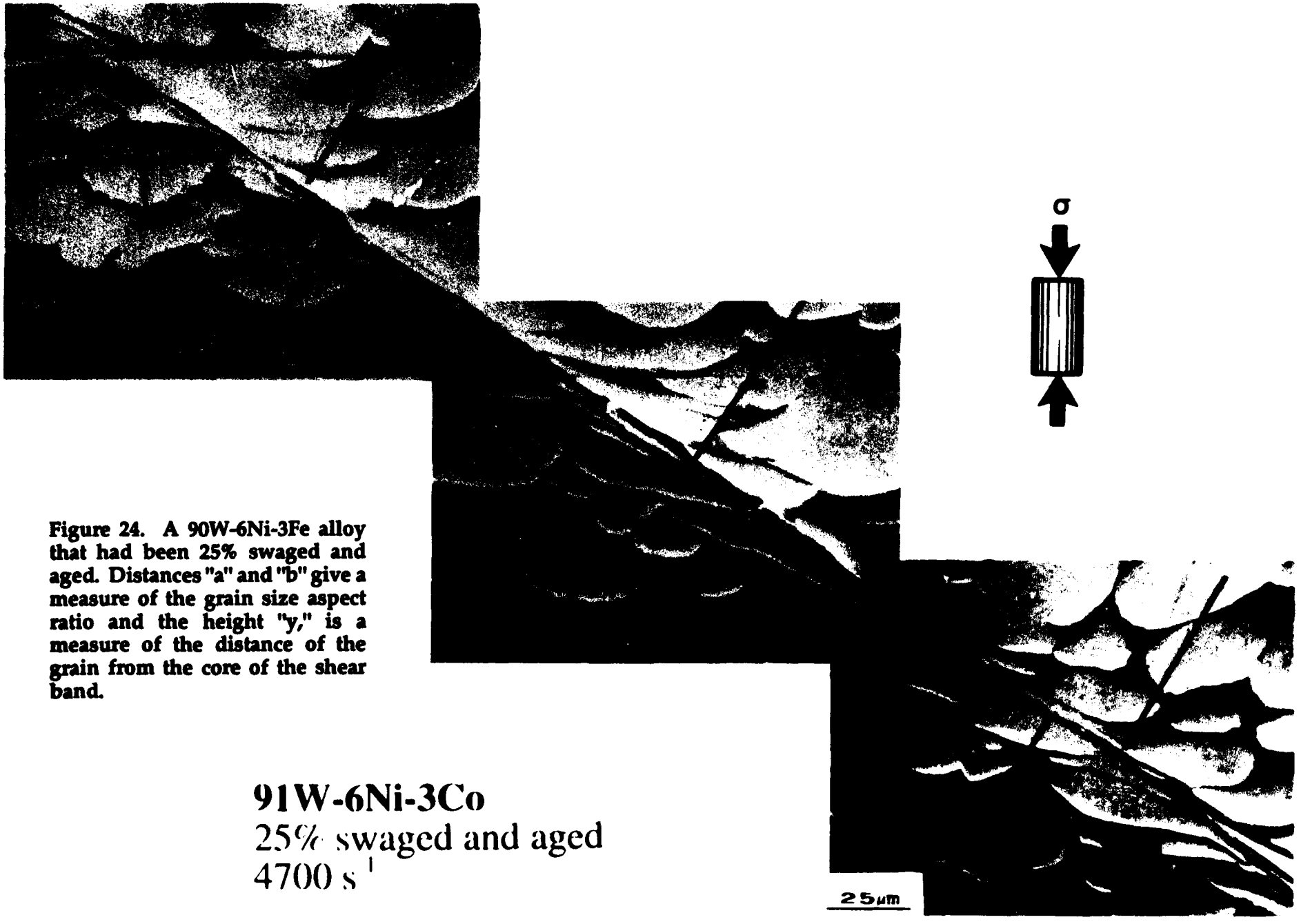

Figure 24. A 90W-6Ni-3Fe alloy that had been 25% swaged and aged. Distances "a" and "b" give a measure of the grain size aspect ratio and the height "y," is a measure of the distance of the grain from the core of the shear band.

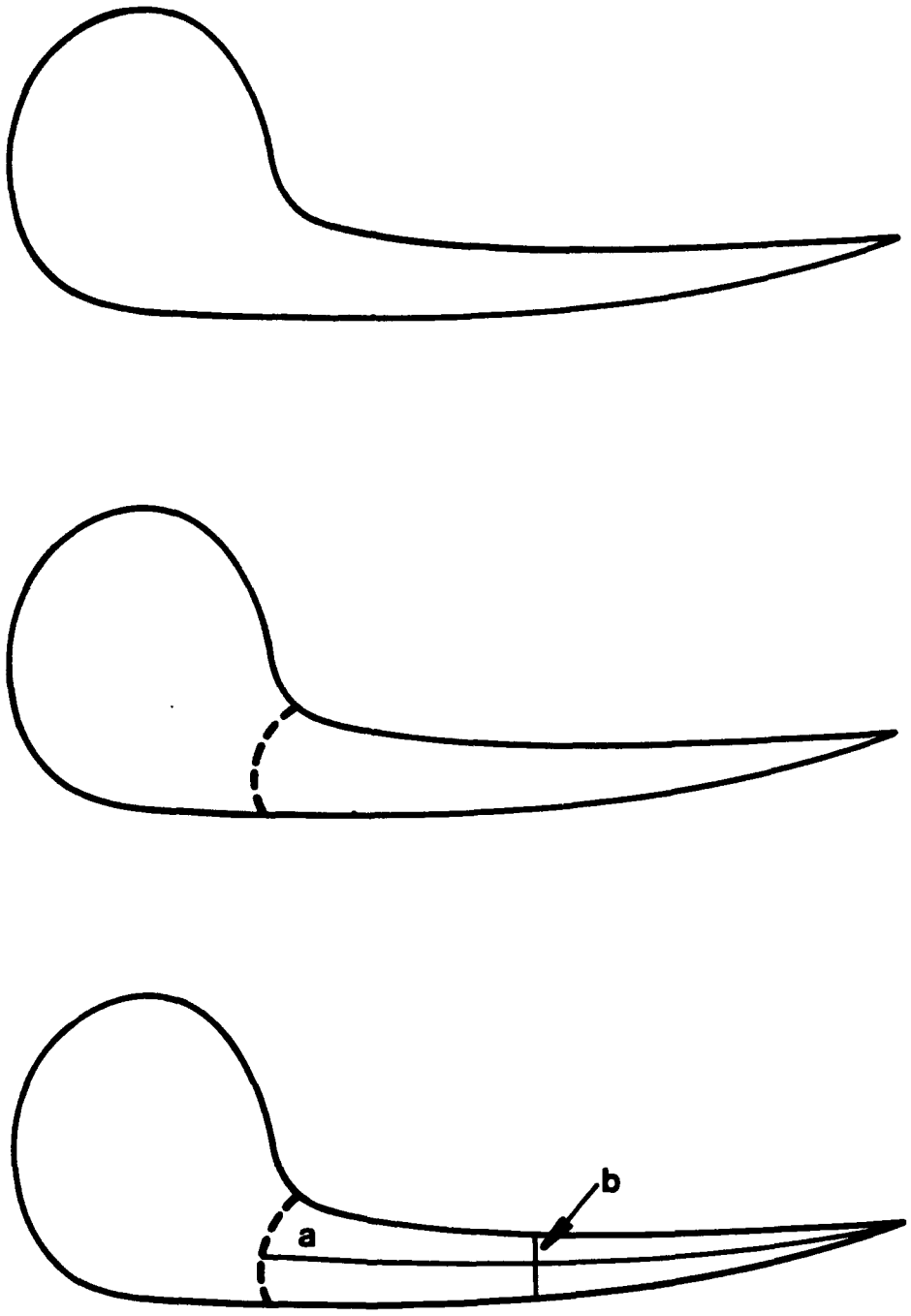

Figure 25. **A schematic view of a tungsten grain that is adjacent to the core of a localized shear band. This figure shows the measurements "a" and "b" that are used to measure the aspect ratio of the tungsten grains.**

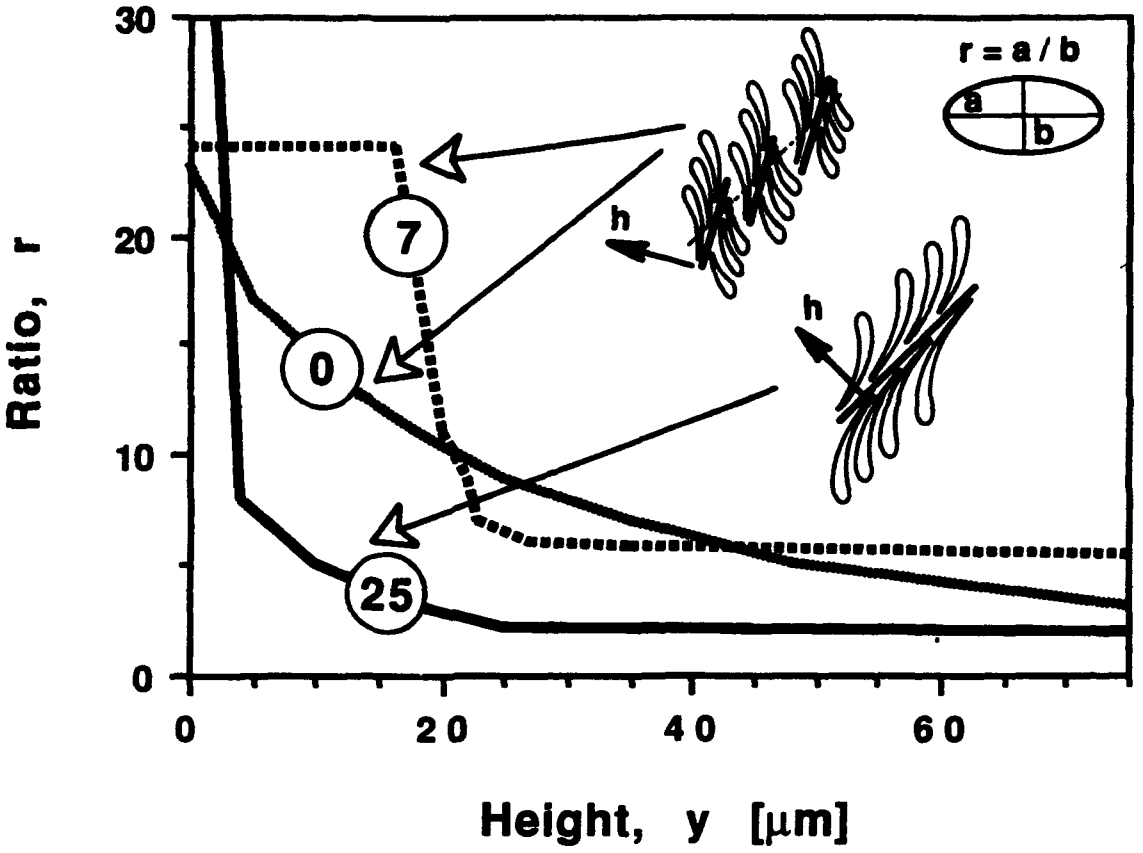

Figure 26. **Variation in the envelope of maximum tungsten grain size aspect ratio with distance from the core of the shear band for Alloys 8, 9, and 10 (marked in the figure as 0, 7, and 25, respectively).**

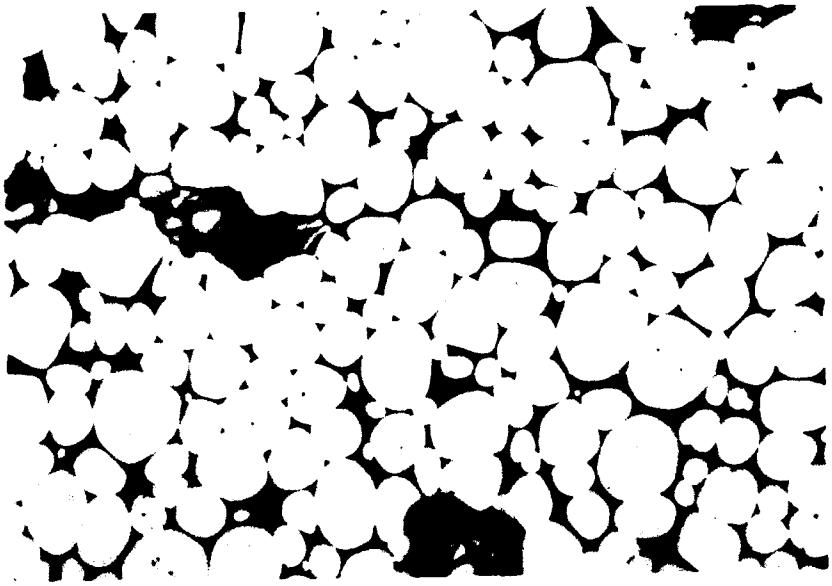

a) Top Section

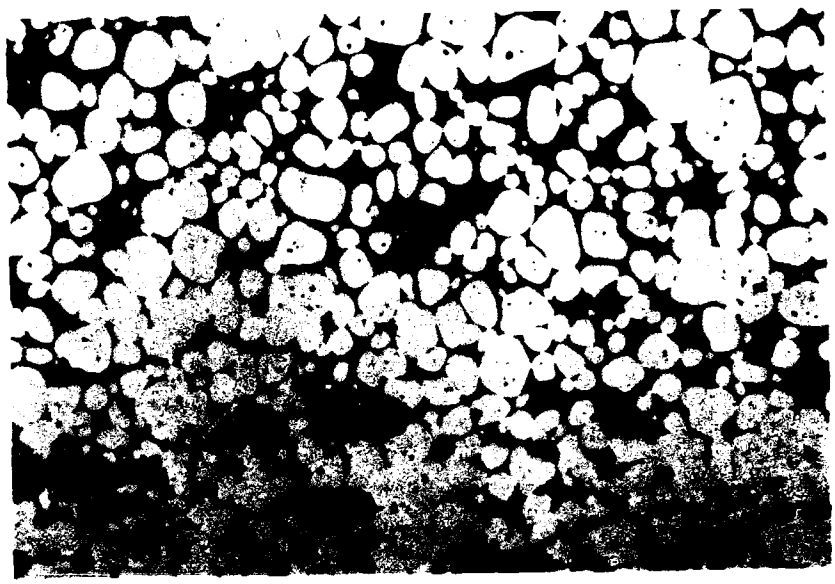

b) Transition Zone

c) Bottom Section

Figure 27. Photomicrographs of three regions of a sample of tungsten heavy alloy doped with alumina.

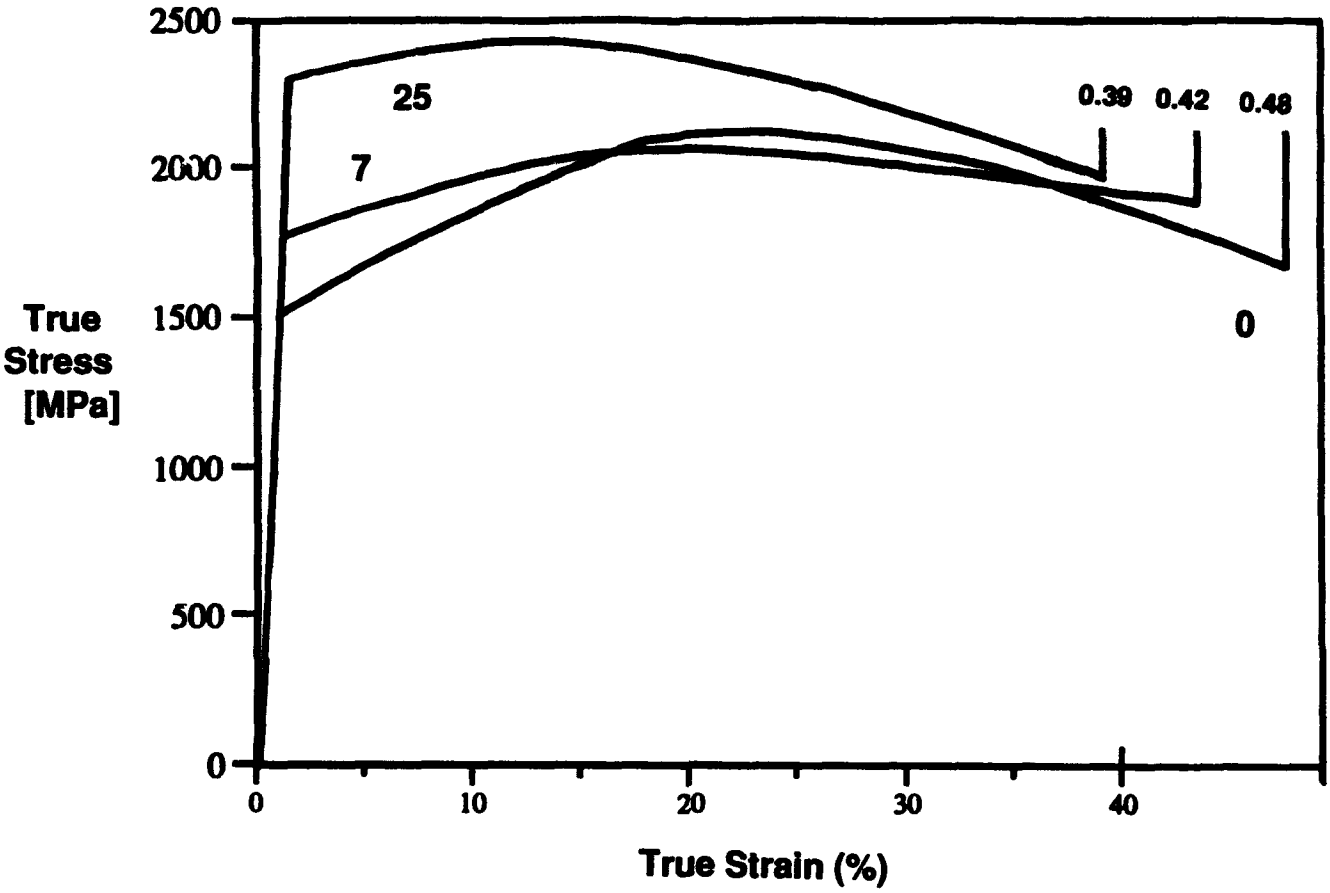

Figure 28. The compression stress-strain curves obtained during high strain rate deformation of Alloy 8, Alloy 9, and Alloy 10.

Distribution List

1 Office of the Secretary of Defense for Research and Engineering, The Pentagon, Washington, D.C. 20301

Director, U.S. Army Research Laboratory, 2800 Powder Mill Road, Adelphi, MD 20783-1197
1 ATTN: AMSRL-OP-CI-AD, Technical Publishing Branch
1 Dr. Alan Goldman
1 AMSRL-OP-CI-AD, Records Management Administrator

Commander, Defense Technical Information Center, Cameron Station, Building 5, 5010 Duke Street, Alexandria, VA 22304-6145
2 DTIC-FDAC

1 MIAC/CINDAS, Purdue University, 2595 Yeager Road, West Lafayette, IN 47905

Commander, Army Research Office, P.O. Box 12211, Research Triangle Park, NC
27709-2211
1 ATTN: Information Processing Office
1 Dr. Andrew Crowson
Dr. Edward Chen

Commander U.S. Army Materiel Command (AMC), 5001 Eisenhower Avenue, Alexandria, VA 22333
1 ATTN: AMCSCI

Commander, U.S. Army Materiel Systems Analysis Activity, Aberdeen Proving Ground, MD 21005
1 ATTN: AMXSY-MP, Director

Commander, U.S. Army Missile Command, Redstone Arsenal, AL 35809
1 ATTN: AMSMI-RD-CS-R/Doc

Commander, U.S. Army Armament Research Development and Engineering Center, Dover, NJ 07801
1 ATTN: Technical Library
1 Mr. D. Kapoor
1 Dr. S. Cytron

Commander, U.S. Army Tank-Automotive Command, Warren, MI 48397-5000
2 ATTN: AMSTA-TSL Technical Library

Commander, U.S. Army Foreign Science and Technology Center, 220 7th Street, N.E., Charlottesville, VA 22901
3 ATTN: AIFRTC, Applied Technologies Branch, Gerald Schlesinger

Naval Research Laboratory, Washington, D.C. 20375
1 ATTN: Code 2627
1 Dr. Virgil Provenzano

Chief of Naval Research, Arlington, VA 22217
1 ATTN: Code 471

Naval Surface Weapons Center, Dahlgren Laboratory, Dahlgren, VA 22448
1 ATTN: Code G-32, Ammunition Branch, Mr. Brian Sabourin

Commander, Rock Island Arsenal, Rock Island, IL 61299-6000
1 ATTN: SMCRI-SEM-T

Battelle Columbus Laboratories, Battelle Memorial Institute, 505 King Avenue, Columbus, OH 43201
1 ATTN: Mr. Henry Cialone
1 Dr. Alan Clauer

Battelle Pacific Northwest Laboratories, P.O. Box 999, Richland, WA 99352
1 ATTN: Mr. William Gurwell
1 Dr. Gordon Dudder
1 Mr. Curt Lavender

GTE Sylvania, Inc. Chemical and Metallurgical Division, Hawes Street, Towanda, PA 18848
1 ATTN: Dr. James Mullendore
1 Mr. James Spencer
1 Ms. Susan Doepker

Director, U.S. Army Research Laboratory, Aberdeen Proving Ground, MD 21005
1 ATTN: AMSRL-WT
1 AMSRL-WT-T, Dr. Lee Magness
1 Ms. W.A. Leonard

Teledyne Firth Sterling, 1 Teledyne Place, LaVergne, TN 37086
1 ATTN: Dr. Steven Caldwell

Los Alamos National Laboratory, ATAC, MS F681, P.O. Box 1663, Los Alamos, NM 87545
1 ATTN: Mr. Bill Hogan
1 Mr. Paul Dunn
1 Mr. Bill Baker

Philips Elmet, 1560 Lisbon Road, Lewiston, ME 04240
1 ATTN: Mr. James Anderson

Ultramet, Inc., 12173 Montague Street, Pacoima, CA 91331
1 ATTN: Mr. Brian Williams
1 Dr. Robert Tuffias

Ceracon, Inc., 1101 N. Market Boulevard, Suite 9, Sacramento, CA 95834
1 ATTN: Dr. Ramas Raman
1 Mr. Sundeep Rele

Southwest Research Institute, 6220 Culebra Road, P.O. Drawer 28510, San Antonio, TX 78228-0510
1 ATTN: Dr. James Lankford

Metalworking Technology, Inc., 1450 Scalp Avenue, Johnstown, PA 15904
1 ATTN: Mr. C. Buck Skena
1 Mr. Timothy McCabe

Research Triangle Institute, P.O. Box 12194, Research Triangle Park, NC 27709-2154
1 ATTN: Dr. John B. Posthill

3C Systems, 620 Arglye Road, Wynnewood, PA 19096
1 ATTN: Mr. Murray Kornhauser

Advance Technology Coatings, 300 Blue Smoke Ct. West, Fort Worth, TX 76105

Alliant Techsystems, 7225 Northland Drive, Brooklyn Park, MN 55428
1 ATTN: Dr. Stan Nelson
1 Mr. Mark Jones
1 Mr. Thomas Steigauf

CAMDEC, 3002 Dow Avenue, Suite 110, Tustin, CA 92680

Chamberlain Manufacturing Co., 550 Esther St., P.O. Box 2545, Waterloo, IA
50704
1 ATTN: Mr. Tom Lynch

Defense Technology International, Inc., The Stark House, 22 Concord Street,
Nashua, NH
1 ATTN: Mr. Douglas Ayer

Materials and Electrochemical Research Corporation, 7960 S. Kolb Road, Tucson, AZ 85706
1 ATTN: Dr. James Withers
1 Dr. Sumit Guha

Materials Modification, Inc., 2929-P1 Eskridge Center, Fairfax, VA 22031
1 ATTN: Dr. T.S. Sudarshan

Micro Materials Technology, 120-D Research Drive, Milford, CT 06460
1 ATTN: Dr. Richard Cheney

Nuclear Metals, 2229 Main Street, Concord, MA 01742
1 ATTN: Dr. Willian Nachtrab

Olin Ordnance, 10101 9th Street N., St. Petersburg, FL
1 ATTN: Hugh McElroy

The Pennsylvania State University, Department of Engineering Science and Mechanics, 227 Hammond Building, University Park, PA 16802-1401
1 ATTN: Dr. Randall M. German, Professor, Brush Chair in Materials

Worcester Polytechnic Institute, 100 Institute Road, Worcester, MA, 01609
1 ATTN: Dr. Ronald Biederman
1 Dr. Richard Sisson

Failure Analysis Associates, Inc., 149 Commonwealth Drive, PO Box 3015, Menlo Park, CA 94025
1 ATTN: S.P. Andrew
1 R.D. Caliguri
1 T.K. Parnell
1 L.E. Eiselstein

Amorphous Technologies International, Laguna Hills, CA
1 ATTN: Mr. Dick Harlow

Parmatech Corporation, 2221 Pine View Way, Petaluma, CA 94952
1 ATTN: Dr. Animesh Bose

Stiglich Associates, PO Box 206, Sierra Madre, CA 91025
1 ATTN: Dr. Jack Stiglich

Director, U.S. Army Research Laboratory, Watertown, MA 02172-0001
2 ATTN: AMSRL-OP-CI-D, Technical Library
1 AMSRL-OP-CI-D, Visual Information Unit
1 AMSRL-OP-PR-WT
20 AMSRL-MA-MB, Mr. Robert Dowding, COR